UNIVERSITÀ DEGLI STUDI DI PADOVA

DIPARTIMENTO DI SCIENZE CHIMICHE

CORSO DI LAUREA MAGISTRALE IN CHIMICA

TESI DI LAUREA MAGISTRALE

Investigation and Structural Optimization of Supported Organic Photocatalyst

Relatore: Prof. Luca Dell'Amico

Correlatore: Prof. Edmondo Maria Benetti

Controrelatore: Prof. Antonio Barbon

Laureanda: Agata Checcozzo

ANNO ACCADEMICO 2023/2024

Summary

Preface

The successful realization of a photoredox catalyst plays an important role in the development of photocatalytic transformations. Design a photocatalyst give the chance to achieve different redox potential of the excited state and therefore to activate different substrates. In addition to this, one of the challenges of catalysis is to have a catalyst in the reaction system that can be easily recovered. Taking into consideration these two important concepts, the aim of the project is the synthesis and characterization of supported redox photocatalysts.

Within the scenario of TADF photocatalysts, organic molecules with thermally activated delayed fluorescence, 1,2,3,5-tetrakis(carbazol-9-yl)-4,6-dicyanobenzene (4CzIPN) stands out as one of the most relevant ones. The latter, is composed of an acceptor core, dicyanobenzene, and donor groups, carbazoles. Considering that the photoredox properties of these molecules can be easily modified by the incorporation of different substituents in the donors, we decided to prepare a family of TADF molecules presenting carbazoles and diphenylamine with electron withdrawing group (Bromine) or electron donating group (Methoxy).

Looking at the goal of having a photocatalyst that is easy to remove from the reaction mixture, a strategy was developed in which the latter is supported in a polymeric system. The photocatalyst was functionalized with a chain of glycols having a methacrylic function at the end capable of polymerizing. By carrying out a controlled radical polymerization, in particular an atom transfer radical polymerization (ATRP) in the presence of poly (ethylene glycol) methyl ether methacrylate p(OEGMA) as a copolymer, the final p(OEGMA-*co*-3("Donor-Group")IPN-MA) is easily obtained.

Finally, is demonstrated that the photocatalyst-functionalized can be efficient in photocatalyzed reaction by irradiating with blue light (λ_{max}= 427 nm), as all photocatalysts absorb at this wavelength and therefore a direct comparison is possible. In the path that involves a reductive quenching for the photocatalyst, a radical addition of the Giese type, a radical decarboxylation with the addition of a

Michael acceptor, and a Povarov type cyclization were tested. Reaction yields are directly proportional to the excited state potentials of catalysts. Regarding the pathway involving oxidative quenching of the photocatalyst, a dehalogenation of a benzylhalide was tested. Again, the reaction yields reflect the reducing capacity of the catalyst.

Prefazione

La realizzazione di catalizzatori fotoredox gioca un ruolo importante nello sviluppo di trasformazioni fotocatalitiche. La progettazione di un fotocatalizzatore dà la possibilità di ottenere potenziali redox dello stato eccitato variabili e quindi di attivare diversi substrati. Oltre a questo, una delle sfide della catalisi è quella di avere un catalizzatore che possa essere facilmente recuperato dal sistema di reazione. Considerando questi due importanti concetti, l'obiettivo del progetto è la sintesi e la caratterizzazione di catalizzatori fotoredox supportati.

Nell'ambito dei fotocatalizzatori TADF, molecole organiche con fluorescenza ritardata attivata termicamente, l’1,2,3,5-tetrakis (carbazol-9-il)-4,6-dicianobenzene (4CzIPN) si distingue come uno dei più rilevanti. Quest’ultimo è composto da un nucleo accettore, il dicianobenzene, e da gruppi donatori, i carbazoli. Considerando che le proprietà fotoredox di queste molecole possono essere facilmente modulate inserendo gruppi donatori diversamente sostituiti, si sintetizza una famiglia di molecole TADF che presentino carbazoli e difenilammine *para*-sostituiti con gruppo elettron-attrattori (bromo) ed elettron-donatori (metossi).

Guardando all'obiettivo di avere un fotocatalizzatore facile da rimuovere, è stata sviluppata una strategia in cui esso è supportato in un sistema polimerico. Il fotocatalizzatore, infatti, è stato funzionalizzato con una catena di glicole avente all'estremità una funzione metacrilica in grado di polimerizzare. Attraverso polimerizzazione radicalica controllata, in particolare *activator regenerated by electron transfer atom transfer radical polymerization* (ARGET ATRP) in presenza di poli(metacrilato) come copolimero, si ottiene facilmente il p(OEGMA-*co*-3("Donor-Group")IPN-MA).

Infine, è dimostrato che i fotocatalizzatori ottenuti possono essere efficienti in reazioni che necessitano mediatori fotoattivi, irradiando con luce blu (λ_{max}= 427 nm), dal momento che tutti i fotocatalizzatori assorbono a questa lunghezza d'onda ed è quindi possibile un confronto diretto. Nel ciclo catalitico che prevede un quenching riduttivo per il fotocatalizzatore, sono state testate un'addizione radicalica di tipo Giese, una decarbossilazione radicalica con l'addizione di un accettore di Michael, e una ciclizzazione di tipo Povarov. Le rese di reazione sono direttamente proporzionali ai potenziali redox di stato eccitato dei catalizzatori. Per quanto riguarda il quenching ossidativo del fotocatalizzatore, è stata testata una dealogenazione di un benzilalogenuro. Anche in questo caso, le rese della reazione riflettono la capacità riducente del catalizzatore.

1. Introduction

1.1. Photochemistry

"The field of photochemistry concerns chemical reactions promoted by the absorption of light"[1]. In photochemistry, light is uses as a partner of reaction as it drives chemical transformation. In photocatalysis, a new reaction pathway is defined[2], running through reactive intermediates that cannot be achieved by thermal conditions.[3,4]

Between 1908 and 1912, Giacomo Ciamician, after conducting several experiments, demonstrated the power of light to drive chemical reactions, with his important work "The Photochemistry of the Future"[5]. He established that a lot of light-induced reactions studied by himself were initiated by light energy excluding the thermal one[6]. High-energy intermediates that are not thermally accessible can be achieved and high energy barriers can be overcome in a short time and under mild reaction conditions through photochemical steps[7–9].

At the basis of a photochemical reaction, a substrate (a reactant or a photocatalyst) must be able to absorb a radiation that generally must have sufficient energy to allow the promotion of an electron to an excited state [10]. When a molecule that is in the ground state S_0, absorbs a photon, reaches an excited singlet states S_n. The primary process that can generally occur is the internal conversion (IC) to the lowest vibrational state S_1, according to Kasha's rule, considering the relaxation to S_0 will always start from this lower vibrational level.[11]

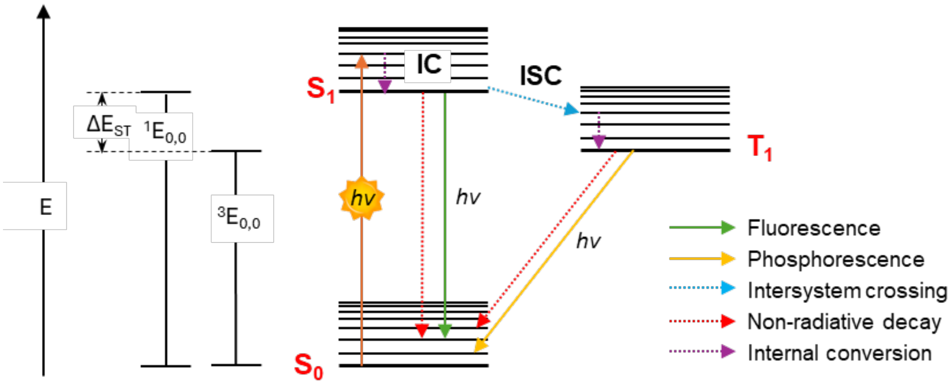

Figure 1. Jablonski diagram.

At this point, the molecule can go back to the ground state through different pathways, as shown **Figure 1**.

Relaxation from the excited state S_1 to the ground state S_0 is possible through non-radiative decay (internal conversion, IC) or by radiative decay (Fluorescence). There is also the possibility that the excited state S_1 will undergo inter system crossing (ISC) and lead to the lower excited triplet state T_1. In this case, relaxation to the S_0 state occurs by inter system crossing (ISC), or by radiative decay (Phosphorescence). Since this process is spin forbidden transition, it occurs when spin-orbit coupling (SOC) happens[12] and, consequentially, the total spin angular momentum $\vec{S}$ changing is compensated by a total orbital angular momentum $\vec{L}$ changing.

Photochemistry can be divided into two main fields: direct photochemistry and photocatalysis. In direct photochemistry one of the reactants absorbs light and consequently it is directly excited.[13,14] In contrast, in photocatalysis when reagents cannot directly absorb light, a photocatalyst serves as an essential intermediary.

1.1.1 Direct photochemistry

In direct photochemistry, light is absorbed directly by the molecule, which must possess either chromophore groups or ester or ketone functional groups capable of absorbing light[15]. Since these groups absorb in the UV medium (λ<300 nm), the radiation used is highly energetic and dangerous[16]. Despite this, direct photochemistry has set milestones in the synthesis of thermally inaccessible scaffolds.

The earliest examples of photochemical transformations involved the direct irradiation of substrates such as the *syn–anti* isomerization of oximes reported by Ciamician and Silber (**Scheme 1**)[6].

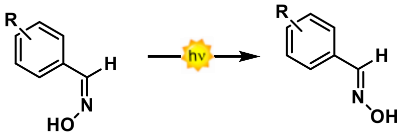

1 **2**

Scheme 1. Photoinduced syn-anti isomerization of oximes.

Another important contribution at the beginning of direct photochemistry is from the Italian chemist Emanuele Paternò and the Swiss chemist George Büchi with the Paternò-Büchi reaction[17]. This reaction, is a [2+2]-photocycloaddition between an alkene (**4**) and the excited state of a carbonyl compound (**3**) to give the corresponding oxetane **5** (**Scheme 2**). Mechanistic studies of the reaction have revealed that the radiation is absorbed by the benzophenone carbonyl, forming either a singlet or a triplet state.

This reaction was firstly reported in 1909, but it is still used nowadays.[18]

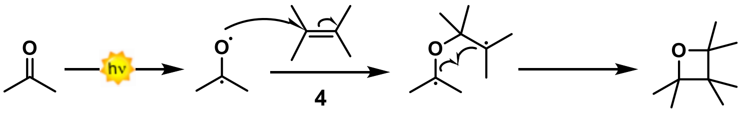

3 **5**

Scheme 2. Paternò- Büchi reaction mechanism.

1.1.2 Photocatalysis

In photocatalysis, radiation of the appropriate wavelength is absorbed by a mediator, the photocatalyst, which reaches the excited state. From here, a transfer of energy or photons to one of the reaction partners can take place, through potential curves that are inaccessible by thermal means[19].

The field of photocatalysis saw an important development in the early 2000s with the works of MacMillan, Yoon and Stephenson who illustrated how photoactive organometallic compounds were able to catalyze organic reactions.[20–23]

At the beginning catalysts were mainly metal-based exploiting Ruthenium, Iridium and other rare earths metals which have proven to be suitable photocatalysts for a lot of transformations.[24] Despite the countless advantages, the interest of scientific research has shifted towards the design of organic-based photoactive compounds, looking at a more sustainable chemistry, equally electronically modulable and cheaper[25]. In fact, organic-based photocatalysts offer greater chemical tunability. Their structures can be easily modified to adjust properties like light absorption, redox potential, and solubility, allowing for precise control over catalytic activity.

Metal-based and organic-based catalysts can also differ from each other by the "type of excited state" that can be charge transfer (CT) and locally excited (LE). In the CT mechanism the electron density is displaced from one part of the molecule (donor moiety) to another (acceptor moiety) and it is the typical excited state of metal-based photocatalysts. Purely organic compounds undergo both mechanisms, where in the LE the electron density is retained in the same area of the molecule during the transition $\pi \rightarrow \pi^*$ (better orbital overlapping).[26] LE states are typically shorter-lived than CT states according to Fermi's golden rule [27] stating that the transition's rate depends upon the strength of the coupling between the initial and final state and upon the density of the final states of the system. Specifically, the relaxation rate is given by the following formula:

$$W_{fi} = \frac{2\pi}{\hbar} \mid \langle f \mid \hat{H}_{int} \mid i \rangle \mid^2 \rho(E_f)$$

Where:

- $\hbar$ is the reduced Planck constant,
- *f* and *i* are the wavefunctions of the initial and final sates,
- $\hat{H}_{int}$ is the interaction Hamiltonian responsible for the transition,
- $\mid \langle f \mid \hat{H}_{int} \mid i \rangle \mid$ is the matrix element representing the overlap between the initial and final states,
- $\rho(E_f)$ is the density of final states available at energy E_f.

Since in LE states the excitation is localized within a specific part of the molecule, the matrix element tends to be large (the transition involves a localized change) making it easier for the molecule to relax back to the ground state. In CT states, the excitation involves a significant separation of charge, where an electron is transferred from one part of the molecule to another, making the matrix element smaller. It results in a longer lifetime of the CT excited state since its decay turns out to be slower.

A photocatalyzed reaction can undergo different pathway: hydrogen atom transfer (HAT) or halogen-atom transfer (XAT), energy transfer (EnT), electron transfer (ET) and proton-coupled electron transfer (PCET). [28]

- In the ***HAT*** process the activation of the substate pass through the transfer of a hydrogen atom $H^{\bullet}$. The excited PC* abstracts a hydrogen atom from the substrate and the protonated form, PC-H, can consequently donate the $H^{\bullet}$ to another substrate closing the photocatalytic cycle (**Scheme 3**). [29]

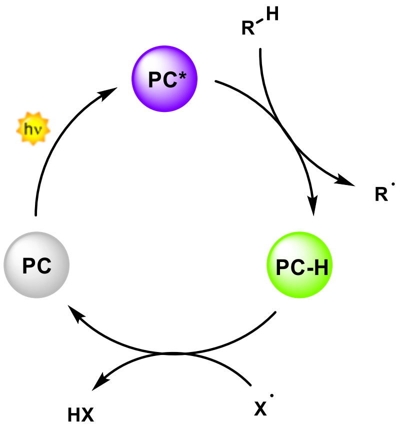

Scheme 3. Hydrogen atom transfer mechanism.

If the starting organic substrate is a halogenated compound (R-X) and the interaction with the PC* brings to the cleave of the C-X bond, the process is referred to as the halogen atom transfer (XAT) mechanism (**Scheme 4**). In this mechanism, a carbon-cantered radical is formed ($R^{\bullet}$) and the photocatalyst forms a PC-X species, which can then transfer the halogen atom ($X^{\bullet}$) to another substrate, thereby regenerating the photocatalyst. Halogen-atom transfer (XAT) is a fundamental step in radical reactions to generate carbon-based radical intermediates from alkyl and aryl halides efficiently.[30]

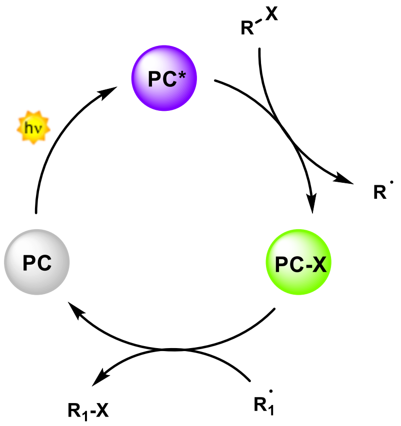

Scheme 4. Halogen atom transfer mechanism.

- The ***EnT*** *generally* works from the triplet excited state. Once the catalyst reaches the excited S_1 state, it undergoes ISC accessing the triplet T_1 from where it transfers energy to the substrate R that reaches its triplet excited state (**Scheme 5**). This process is possible if the triplet energy of the compound involved in the reaction is lower than T^1 energy of the photocatalyst.[31]

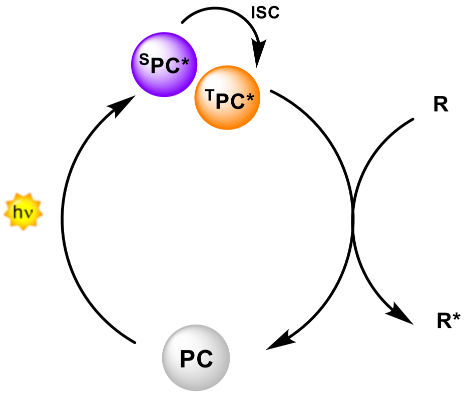

Scheme 5. Energy transfer mechanism.

EnT could take place in two different ways: Förster resonance energy transfer (FRET)[32] or Dexter exchange.[33] FRET is a non-radiative energy transfer process that occurs via dipole-dipole interactions between molecules, leading to the transfer of energy from the donor's excited state to the acceptor. [34] Dexter exchange is at the same a non-radiative process, but in this case it involves a simultaneous intermolecular exchange of two electrons. The excited photocatalyst donates an electron to the LUMO of the substate and simultaneously the substrate donates an electron to the HOMO of the PC. The substrate reaches the excited state while the photocatalyst is restored to its ground state.

- The ***ET*** process in *most cases* works directly from the excited singlet state, but ET from triplet excited state must be not exlueded[35]. After excitation, the PC is more reductant and more oxidating. Indeed, when an electron is excited from the highest occupied molecular orbital (HOMO) to the lowest unoccupied molecular orbital (LUMO) brings to the formation of two single occupied molecular orbitals (SOMOs, **Figure 2**). The lowest in energy is more stabilized with respect to the HOMO of the ground state form, resulting in a higher oxidative power of the PC*, on the contrary, the highest SOMO is more destabilized with respect to the LUMO of the ground state, resulting in an enhanced reductive power of the PC*.

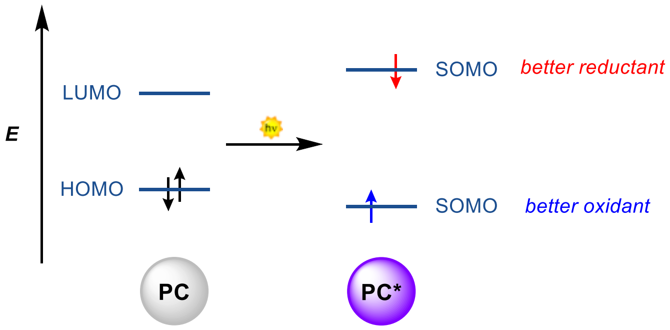

Figure 2. Energy level comparison between ground state and excited state of a PC.

From this situation the compound can both donate or accept an electron to or from an organic substrate giving access to two different pathways: the reductive quenching and the oxidative one depending on the oxidation state of the catalyst (**Scheme 6**).[36]

⇒ In the **reductive quenching**, the excited photocatalyst takes one electron from an electron rich donor (D) forming the radical anion $PC^{\bullet-}$. Afterwards, the ground state of the PC is restored thanks to the presence of an electron poor molecule (acceptor A). In this cycle the PC promotes the oxidation of the substrate that generally represents the donor moiety.

⇒ In the **oxidative quenching**, the PC* donate an electron to the acceptor molecule (A) forming the radical cation $PC^{\bullet+}$**.** The ground state will be restored by a donor D. Inversely from the reductive quenching, the PC promotes the reduction of the substrate.

Obviously, the pathway that occurs depends on the redox potentials of the PC* and the substrate.

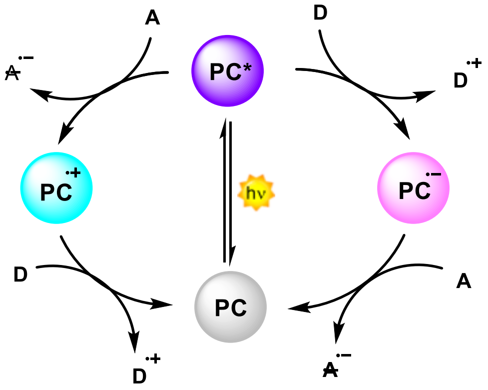

Scheme 6. Electron transfer mechanism.

- Finally, another mechanism that combines two of the previous ones, is the ***proton-coupled electron transfer*** (PCET). In this type of process, the PC* transfer both an electron and a hydrogen atom at the same time, generating the radical species of the substrate. The oxidative and reductive quenching pathway can be distinguished also in this case (**Scheme 7**).[37]

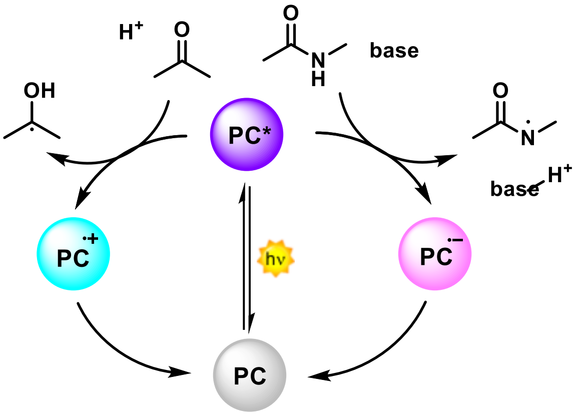

Scheme 7. Proton-coupled electron transfer mechanism.

Important, to determine whether PC* will react from the triplet state or the singlet state, several factors must be considered. Firstly, for energy transfer (EnT) to occur, the substrate must have a lower triplet energy compared to the photocatalyst. If both mechanisms are possible, the diffusion constant (k_{diff}) for the formation of the encounter complex (PC* + substrate) must be considered, as this is the first step in a photophysical process. According to the Jablonski diagram (**Figure 3**), if the rate constant of the intersystem crossing process (k_{ISC}) is lower than k_{diff}, the singlet state (^{1}PC*) will form the complex. Conversely, if k_{ISC} is higher, the triplet state (^{3}PC*) will form the complex.

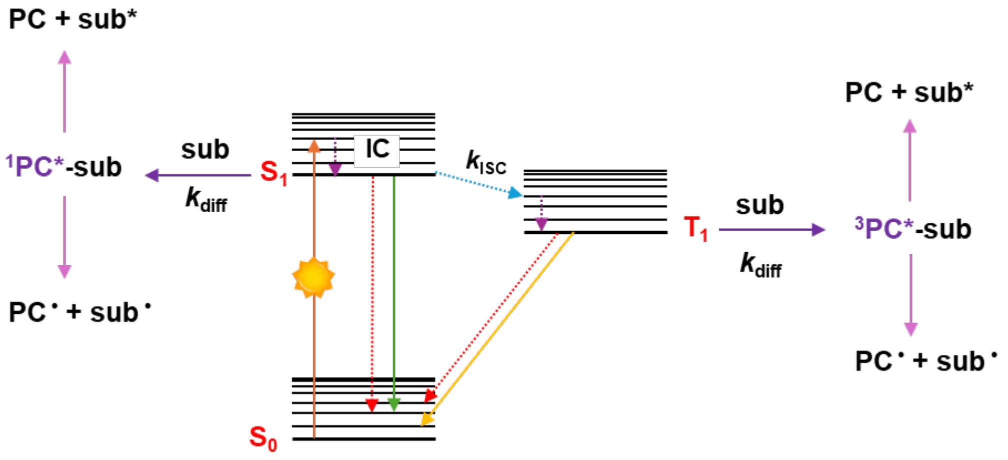

Figure 3. Jablonski diagram reporting the formation of the encounter complex between the excited state of the catalyst (PC) and the substrate (sub).*

1.1.2.1 Organic photoredox catalysts

In recent years, the development and use of purely organic photoredox catalysts has seen a rapid increase, since they are more sustainable and easier to design[38,39,40]. After light irradiation, an organic PC is promoted to its excited state S_1, generally through a π-π^* transition. The S_1 state has a duration in the order of few ns and is usually involved in the redox event. In some cases, however, thanks to ISC, the PC reaches a T_1 state, and this is desirable due to its longer lifespan. Organic PCs can be rationally designed precisely to work through the S_1 or T_1 state and this is a great strength of photoredox catalysis.

Like in the MLCT process in metal-based PCs, organic PCs access charge transfer (CT) in the excited state when the HOMO and LUMO are spatially separated. This is allowed to govern electron-donating or electron-withdrawing substituents at specific positions in the molecule. A recent classification of organic PCs is based on their ability to activate the substrate towards both oxidation and reduction. So, we can divide it in strongly oxidizing organic PCs, strongly reducing and bimodal PCs, which have a balanced distribution of their redox power that allows them to be used both oxidative and reductive[38].

Organic molecules that show thermally activated delayed fluorescence (TADF), like emitters in organic light emitting diodes (OLEDs), have found increasing use as organic photoredox catalysts.[41,42] This particularly family of compound, once exited to its S_1, exhibits an improvement in the lifetime of the excited state. This because S_1 and T_1 are close in energy (in these particular molecules the triplet state is very high in energy) and so once it gets populated, the compound doesn't phosphoresce, because of a too big ΔE_{S0T1}, but reverse intersystem crossing (RISC) takes place. This phenomenon extends the excited state lifetime of TADF catalysts, until to microseconds, in the best cases. These prolonged excited state lifetimes enhance the efficiency of the photocatalysts by increasing the probability of interactions between the excited photocatalyst (PC*) and the reactant.

ΔE_{S1T1} is the parameter to control because is the one that governs the states' mixing. Indeed, it is directly proportional to the exchange integer (J) between S_1 and T_1:

$$\iint \Phi(r_1)\Psi(r_2)\left(\frac{e^2}{r_2 - r_1}\right)\Phi(r_2)\Psi(r_1)dr_1 dr_2$$

Where $\Phi(\mathrm{r})$ and $\Psi(\mathrm{r})$ are the wavefunctions of HOMO and LUMO orbitals. The exchange integer depends on the overlap of the molecular frontier orbital involved in the transition $S_1 \rightarrow T_1$. It is clear that minimising the overlap between HOMO and LUMO we will observe a smaller J and a smaller ΔE_{S1T1}[43].

It's for this reason that the key for the strategy to have a TADF compounds lies in creating spatially separated and electronically decoupled donor-acceptor structures.

The 1,2,3,5-Tetrakis(carbazol-9-yl)-4,6-dicyanobenzene (4CzIPN)[44] is widely studied in the family of TADF photocatalyst, belonging to the carbazolyl dicyanobenzene (CDCBs), a derivative of cyanoarenes[45]. The 4CzIPN (**6**) is composed of an electron poor aromatic core (acceptor core) and four carbazoles that represents the electron rich part of the molecule (donator moieties). From the DFT calculations (**Figure 4**) the HOMO is clearly localized on the substituents while the LUMO on the centre of the molecule and steric hindrance generally intensifies this spatial separation. The same compound can act both as oxidating and reducing agent, like a bimodal photocatalysts.[46]

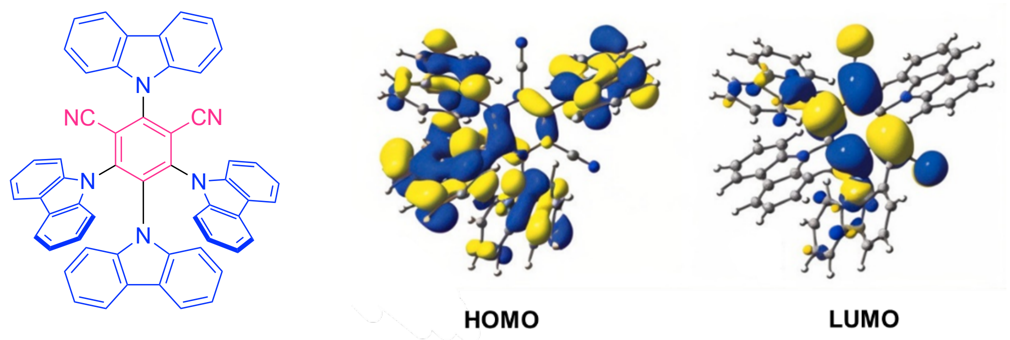

6

*Figure 4. Representation of 4CzIPN (**6**) on the left and its HOMO and LUMO orbitals on the right. Represented from [44].*

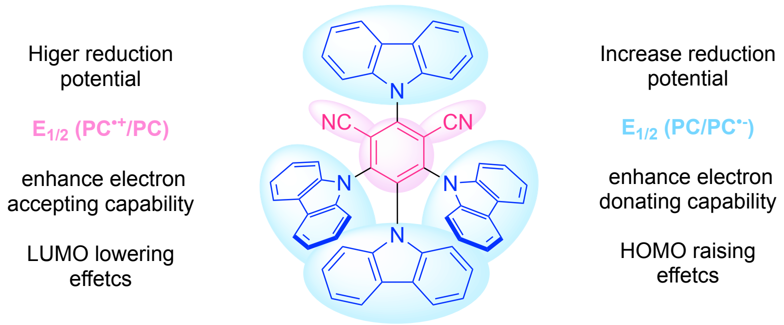

6

Figure 5. Correlation of redox potentials and the impact of donor/acceptor strength[40].

Considering the frontiers molecular orbitales ad spatially separated, the reduction and oxidation power of the PC can be optimized, designing new photocatalysts. In the ground state, emphasizing the electron donating capability of the system, the HOMO is raised bringing to an increase in the reduction potential ($E_{1/2}$ $(PC^{\bullet+}/PC)$). Inversely, accentuating the electron accepting ability will lower the

LUMO giving higher oxidation potentials ($E_{1/2}$ (PC$^{\bullet-}$/PC)) as reported in **Figure 5** in the case of 4CzIPN[47]. The excited state energy is evenly distributed between the oxidation and reduction potentials, creating both a strong oxidant and a strong reductant upon light irradiation.

Speckmeier et al. reported a tuning in the 4CzIPN, modifying both the acceptor core and the donor moieties, also introducing the effect on the redox potentials by halogens (Fluorine or Chlorine). In particular, they identified as a strong oxidizer 3CzClIPN, a molecule consisting of the core dicyanobenzene, a chlorine substituent and 3 Cz units, with $E_{1/2}$(PC*/PC$^{\bullet-}$)= +1.56 V, while as a strong oxidant 3DPA2FBN, consisting of a benzonitrile core, two fluorine substituents and 3 diphenylamine, with $E_{1/2}$(PC$^{\bullet+}$/PC*)= -1.60 V[48].

1.2 Controlled radical polymerization

In the last decades, big effort was spend trying to develop polymerization processes that give access to polymers with narrow distribution of molecular weight, *i.e.,* low **dispersity** (*Đ*), where is defined "low" if is less than 1.5. This parameter is important because it influences the interfacial properties.[49] In fact, synthetic polymers are intrinsically polydisperse, meaning that different chains possess different lengths, and this feature is particularly evident for polymers obtained through free radical polymerization. Indeed, polymers presenting a low dispersity are reported to present well-defined properties.

The most common way to achieve control over the polymerization is exploiting reversible deactivation radical polymerization (RDRP) methods[5051]. These procedures differ from free radical polymerizations because they possess distinct features that resemble living ionic polymerizations[52]. In RDRPs, terminations of propagating chains and other side reactions are minimized by keeping low the concentration of radicals (typically 10^{-8}-10^{-9} M) throughout the polymerization process. Under optimized RDRP conditions, ideally all the chains are initiated at the same time and grow uniformly. However, differently from living ionic polymerizations, irreversible termination reactions among radicals cannot be completely avoided. Thus, the main goal of an RDRP is to elongate the lifetime of radical species that, for free radical processes, is about 1 second before termination occurs. To achieve that, RDRPs are based on an equilibrium between propagating radicals and their corresponding *dormant species.* The polymer chains remain in a dormant state for most of the polymerization process, avoiding premature radical recombination and disproportionation. One of the most employed RDRPs is atom transfer radical polymerization (ATRP).

1.2.1 Atom transfer radical polymerization

ATRP was incepted in 1995 thanks to the independent works of Matyjaszewski[53] and Sawamoto.[54] This technique usually employs a transition metal complex as the catalyst and an alkyl halide (R-X) as initiator. The process relies on an activation-deactivation equilibrium between halogen-capped dormant species and propagating radicals. The latter are generated by activation of the initiator or dormant species by the transition metal complex ($Mt^n\backslash L$). The activation occurs via the reductive cleavage of a C-X bond by the activator complex, forming a propagating radical and the corresponding oxidized complex $X\text{-}Mt^{n+1}\backslash L$, which then acts as deactivator. The reaction between the deactivator and the radical species reverts them back to the dormant state. The deactivation rate constant k_{deact} is generally bigger than the activation one (k_{act}) and this allow the ATRP equilibrium is shifted toward dormant species. This is key for the control as the radical's concentration is kept low, minimizing termination processes. The transition metals used in ATRP are many (Fe, Cu, Mo etc.), but in most cases Cu is the most effective[55].

In a typical ATRP, a Cu(I) complex is employed (Cu(I) /L, where L is a polydentate amine ligand), which is responsible for the cleavage of the C-X bond forming propagating radicals while turning into a Cu(II) complex, namely Cu(II)X/L that will act as the deactivator (**Scheme 8a**).

However, several ATRP mechanisms have been developed with the aim of employing a Cu(II) complex that is reduced in situ in the polymerization mixture, rather than a Cu(I) complex that requires strictly inert atmospheres.[56] Among these, the most common are initiators for continuous activator regeneration (**ICAR**) ATRP[57], supplemental activation reducing agent (**SARA**) ATRP[58], photochemically mediated ATRP (*photo*ATRP),[59] electrochemically mediated ATRP (***e*ATRP**),[60] and activator regenerated by electron transfer (**ARGET**) ATRP.[61]

In ARGET ATRP a reducing agent is responsible for the continuous regeneration of the active oxidation state of the metal complex (**Scheme 8b**).

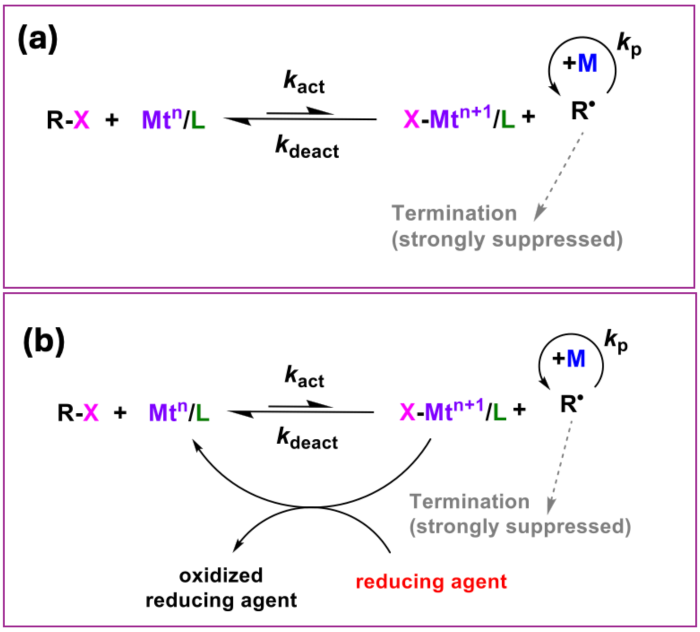

Scheme 8. Generalized mechanism of a) normal ATRP and b) ARGET ATRP.

In ARGET ATRP the amount of the metal catalyst needed is much lower, since the activator is continuously reformed thanks to a reducing agent (such as Tin$^{(II)}$ 2-ethylhexanoate ($Sn(EH)_2$), glucose, ascorbic acid, sodium ascorbate, silver metal, etc), and the rate of polymerization can be controlled by adjusting the type and amount of reducing agent. About the latter, an important feature to consider in ATRP is the oxygen-sensitivity. This represents the main drawback of ATRP, that is overcome in ARGET ATRP using an excess of reducing agent relative to the catalyst, which can reduce the Cu$^{(II)}$ species formed by reaction between the activator and adventitious oxygen.[62–65]

1.2.3 Supported photocatalysts

In recent years, the concept of supporting photocatalysts on materials has gained popularity, since this allows for combining the benefits of photocatalysis with the properties of the support material[66]. Supported catalysts typically offer a longer lifespan and extended operational life[67], since they are both sustainable in catalytic processes[68] and easy to recover and to reuse.

Polymers represents a valid option to support catalysts.[69] The main advantages are their low price and ease of synthesis. Furthermore, these materials can be endowed with a wide variety of functionalities, enabling the properties to be easily adjusted to meet specific application requirements.

There are two main approaches that can be followed to incorporate photocatalysts: the first one is based on the attachment of the photocatalyst to a pre-synthesized functional polymer by post-polymerization modifications;[70,71] the other, and most used strategy, consists of the modification of the catalytically active molecule so that it can be (co)polymerized.[72–74] This second approach makes the insertion of the photocatalyst within polymer chains less demanding and controllable, especially using RDRP techniques, allowing to the synthesis of defined copolymers.

Copolymers are polymers made by linking two or more different monomers together. Depending on the choice of monomers and the strategies used, we can produce various types of copolymers. In the specific case of incorporating a photocatalyst, the resulting (co)polymer could be used for several light-mediated reactions, it should be recovered and reused[75] and can be used under homogeneous conditions, meaning in solvents where the copolymer is soluble and easily accessible by the reacting substrates.

These copolymers can be tailored for specific needs such as solvent compatibility, light transmittance, or the positioning of the photocatalyst. Their properties, mostly dictated by the choice of comonomers, can be tailored to achieve the desired outcome, giving access to a highly adaptable platform. The monomer that is copolymerized with the monomer incorporating the photocatalyst usually represents the major molar fraction, and it is often chosen solely based on the desired characteristics of the material. Indeed, in most reported systems, the possibility of interactions between the photoactive part and the structural part is overlooked, with the assumption that the polymer environment has no actual influence on the catalytic activity, as often observed. Very few literature examples studied the influence of polymer composition on photocatalytic properties. Kobashi and Yoo[76] covalently incorporated an Ir-based photocatalyst in copolymers combining ethyl methacrylate with styrene, *N*-isopropyl acrylamide, or benzyl methacrylate, and measured different catalytic activities. Recently, Ferguson group[77] studied the comonomer effect for vinyl based photocatalytic polymers. They reported that with some comonomers the photophysical properties of the diphenyl benzothiadiazole photocatalyst were significantly different, while the photocatalytic efficiency was mainly dependent on the reaction conditions. Thus, based on the state-of-the-art of photocatalyst-embedding copolymers, we can generally assume that binding a photocatalyst within a polymer will not significantly affect its properties. Conversely, it is well described that the photocatalyst structure and the reaction solvent can have a big impact on the catalytic performance.

Incorporating photocatalyst-bearing monomers along polymer chains can be a way to address some of the main drawbacks of photocatalysis such as solubility issues and poor recyclability. However, polymers are not always easy to separate from the reaction mixture. Finding a solvent in which the copolymer is not soluble while the reaction mixture is, can be a key step in the precipitation of the polymeric system and therefore its recovery.

A weak point that can occur in the polymeric system and must be consider is the chemical degradation of the catalysts. Especially when dealing with organic molecules, they are very prone to bleaching, which obviously invalidates the reusing process. Recently, a study conducted by Pester’s group demonstrated that light irradiation for just a few hours can lead to photobleaching of certain photocatalysts.[78] This phenomenon occurs whether the molecules are used in solution, directly immobilized on inert supports or incorporated within brushes. It cannot be generally asserted that the copolymerization of photoactive units prevents their degradation, but some considerations can be made in this regard. These structures appear to provide a more protective environment for the photocatalyst maybe limiting the interaction between the radical form of the PC and the radical intermediates of the reaction. There are numerous examples of catalysts, such as fluorescein,[79] rose Bengal,[80] eosin Y,[72] porphyrins[81] and others, that can be reused.

These examples highlight that there is a significant dependence of photocatalyst degradation on reaction conditions.

2. Aim of the study

Visible light organo-photoredox catalysis has demonstrated its enormous potential for facilitating challenging chemical reactions.

One of the most studied compounds of the IPN class is the *1,2,3,5-tetrakis(carbazol-9-yl)-4,6-dicyanobenzene*, referred as 4CzIPN (**Figure 6**). Its analogue diphenylamine as a donor group is *1,3-Dicyano-2,4,5,6-tetrakis(diphenylamino)-benzene*, referred as 4DPAIPN (**Figure 6**).

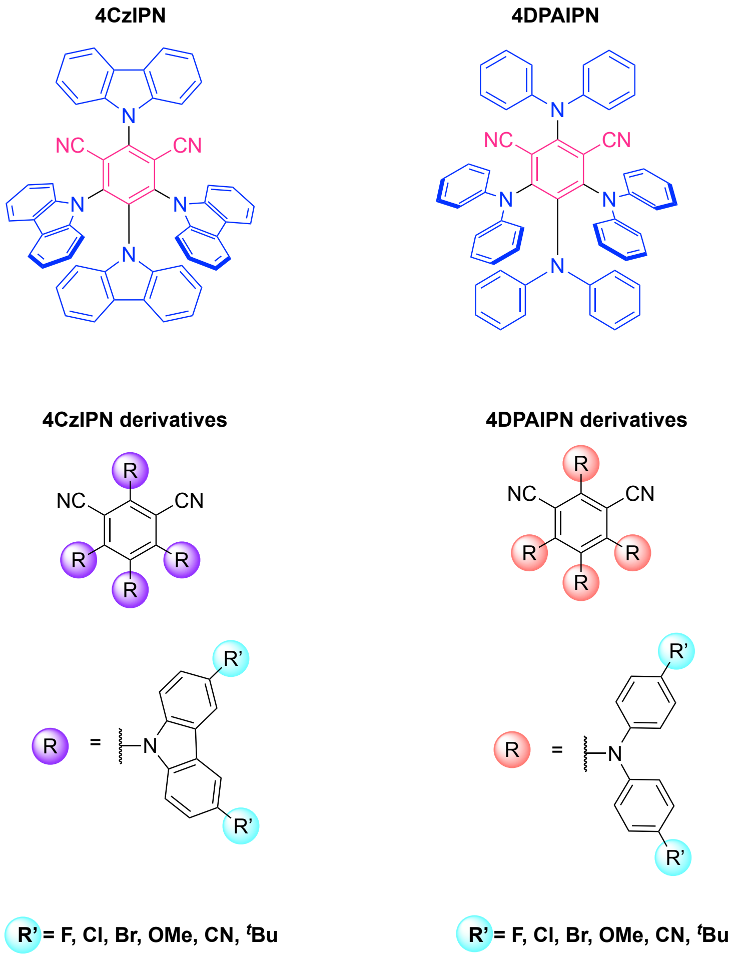

Figure 6. Common modifications to the IPN core involve substituting the aromatic core with different groups. Using carbazoles (Cz) gives the 4CzIPN, while using diphenylamine (DPA) produces the 4DPAIPN. Further modifications to Cz or DPA can create analogues with varying redox potentials

These two molecules are taken as a reference in this project, studying how steric and electronic modifications affects the photochemical and redox properties of the PC.

The goal is to have two families of compounds, the photocatalysts **7** and **8** (**Figure 7**), in order to evaluate how stereoelectronic variations affect the photophysical properties of the molecules and how homogeneous photocatalytic processes are affected by these variations, comparing them with compounds known in the literature.

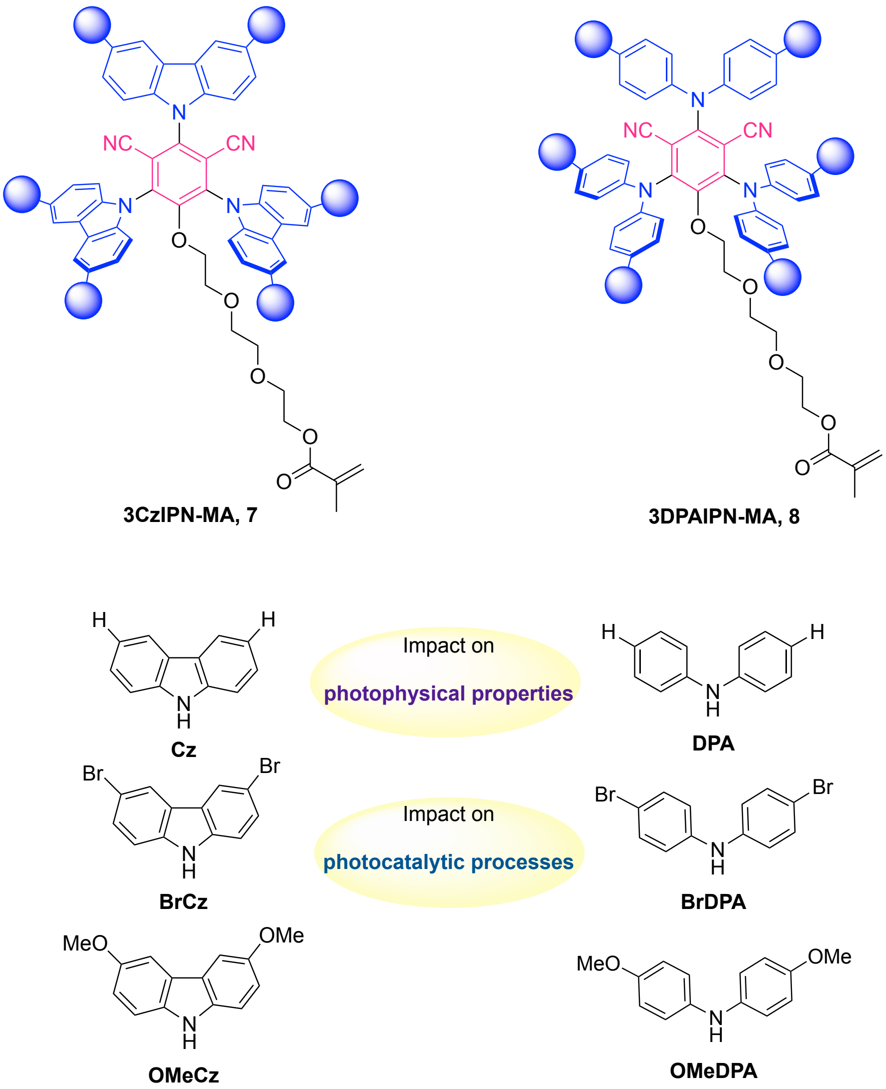

*Figure 7. Representation of the two photocatalyst-functionalized monomers, **7** and **8**. On the left the carbazole (Cz) derivatives (● = H, Br, OMe), on the right the diphenylamine (DPA) derivatives (● = H, Br, OMe). OMeCz= 3,6-dimtheoxy-9H-carbazole, BrCz= 3,6-dibromo-9H-carbazole, OMeDPA= 4,4'-dimethoxydiphenyalmine, BrDPA= 4,4'-dibromodiphenylamine, IPN=isophthalonitrile, MA=methacrylic*

We want to study the photophysical properties of the designed compounds, such as at the UV-Visible absorption and emission spectra, in order to determine the $E_{0,0}$, the redox properties, to know both the ground state potentials and the excited state potentials, and the delayed fluorescence. To have an easily recoverable photocatalyst, it will be supported through ATRP in the presence of an amphiphilic poly(methacrylate), setting the incorporation of the PC within the copolymer equal to 5%.

Once the polymer systems have been obtained and the incorporation has been verified, it will be possible to test photocatalyzed reactions to verify whether the photocatalysts obtained are able to access the catalytic cycle.

3. Result and discussion

3.1 Comparative of the Photocatalyst-functionalized monomers: photophysical characterization

The first part of the project focused on the design, synthesis, and characterisation of five photocatalysts that can be incorporated within a poly(methacrylate).

The photophysical properties of these compounds were studied and summarized to facilitate a better comparison. To do this, a version of the photocatalysts was synthesized in which the final double bond is saturated. This was done in order to mimic the electronic nature of the photoactive moiety in the polymer since, once it is incorporated into the copolymer backbone, the monomer does not exhibit the terminal double bond.

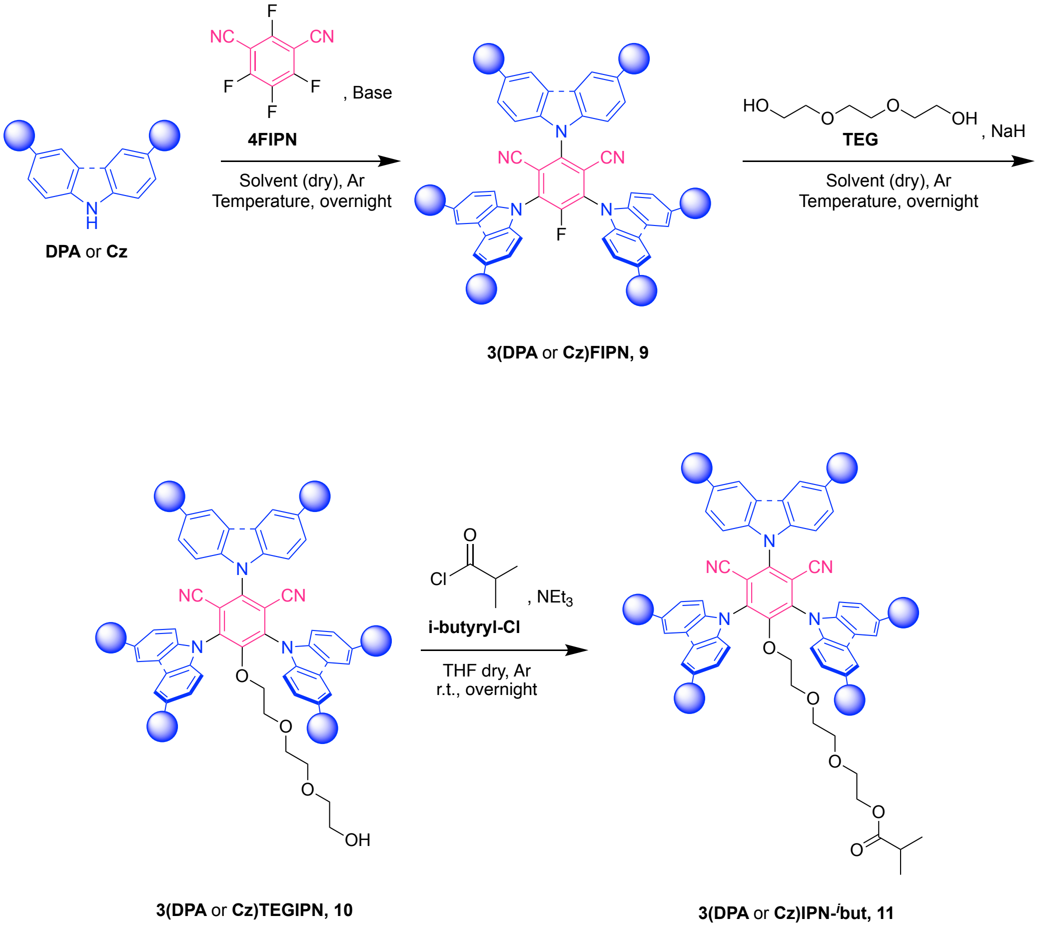

*Scheme 9. Synthetic steps to obtain the Photocatalyst-functionalized monomers in the saturated version (**11**). All the details are in the Supporting Information.*

In the first step, we want to obtain the monofluorinated intermediate **9**, from the tetrafluoroisophthalonitrile (**4FIPN**), in such a way that the fourth substitution with the triethylene glycol (**TEG**) chain can be carried out and obtain the compound **10**. TEG was chosen as a linker between the photocatalytic moiety and the methacrylate function, or the isobutyryl function (**i-butyryl**) in the case of the saturated version. The use of such a long chain was meant to avoid any potential interactions between the photoactive part and the polymer backbone. The final photocatalyst **11**, **3("Donor-Group")IPN-^{i}but**, where the ^{i}but stay for the terminal isobutyryl functionality, will be used for all the characterizations.

3.1.1 Steady-State Absorption and Emission Spectroscopy ($E_{0,0}$)

The UV-Visible and Fluorescence spectra were measured to measure the singlet energy of the photocatalysts ($E_{0,0}$) i.e. the energy difference between the first vibrational level of the ground electronic state and the first vibrational level of the first excited electronic state.

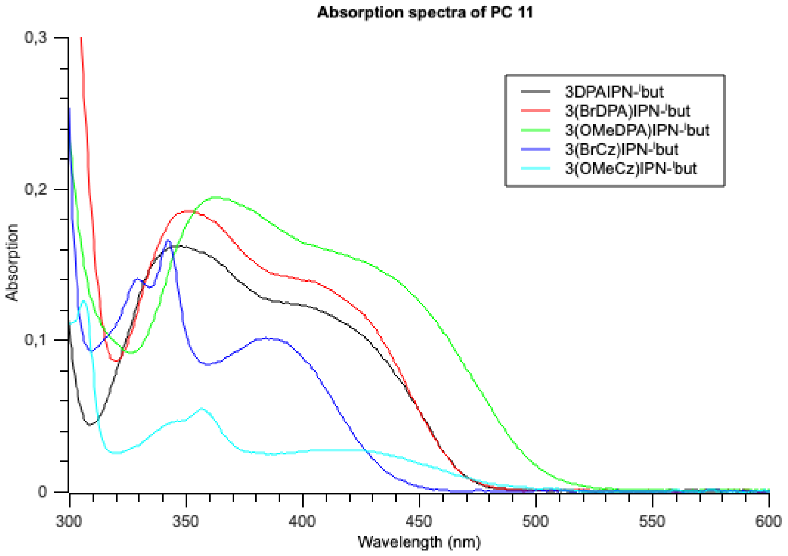

*Figure 8. UV-Visible absorption profile of the photocatalysts **11** (solution 10^{-4} M in acetonitrile).*

All photocatalysts show a broad absorption band in the visible region (λ>400nm) attributable to charge-transfer transitions from the donor side, diphenylamine (DPA) or carbazole (Cz), to the acceptor core, dicyanobenzene[82,83]. The most red-shifted absorption of the 3(OMeDPA)IPN-^{i}but compared to the other is due both for the more electron-rich nature of DPA compared to Cz moieties and for the electron donating nature of methoxy substituent.

Experimentally, from the intersection point between the absorption and emission profiles, the energy $E_{0,0}$ can be derived, since the fluorescence spectrum represents the transition between the first excited energy level and the ground level.

The values can be summarized in **Table 1**.

Photocatalyst	**Intersection point (nm)**	**$E_{0,0}$ (eV)*****
4CzIPN*	464	2.67
3CzIPN-^{i}but **	445	2.74
3(BrCz)IPN-^{i}but	450	2.76
3(OMeCz)IPN-^{i}but	490	2.53
4DPAIPN*	486	2.55
3DPAIPN-^{i}but	462	2.68
3(BrDPA)IPN-^{i}but	464	2.67
3(OMeDPA)IPN-^{i}but	504	2.46

*Table 1. Comparative of the $E_{0,0}$ values of the Photocatalyst-functionalized monomer, saturated version. *Values from literature, ** from Elena Avanzini Master Thesis, ***calculated from the wavelength values*

All the single absorption and the emission profiles are present in the Supporting Information.

3.1.2 Cyclic Voltammetry measurement

Cyclic voltammetry allows us to determine the redox potentials of photocatalysis in the ground state. This is important as those are required to estimate the excited state potentials.

In the case of reduction, the $E_{1/2}$ was considered since the photocatalysts have a reversible peak, unlike the oxidation profile where the peak is irreversible. In this case, the anodic peak value, $E_{p,a}$, was taken as the potential value.

The values are summarized in the **Table 2**.

Photocatalyst	**$E_{1/2}$(PC/PC$^{\bullet-}$) (V)**	**$E_{p,a}$(PC$^{\bullet+}$/PC) (V)**
4CzIPN*	-1.24	+1.49
3CzIPN-^{i}but **	-1.30	+1.21
3(BrCz)IPN-^{i}but	-1.17	+1.75
3(OMeCz)IPN-^{i}but	-1.36	+1.22
4DPAIPN*	-1.66	+1.01
3DPAIPN-^{i}but	-1.63	+1.26
3(BrDPA)IPN-^{i}but	-1.48	+1.39
3(OMeDPA)IPN-^{i}but	-1.75	+0.87

Table 2. Calculated redox potential of the Photocatalyst-functionalized monomer in the saturated version, ***11****, in the ground state. All the measure was performed in ACN at room temperature using tetrabutylammonium hexafluorophosphate (TBAPF$_6$ 1M) as supporting electrolyte. All the solution are 10^{-3} M, except for 3(BrCz)IPN-^{i}but that is 10^{-4}M. Ferrocene is used as internal standard. All values are vs SCE. *Values from literature, ** from Elena Avanzini Master Thesis*

Looking at the potentials obtained, diphenylamine derivatives have more negative reduction potentials (PC/PC$^{\bullet-}$), as the structure of diphenylamine is more electron rich and therefore it is more difficult to add an electron. On the contrary, the rigid and planar structure of carbazole favors electronic delocalization and better tolerates the negative charge. Similarly, the reduction potentials of the oxidized form of carbazole derivatives (PC$^{\bullet+}$/PC) are higher in value, as having the structure delocalized makes it easier to abstract an electron and they are easily reducible.

The effect of the substituents can be seen by comparing the two electronally opposites, i.e. the 3(OMeDPA)IPN-^{i}but and the 3(BrCz)IPN-^{i}but. In the first case, the electron donating methoxy group greatly lowers the reduction potential ($E_{1/2}$(PC/PC$^{\bullet-}$)= -1.75 V) being energetically expensive to add an electron to a structure rich in electron density. Similarly, the redox potential of the oxidized form is less positive ($E_{p,a}$(PC$^{\bullet+}$/PC)= +0.87 V). In the second case, bromine acts as an electron withdrawing group and in carbazole the ease with which an electron can be added is accentuated, having the least negative potential of all compounds

($E_{1/2}$(PC/PC$^{\bullet -}$)= -1.17 V). In the case of the oxidized form, adding an electron is very easy in a structure poor in electron density ($E_{p,a}$(PC$^{\bullet +}$/PC)= +1.75 V).

3.1.3 Calculation of redox potential in the excited state

For the estimation of the potentials of the excited state, the Rehm-Weller formalism was applied[1]:

$$E(PC^{*}/PC^{\bullet -}) = E(PC/PC^{\bullet -}) + E_{0,0}$$

$$E(PC^{\bullet +}/PC^{*}) = E(PC^{\bullet +}/PC) - E_{0,0}$$

where:

- $E(PC^{*}/PC^{\bullet -})$ and $E(PC^{\bullet +}/PC^{*})$ are the reduction potential of the photocatalyst in the exited state
- $E(PC/PC^{\bullet -})$ and $E(PC^{\bullet +}/PC)$ are the reduction potential of the photocatalyst in the ground state
- $E_{0,0}$ is the energy of the singlet

The resulting calculated reduction potential of the photocatalyst in the exited state are summarized in the **Table 3**:

Photocatalyst	**$E_{1/2}$(PC*/PC$^{\bullet -}$) (V)**	**$E_{p,a}$(PC$^{\bullet +}$/PC*) (V)**
4CzIPN*	+1.43	-1.18
3CzIPN-^{i}but **	+1.44	-1.53
3(BrCz)IPN-^{i}but	+1.59	-1.01
3(OMeCz)IPN-^{i}but	+1.17	-1.27
4DPAIPN*	+0.76	-1.41
3DPAIPN-^{i}but	+1.05	-1.42
3(BrDPA)IPN-^{i}but	+1.19	-1.28
3(OMeDPA)IPN-^{i}but	+0.71	-1.59

*Table 3 Calculated redox potential of the Photocatalyst-functionalized monomer in the saturated version, **11**, in the exited state. All values are vs SCE. *Values from literature, ** from Elena Avanzini Master Thesis*

Looking at the excited state potentials obtained and considering that the photocatalyst in this electronic configuration has two unpaired electrons in two different SOMOs, it can be easily understood that these values are a direct quantification of the oxidizing or reducing power with respect to a general substrate.

In fact, the higher the absolute value of the reduction potential of the PC*/$PC^{•-}$ or $PC^{•+}$/PC* pair, the more the oxidation or reduction of a substrate that has a lower potential in absolute value will be favoured. For example, if a generic substrate S, electron poor, with a reduction potential E(S/$S^{•-}$) of a value lower in absolute value to $E_{p,a}$($PC^{•+}$/PC*), encounters the photocatalyst in the excited state in the reaction mixture, then the reduction of the substrate S to $S^{•-}$ and the oxidation of PC from PC* to $PC^{•+}$ will be favoured. The photocatalyst is counter-oxidative quenching and is a reducing agent against the S substrate. The same applies in the case of oxidizing power.

As can be seen from the experimental values obtained, rich electron structures, such as those containing electron donating substituents or in the general case of diphenylamine, have a greater reducing power ($E_{p,a}$($PC^{•+}$/PC*) has higher values in absolute value) and therefore the reduction of the substrate and the oxidation of the photocatalyst is favoured. In the case of structures less rich in electron density, such as in the case of electron withdrawing substituents or in general those containing carbazole as donor groups, the oxidizing power is higher ($E_{1/2}$(PC*/$PC^{•-}$) has higher values in absolute value) and therefore the oxidation of the substrate and the reduction of the photocatalyst is preferred.

3.1.4 Lifetime measurements

The lifetime of the excited state of the various PC was measured for two main reasons. First, it is reported that the excited state of a photocatalyst must have a lifetime of at least 1 ns, otherwise the compound tends to emit before forming the encounter complex with the substrate.[26] Secondly, one of the most important features of this type of PC is its very long excited-state lifetime, which is correlated to its TADF behaviour. Measuring the lifetime was necessary to confirm that the excited state duration was sufficiently long and to determine if the compound still exhibited reverse intersystem crossing (RISC).

Two different techniques were used for this purpose. Direct fluorescence was measured using time-correlated single-photon counting (TCSPC)[84] a technique typically employed for short lifetimes (a few nanoseconds at most). In this method, a detector converts a single photon into an electronic pulse, and the TCSPC electronics accurately measures its arrival time relative to the excitation pulse. Thousands of arrival times are recorded showing their statistical intensity at a given time, from which the decay fitting provides the lifetime.

For delayed fluorescence, a more suitable method is Multi-Channel Scaling (MCS),[85] a photon counting technique generally used for measuring longer lifetimes. In MCS, multiple photons are collected in each sweep of the time window, quickly accumulating decays across timescales ranging from several hundred nanoseconds to seconds.

All the values are summarized in the below **Table 4**.

Photocatalyst	**Prompt fluorescence, τ_p (ns)**	**Delayed Fluorescence, τ_d (ns)**
4CzIPN*	18.7	1 390
3CzIPN-^{i}but **	10.5	255
3(BrCz)IPN-^{i}but	-	817
3(OMeCz)IPN-^{i}but	0.6	4.4
4DPAIPN*	3.4	67
3DPAIPN-^{i}but	-	7.2
3(BrDPA)IPN-^{i}but	2.3	66 000
3(OMeDPA)IPN-^{i}but	0.3	1.87

Table 4. Comparison between fluorescence lifetimes of 3("DonorGroup")IPN-^{i}but and 4CzIPN[128] and 4DPAIPN[86]. The synthesized PC ***11*** *were measured at room temperature in ACN, by degassing the solution with N_2.*

Comparing these values with lifetime measurements of 4CzIPN and 4DPAIPN under the same conditions,[87] it is evident that the lifetimes of the references are longer, for the delayed fluorescence, excepted for the brominated compound.

We can speculate that the reason behind this result lies in the lower rigidity of the photocatalyst synthesized. In fact, it is described that bulky substituents, and consequently a sterically hindered system, exhibit longer lifetimes of the excited state. This is linked to the larger separation of HOMO and LUMO orbitals, and so to a worse overlapping of the orbitals' wavefunctions.[88–90] We can say that the electron, once in the triplet state, finds it more difficult to return to the singlet state, translating in longer reverse intersystem crossing and consequently longer delayed fluorescence.

As far as brominated compounds are concerned, the region of such a long-delayed fluorescence lies in the heavy atom effect (HAE). In fact, compounds containing heavy atoms such as halogens or sulphur favour the triplet state population. According to Fermi's golden rule, a fast k_{RISC} can be obtained by combining sufficient spin-orbit coupling (SOC) and a small ΔE_{ST}. Specifically, spin-orbit coupling can be promoted by heavy elements and is larger among the excited states of compounds containing this type of atoms, suggesting that this parameter influences the RISC process[91].

3.2 Polymerization in solution

Looking at the ARGET-ATRP, the PC presenting the polymerizable function, is obtained in gram scale and copolymerized with poly(ethylene glycol) methyl ether methacrylate p(OEGMA), producing the photoactive polymers. Then it was verify the incorporation into the polymeric chain, to testing the catalytic activity.

ARGET ATRP was chosen as controlled radical polymerization technique, using ethyl α-bromoisobutyrate (EBiB) as the initiator in solution and targeting a degree of polymerization of 200. The degree of polymerization (DP) measures the number of monomer units in a polymer chain, reflecting the chain's length. The employed transition metal catalyst was $Cu^{(II)}Br_2$ with Tris(2-pyridylmethyl)amine (TPMA) as a ligand (1:2 $Cu^{(II)}$:ligand ratio). OEGMA was chosen as comonomer to generate PC-bearing copolymers that could catalyze reaction both in organic and aqueous media. Sodium Ascorbate (NaAsc) was used as reducing agent, which is a mild reductant often used in ARGET ATRP.[92]. The polymerization procedure is detailed in the Supporting Information.

Polymerization tests were carried out in the presence of only the chosen comonomer, before incorporating the photocatalyst. These are summarized in the **Table 5**.

	OEGMA (mM)	EBiB (mM)	CuBr2/TPMA (mM)	NaAsc (mM)	M_n (Da)	Đ	Conversion (%)
1	1750	8.75	1/2	0.5	8 978	1.34	30
2	1750	8.75	1/2	5	34 278	1.47	80
*3**	432	2.16	0.5/1	2.5	17 066	2.26	90

*Table 5. Optimization of OMEGA polymerization in solution. The solution in the case of Entry 1 and Entry 2 are 50:50 $OEGMA_{300}$:DMSO, while in *Entry 3 was used $OEGMA_{500}$:DMSO 20:80. The reactions were followed by ^1H-NMR to study the kinetic and monomer conversion in the case of $OEGMA_{300}$. The reported M_n were obtained by GPC, calculated using a calibration curve based on PMMA standards. The percentage conversions are referred after 24 h of polymerization. All the details are reported in the Supporting Information.*

In *Entry 1* and *Entry 2* the ratio between $Cu^{(II)}$ and NaAsc was investigated. In the case of *Entry 2*, the reducing agent is five time the molar amount of copper. This is high ratio, permit a faster polymerization, although this can be at the expense of a less controlled polymerization and therefore a greater dispersion *Đ*, as can be seen by comparing the first two row. This is even more accentuated in the case of *Entry 3* in which the 1:5 $Cu^{(II)}$:NaAsc ratio leads to a very high dispersion *Đ*, synonymous with a poorly controlled polymerization. In this case, termination processes may have taken place between already very long chains that have raised the value of *Đ.* In fact, the ideally dispersity (*Đ*) of the polymer chains should be low (*Đ* < 1.5), which is expected for a controlled polymerization.

3.2.1 Copolymerization of OEGMA and the Photocatalyst-functionalized monomer and calculation of the real incorporation

The conditions of *Entry 2* in **Table 5** were then used for the copolymerization of $OEGMA_{300}$ with a 5 mol% of the Photocatalyst-functionalized (3("Donor-Group")IPN-MA) yielding the copolymer p(OEGMA-*co*-3("Donor-Group")IPN-MA).

In the **Table 6** are show the results of the polymerizations.

PC-functionalized monomer	Conversion (%)	Note
3DPAIPN-MA	83	Conversion obtained after 48 h
3(BrDPA)IPN-MA	90	2nd addition of NaAsc after 24 h
3(OMeDPA)IPN-MA	40	2nd addition of NaAsc after 24 h
3(BrCz)IPN-MA	88	-
3(OMeCz)IPN-MA	77	2nd addition of NaAsc after 24 h

Table 6. Conversion of the polymerization obtained from ^{1}H-NMR spectrum using DMF as internal standard.

The incorporation was investigated from the absorbance of the polymer under UV light. A calibration line (**Figure 10**) was built with the solutions containing the saturated version of the various PC in different concentration (**Figure 9**). The incorporation was also quantified ^{1}H-NMR.

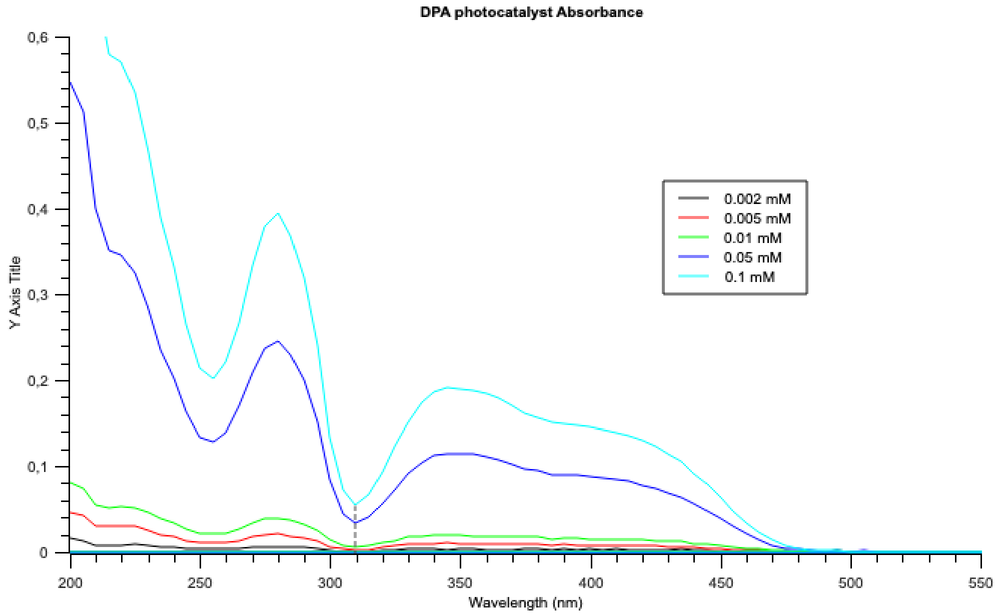

Figure 9. Absorption spectra at different concentration of the monomer 3DPAIPN-^{i}but in ACN.

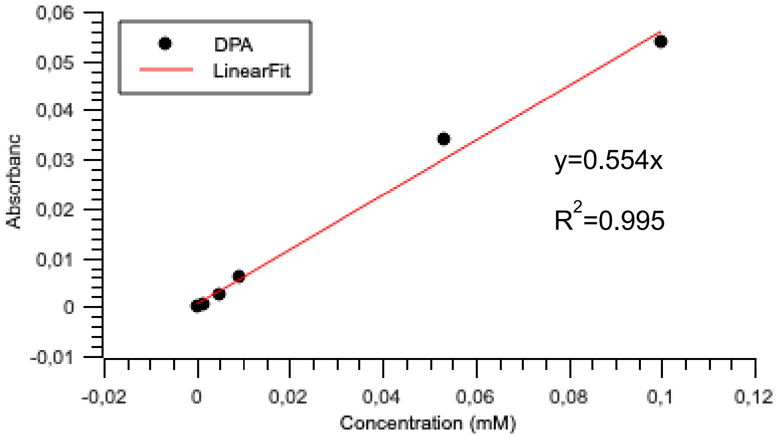

Figure 10. Calibration line built taking the absorbance values at 300 nm of 3DPAIPN-^{i}but in ACN.

The real incorporation of the monomers has been investigated for each catalytic system, both with UV-Visible (**Figure 11**) and via ^{1}H-NMR.

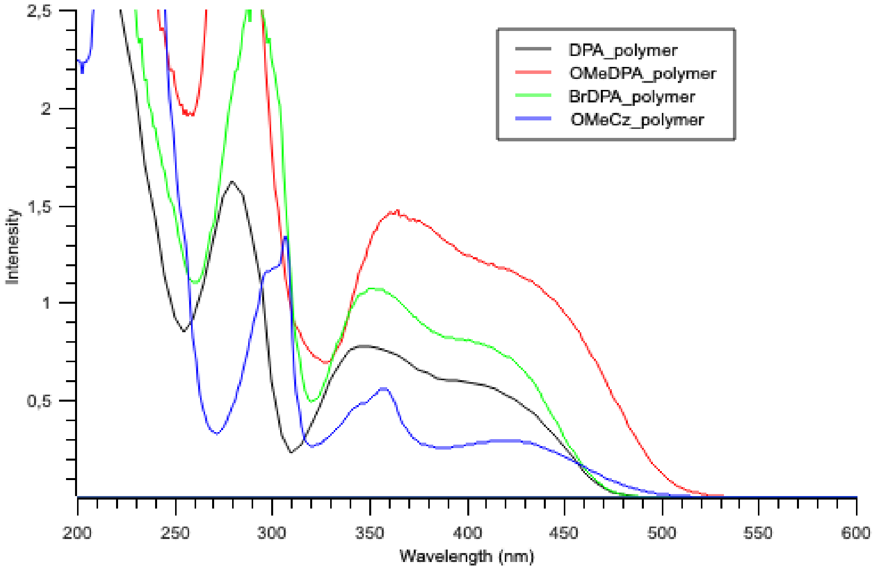

Figure 11. Absorption spectra of the different polymeric systems after ARGET-ATRP.

The **Table 7** summarizes and results obtained:

Monomer	% from UV-Vis	% from ^{1}H-NMR
3DPAIPN-MA	1.6	3
3(BrDPA)IPN-MA	5	4.8
3(OMeDPA)IPN-MA	3	3.8
3(BrCz)IPN-MA	-	1
3(OMeCz)IPN-MA)	1.5	1.8

Table 7. Incorporation of the monomers in the polymeric system obtained from UV-Visible calibration and from ^{1}H-NMR

At this point, it was crucial to understand if the copolymerized photocatalyst was able to catalyse photoreactions.

3.3 Test photocatalyzed reactions

To study the differences between the various catalytic systems obtained, reactions were studied that included in the reaction mechanism in one case the reductive quenching of the PC and in the other the oxidative quenching.

3.3.1 Reductive quenching

3.3.1.1 Giese-type addition

The Giese-type radical addition involves the addition of radical intermediates to versatile Michael acceptors. As radical precursors, carboxylic acids are particularly attractive since the corresponding nucleophilic carbon radical can be readily obtained through a favourable radical decarboxylation process, which releases CO_2 as a traceless by-product.[93]

A proline derivative **13** was used as the radical precursor, and dimethyl maleate **15** served as the Michael acceptor
The photocatalytic cycle of this reaction proceeds via reductive quenching for the formation of the radical precursor **14** through decarboxylation. The generated radical adds to the electron-deficient olefine **15** to generate the radical species **16** that closes the photocatalytic cycle forming the anion **17**. The final product **18** is obtained upon protonation (**Scheme 10**).

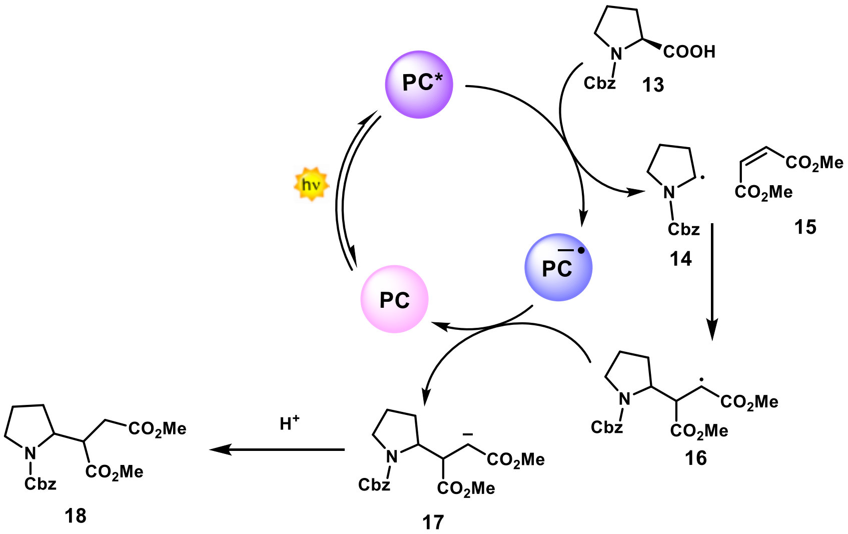

Scheme 10. Photocatalytic cycle of Giese-type radical reaction with the substrates of interest.

This reaction was tested with the polymeric systems obtained after polymerization in acetonitrile using as catalyst loading 5 mol%.

PC	**^{1}H-NMR Yield (%)**	**$E_{1/2}$(PC*/PC$^{\bullet-}$) (V)**	**$E_{1/2}$(PC/PC$^{\bullet-}$) (V)**
4CzIPN*	80	+1.43	-1.26
p(OEGMA-*co*-3CzIPN-MA)**	80	+1.44	-1.30
p(OEGMA-*co*-3DPAIPN-MA)	47	+1.05	-1.63
p(OEGMA-*co*-3(BrDPA)IPN-MA)	51	+1.19	-1.48
p(OEGMA-*co*-3(OMeDPA)IPN-MA)	25	+0.71	-1.75
p(OEGMA-*co*-3(OMeCz)IPN-MA)	6	+1.17	-1.36

*Table 8. ^{1}H-NMR yields of Giese-type photoreactions calculated using dibromoethane CH_2Br_2 as internal standard. The reactions were carried out using a 427 nm Kessil at 25% intensity for 3.5 h. *from literature[92] **from Alessio Lo Bocchiaro Master Thesis*

In the control reaction performed in the absence of a photocatalyst the product was not detected in the crude. This result implies the reaction is photocatalyzed.

The reaction, in addition to presupposing a sufficient oxidizing power of the PC to mediate the decarboxylation process and generate species **14** (e.g., Boc-Pro-OCs, $E_{1/2}$ (red)= +0.95 V vs SCE), also subsequently requires a sufficient reducing potential to generate the corresponding enolate **17** by SET reduction of the α-acyl radical generated in situ (cf. $E_{1/2}$ (red)= -0.60 V vs SCE)[48].

Looking at the redox potentials of the excited state of the synthesized photocatalysts, in principle everyone should possess the thermodynamically driving force necessary to start and conclude the catalytic cycle, with the exception of p(OEGMA-co-3(OMeDPA)IPN-MA) which have a low oxidizing power ($E_{1/2}$(PC*/PC$^{\bullet-}$)= +0.71 V vs SCE), but sees a reaction yield of 25%.

The results obtained with the p(OEGMA-co-3DPAIPN-MA) and p(OEGMA-co-3(BrDPA)IPN-MA) systems give a higher yield respect to with what was expected, in fact from the literature the 3DPAFIPN and 3DPACIIPN give the product with a yield of 16% and 12%, respectively [48]. This could be due to the presence of the polymeric system that could promote better PC-reactant interaction. In the case of p(OEGMA-co-3(OMeCz)IPN-MA), which would possess sufficient excited state redox potentials and ground state to catalyze the reaction, the yield is rather low, 6%. It is hypothesized that there may be rapid intramolecular and unproductive (back) transfer of electrons from their excited state of CT, i.e. internal quenching that may prevent their engagement in catalytic cycles[48]. Another hypothesis that could be take in consideration, is that the methoxylated photocatalysts exabit a very short time both for the delayed fluorescence (τ_d), 1.87 ns for the p(OEGMA-co-3(OMeDPA)IPN-MA) and 4.4 ns for the p(OEGMA-co-3(OMeCz)IPN-MA), and the prompt fluorescence (τ_p), 0.3 ns and 0.6 ns respectively. In these cases, other competitive relaxation processes could take place instead to RISC.

3.3.1.2 Povarov-type cyclization

The Povarov-type cyclization studied involves the addition of *N,N*-dimethylaniline **24** to phenylmaleimide **27** (**Scheme 11**). The reaction was chosen because the mechanism is known and sees the PC involved in two catalytic steps. In addition, it has been tested for both organic and metal-based catalysts, which allows for easier comparison. Moreover, the redox potentials of **24** ($E^0(24^{\bullet+}/24)$= +0.80 V vs SCE) and O_2 ($E^0(O_2/\ O_2^{\bullet-})$= -0.64 vs SCE) fall within the window of redox potentials that can be covered by synthesized PCs.

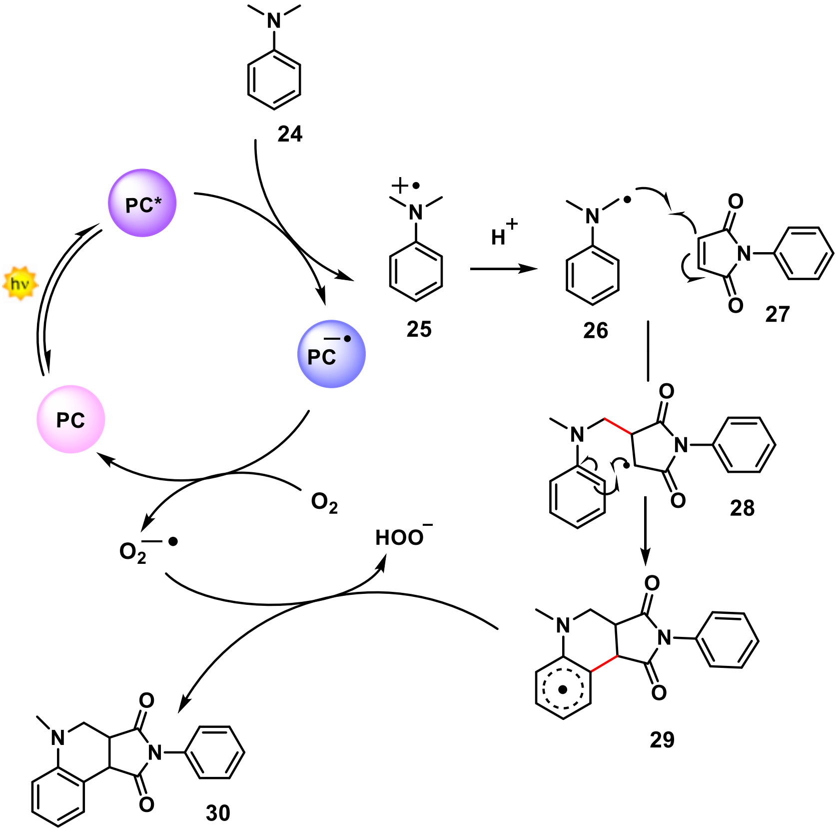

Scheme 11. Reported mechanism of Povarov reaction. The PC is restored in its ground state thanks to the presence of oxygen.

The first step sees the reductive quenching of the PC* with the generation of the *N,N*-dimethylaniline radical cation **25**, which is deprotonated in the reaction environment to give the radical species **26**. At this point, a radical addition with phenylmaleimide **27** leads to the formation of a new C-C bond in species **28**. Following aniline dearomatization, intermediate **29** is produced. A deprotonation on the aniline ring allows the rearomatization of this thanks to the $O2^{\bullet-}$ species generated by the reduction of O_2 by $PC^{\bullet-}$.

The Povarov-type cyclization was tested in acetonitrile both with the Photocatalyst-functionalized monomers (the saturated version) and with the polymeric systems. The catalyst loading used is 3 mol%, as described in literature procedure[94]. The results were summarized in **Table 9**.

	PC	**^{1}H-NMR Yield (%) *Saturated monomer***	**^{1}H-NMR Yield (%) *Polymeric system***	**Time (h)**	**Intensity (%)**	**$E_{1/2}(PC^*/PC^{\bullet-})$ (V)**
1	-	5	5	4	25	-
2	4CzIPN*	61	-	4	25	+1.43
3	3CzIPN-core*	-	42	4	25	+1.44
4	3DPAIPN-core	35	8	4	25	+1.05
5	3(BrDPA)IPN-core	-	9	4	25	+1.19
6	3(OMeDPA)IPN-core	18	5	4	25	+0.71
7	3(BrCz)IPN- core	20	-	4	25	+1.59
8	3(OMeCz)IPN-core	27	6	4	25	+1.17
9	3(BrDPA)IPN-core	45	-	20	100	+1.19
10	3(OMeDPA)IPN-core	40	-	20	100	+0.71

*Table 9. ^{1}H-NMR yields of Povarov-type photoreactions calculated using dibromoethane CH_2Br_2 as internal standard. The reactions were carried out using a 427 nm Kessil, Time and Intensity are detailed in the table.*from Alessio Lo Bocchiaro Master Thesis*

The *Entry* from *1* to *8* are referred to both the polymeric systems and the Photocatalyst-functionalized monomers (saturated version). The tests with the monomers were necessary to see if effectively the system studied was able to catalyze the exanimated reaction. The most oxidant PC, the 3(BrCz)IPN-core, in the case of the saturated monomer, poorly catalyze the reaction. This could be attribute to the high insolubility of the catalytic core in the case of the brominated carbazole. Anyway, all the PCs can catalyze more or less the reaction, since the control experiment without catalyst give the product in 5% yield. More product yield was obtained in case of more power (100% Intensity) and time (20h), for *Entry 9* and *10*. Is interestingly to note that also PC that doesn't match the potential of the *N,N*-dimethylaniline ($E^0(24^{\bullet+}/24)$= +0.80 V vs SCE), the 3(OMeDPA)IPN-core, can give the product.

In the case of the tests with the polymeric systems, a very low yields were obtained. This fact could concern diffusional limits of the reagents within the polymer skeleton, although more in-depth analyses should be performed, since in the case of Giese-type addition, the polymeric system is able to carry out the catalytic cycle.

3.3.2 Oxidative quenching

As regards the reaction pathway involving oxidative quenching of PC, a dehalogenation of benzylhalide was chosen as a benchmark reaction.

The reaction is assumed to proceed by single-electron reduction of α-bromo-p-tolunitrile[94] **31** by **PC***. After that, a species capable of donating a hydrogen atom, an HAT donor, generates the product of reaction **32**. The catalytic cycle of the photocatalyst is closed by oxidation of tributylamine to $Bu_3N^{+\bullet}$, hypothetically by the Hantzsch ester which can act as a reducer[95], and regeneration of PC (**Scheme 12**).

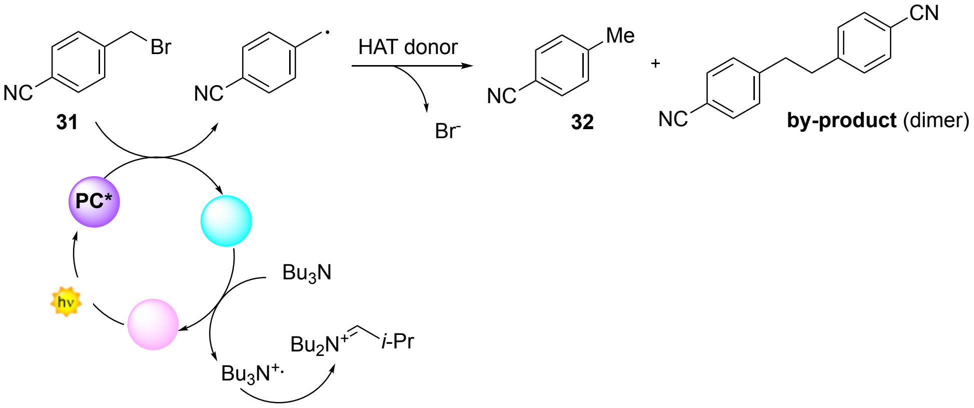

Scheme 12. Hypothetic mechanism for the dehalogenation of benzyl halide in the case of α-Bromo-p-tolunitrile.

This reaction was chosen because despite the fact that the PCs synthesized in principle are not able to access the catalytic cycle, since the reduction potential of α-Bromo-p-tolunitrile is experimentally determined to be equal to -1.64 V, several photocatalysts of the naphthochromenones family are able to give the dehalogenation product with good yields even with redox potentials of the excited ($E_{p,a}(PC^{\bullet+}/PC^*)$) state ranging from -1.27 V to -1.77 V.

The tests were performed in acetonitrile with 3 mol% of catalyst loading for 16 h, as describe in literature[94]. The results are summarized in **Table 10**.

PC	^{1}H-NMR Yield (%)	^{1}H-NMR Yield (%) *by-product*	$E_{p,a}(PC^{\bullet +}/PC^*)$ (V)
p(OEGMA-*co*-3DPAIPN-MA)	16	8	-1.41
p(OEGMA-*co*-3(BrDPA)IPN-MA)	32	8	-1.28
p(OEGMA-*co*-3(OMeDPA)IPN-MA)	30	12	-1.59
p(OEGMA-*co*-3(OMeCz)IPN-MA)	30	5	-1.27

Table 10. ^{1}H-NMR yields of dehalogenation of benzyl halide photoreactions calculated using dibromoethane CH_2Br_2 as internal standard. The reactions were carried out using a 427 nm Kessil at 25% Intensity for 16 h.

The most reducing photocatalysts were chosen to be tested in the oxidative quenching pathway, i.e. PCs containing diphenylamine and the carbazole family, the one replaced with methoxy, as donor groups.

In the crude reaction examined by ^{1}H-NMR, signals appeared relating to a reaction by-product potentially identifiable as the dimer formed by radical combination of the radical intermediate with itself. In terms of equivalents used, considering that each dimer uses two equivalents of the starting material, the photoactive polymeric system that transforms the most quantities of **31** is certainly the most reducing of all, p(OEGMA-co-3(OMeDPA)IPN-MA) ($E_{p,a}(PC^{\bullet +}/PC^*)$= -1.59 V vs SCE), which is also the one that comes closest of all to the potential necessary for single-electron reduction of α-bromo-*p*-tolunitrile **31** (E (**31**/**31**$^{\bullet -}$)= -1.64 V vs SCE).

Interestingly, as is the case with naphthochromenones, PCs that are quite far from the required reduction potential can also access the catalytic cycle. This could be attributable to the fact that the shape of the curve detected in the cyclic voltammetry related to the reduction of the substrate is quite wide at its minimum point and therefore sufficiently accessible in thermodynamic terms, as shown in **Figure 12**.

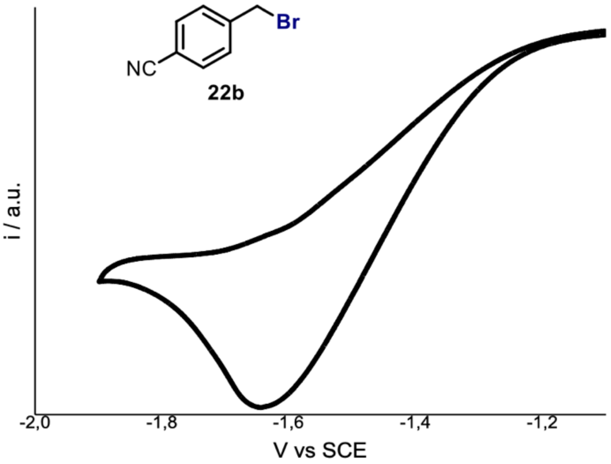

*Figure 12. CV of **31** in 0.1 MTBAPF6 MeCN solution. GC electrode. Scan rate: 100 mV/s, potential referred to SCE at room temperature using a platinum wire as counter electrode. Reported from [93]*

It remains to be seen whether by carrying out reaction optimizations, for example with shorter times to see more substantial differences between the different PCs or with higher lamp intensities (from 50% to 100%) to try to obtain a higher yield, they can be seen in the improvements in the catalytic performance of photoactive polymers.

4. Conclusions

In the light of what is known about molecules exhibiting TADF behaviour and their recent use as photoredox catalysts, this project demonstrates their possible use in benchmark reaction in the form of a polymeric system. This allows easy recovery thanks to precipitation of them and therefore faster reuse, simplifying the purification process of products obtained by reactions catalysed by them.

In the first part of the thesis, the designed PCs are successfully synthesized and characterized to have a knowledge of their singlet energies ($E_{0,0}$), their redox potentials of the ground state and the excited state and their lifetime. It emerges from the comparison that the *para*-substitution of the structure of carbazole and diphenylamine has important effects on redox potentials. The most oxidizing photocatalyst turns out to be the *Bromine*-substituted carbazole core, less electron rich than diphenylamine, i.e. 3(BrCz)IPN-*i*but, with $E_{1/2}(PC^*/PC^{\bullet -})$= +1.59 V. The most reducing PC see by the *Methoxy*-substituted diphenylamine core, which is generally the richer *vs* the carbazole, i.e. 3(OMeDPA)IPN-ibut, with $E_{p,a}(PC^{\bullet +}/PC^*)$= -1.59 V.

In the second part of the thesis, the photoactive monomers were successfully copolymerized with an amphiphilic monomer using ARGET ATRP giving the copolymer poly(OEGMA-co-3("Donor-Group")IPN-MA), with an incorporation ranging from 1 to 5%.

In the third part, three different reaction was tested to verify if the photoactive polymer is able to achieve the catalytic cycle.

The Giese-type addition is actually catalysed, with yields ranging from 5 to 50%, compared to the black reaction that does not produce any product. Obviously, reaction optimizations would be needed to evaluate if higher yields can be achieved.

In the Povarov cyclization, the PCs are able to achieve the catalytic cycle, since the black reaction give the product in very low yield to respect to the system studied, but not as other catalysts described in the literature[93]. Anyway, the 4CzIPN give the product in 60% yield and maybe deeper stereoelectronically modification could give the chance to obtain a better yield. In the oxidative quenching, the dehalogenation of benzyl bromine is catalysed by the photoactive polymers, giving for the p(OEGMA-co-3(OMeDPA)IPN-MA) the best results. Reaction optimizations would be needed to evaluate both if higher yields can be achieved and if the differences between the PCs can be rise in term of redox potential of the exited state.

In conclusion, the studied systems demonstrated photocatalytic activity and easy recovery from the reaction mixture. In addition, they demonstrated a great tunability as organo-photoredox catalysts modifying the donor and acceptor moieties from the originally 4CzIPN TADF photocatalyst. Last but not least, the reactions were carried out by irradiating with blue light (λ_{max}= 427 nm), so using a cheap LED source, under mild and safe condition.

5. Supporting information

5.1 General Infromation

Commercial grade reagents and solvents were purchased from Sigma Aldrich, FluoroChem, BLDpharma or TCIchemicals and used as received, unless otherwise stated.

Oligo[(ethylene glycol) methyl ether methacrylate] (OEGMA) with M_n ~300 g mol^{-1} M_n ~500 g mol^{-1} was purified by passing through a basic aluminium oxide column to remove the inhibitor (butylated hydroxytoluene, BHT) before use.

MilliQ water was purified with a Millipore Direct-Q 5 ultrapure water system or a Milli-Q® IQ 7003 purification system.

5.2 Instruments

NMR spectra were recorded on Bruker AVANCE Neo 400 Nanobay equipped with a BBFOATM-z grad probehead. The chemical shifts (δ) for ^{1}H and ^{13}C are given in ppm relative to residual signals of the solvents ($CHCl_3$ @7.29 ppm ^{1}H-NMR, 77.16 ppm ^{13}C-NMR, CH_2Cl_2 @5.32 ppm ^{1}H-NMR, 53.84 ppm ^{13}C-NMR, $(CH_3)_2CO$ @2.05 ppm ^{1}H-NMR, 29.84 ppm ^{13}C-NMR). Coupling constant are given in Hz. The following abbreviations are used to indicate the multiplicity; s, singlet; d, doublet; t, triplet; q, quartet; m, multiplet; bs, broad signal.

Chromatographic purification of products was accomplished using flash chromatography on silica gel (SiO_2, 0.04-0.063 mm) purchased from MacheryNagel, with the indicated solvent system according to the standard techniques. Thin-layer chromatography (TLC) analysis was performed on pre-coated Merck TLC plates (silica gel 60 GF254, 0.25 mm). Visualisation of the developed chromatography was performed by checking UV absorbance (254 nm). Organic solutions were concentrated under reduced pressure on a Büchi rotary evaporator.

Steady-state absorption spectroscopy studies were performed at room temperature on a Varian Cary 50 UV-vis double beam spectrophotometer; 10 mm and 1 mm path length Hellma Analytics 100 QS quartz cuvettes were used. Steady-state fluorescence spectra, lifetime studies were recorded on a Varian Cary Eclipse Fluorescence spectrophotometer; 10 mm path length Hellma Analytics 117.100F QS quartz cuvettes.

Size exclusion chromatography (SEC) was performed using an Agilent Viscotek 302-TDA gel permeation chromatography equipped with a refractive index (RI) detector, a GRAM pre-colum (50x8, 10 um) and two GRAM analytical linear columns (300x8 mm, 10 um) from Agilent PSS connected in series to determine the number average molecular weight (M_n) and dispersity ($Đ$) of polymers. The column compartment and RI detector were both at 60 ^oC, and the eluent used was DMF containing 10 mM LiBr at a flow rate of 1 mL/min. Every sample (polymer concentration ~2 mg/mL) was prepared by filtering through neutral alumina over a PTFE membrane with a porosity of 0.20 µm. The column system was calibrated with 12 linear poly(methyl methacrylate) standards (M_n = 540–2,210,000 Da).

The potentiostate used for the calculation of the redox potentials is VIONIC powered by INTELLO software from Metrohm Autolab. The measurements were done in a 3-electrode cell. Platinum wire (99.9%) ST 0.6/40 mm was used as auxiliary electrode. The working electrode was a glassy carbon, 70 mm long and 2 mm diameter (body diameter 6 mm), and a Ag/Ag^+ non-aqueous refillable reference electrode (6 mm diameter).

5.3 Experimental Procedures

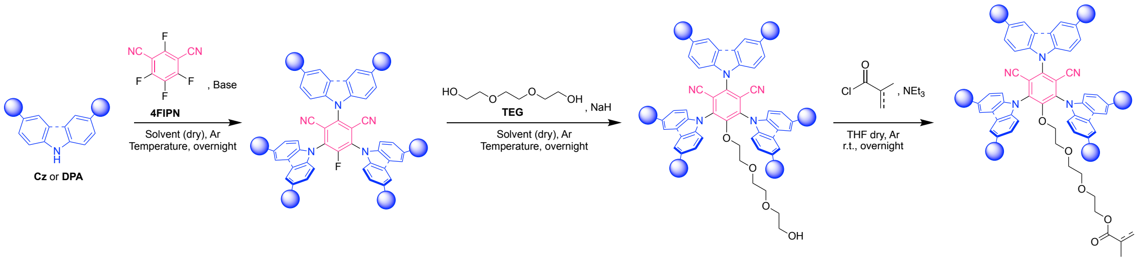

3(DPA or Cz)FIPN, 9

3(DPA or Cz)TEGIPN, 10

3(DPA or Cz)IPN-^{i}but, 11
or
3CzIPN-MA, 7
or
3DPAIPN-MA, 8

General procedures

A. In an oven dried Schlenk flask equipped with a magnetic stir bar 1.25 equiv (per halogen of tetrafluoroisophthalonitrile) diphenylamine were dissolved in dry THF (0.05 M, relating to 1.0 equiv of the corresponding tetrafluoroisophthalonitrile) under an atmosphere of argon. Then, 1.88 equiv (per halogen of tetrafluoroisophthalonitrile) NaH (60% in oil) were added and the suspension was stirred at 50 °C for 30 minutes. Finally, 1.0 equiv of the tetrafluoroisophthalonitrile was added and the resulting mixture was stirred at room temperature for 24h. The reaction mixture was quenched by the addition of water. After removal of THF, the residue was dissolved in DCM and washed with water. The organic phase was dried over Na_2SO_4, and the solvent was removed under reduced pressure. The crude product was purified by column chromatography on silica gel to obtain the product **9** as a solid.[48]

B. In an oven dried Schlenk flask equipped with a magnetic stir bar, 4.2 equiv of substituted diphenylamine were dissolved in dry THF (0.3 M, relating to the total equiv of the diphenylamine) under an atmosphere of argon. The reaction mixture was cooled at -78°C and then 4.2 equiv of LiHMDS (1 M in dry THF) were added slowly. Finally, 1.0 equiv of dissolved tetrafluoroisophthalonitrile (0.1 M in dry THF) was added and the resulting mixture was stirred at room temperature for 24h at room temperature. The reaction mixture was quenched by the addition of water. After removal of

THF, the residue was dissolved in DCM and the organic phase was extracted with DCM. Then, the organic phase was dried over Na_2SO_4 and recrystallized to obtain the product **9** as a solid.

C. In an oven dried Schlenk flask equipped with a magnetic stir bar, 3.0 equiv of substituted carbazole and 1.0 equiv of tetrafluoroisophthalonitrile were dissolved in dry MeCN (0.08 M, relating to the corresponding tetrafluoroisophthalonitrile) under an atmosphere of argon. Tetramethyl piperidine (4.5 equiv) was added slowly. The reaction mixture was heated at 80°C and left at reflux overnight. Finally, the solution was recrystallized to obtain the product **9** as a solid.

D. In an oven dried Schlenk flask equipped with a magnetic stir bar, 1.0 equiv of monofluorinated intermediate **9**, with diphenylamine as donor moieties, and 1.2 equiv of NaH (60% in oil) were dissolved in dry DMAc (0.2 M, relating to **9**) under an atmosphere of argon. Then, 3.5 equiv of triethylene glycol were added at the solution. The resulting reaction mixture was heated at 100°C and left at reflux overnight. The suspension was quenched by the addition of water, extracted with DCM and washed with LiCl (5% p/V). The organic phase was dried over $Na_2SO_{4,}$ and the solvent was removed under reduced pressure. The crude product was purified by column chromatography on silica gel to obtain the product as a solid.

E. In an oven dried Schlenk flask equipped with a magnetic stir bar, 1.0 equiv of monofluorinated intermediate **9**, with carbazole as donor moieties, and 1.2 equiv of NaH (60% in oil) were dissolved in dry THF (0.2 M, relating to **9**) under an atmosphere of argon. Then, 3.5 equiv of triethylene glycol were added at the solution. The resulting reaction mixture was stirred overnight at room temperature. The suspension was quenched by the addition of water, washed with brine and extracted with DCM. The organic phase was dried over $Na_2SO_{4,}$ and the solvent was removed under reduced pressure. The crude product was purified by column chromatography on silica gel to obtain the product as a solid.

F. In an oven dried Schlenk flask equipped with a magnetic stir bar, 1.0 equiv of intermediate **10** and 1.5 equiv of isobutyryl chloride were dissolved in dry THF (0.15 M, relating to intermediate **10**) under an atmosphere of argon. Then, 1.6 equiv of triethylamine (TEA) were added slowly at the solution. The resulting reaction mixture was stirred overnight at room temperature. The suspension was quenched by the addition of water, washed with brine and extracted with DCM. The organic phase was dried over $Na_2SO_{4,}$ and the solvent was removed under reduced pressure. The crude product was purified by column chromatography on silica gel to obtain the product **11** as a solid.

G. In an oven dried Schlenk flask equipped with a magnetic stir bar, 1.0 equiv of intermediate **10** and 1.5 equiv of methacryloyl chloride were dissolved in dry THF (0.15 M, relating to intermediate **10**) under an atmosphere of argon. Then, 1.6 equiv of triethylamine (TEA) were added slowly at the solution. The resulting reaction mixture was stirred overnight at room temperature. The suspension was quenched by the addition of water, washed with brine and extracted with DCM. The organic phase was dried over $Na_2SO_{4,}$ and the solvent was removed under reduced pressure. The crude product was purified by column chromatography on silica gel to obtain the product **7** or **8** as a solid.

5.4 Experimental Data of the Photocatalysts

3DPAFIPN *(2,4,6 Tris(diphenylamino)-5-fluoroisophthalonitrile)*

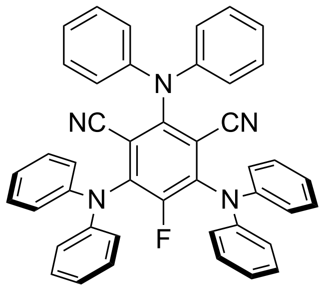

According to **general procedure A** using 200 mg of tetrafluoroisophthalonitrile (1 mmol), 634.6 mg of diphenylamine, 225.6 mg of NaH (60% oil) and 20 mL of dry THF. Column chromatography with hexanes/DCM, 12-85% DCM as gradient. 516.5 mg of product obtained (79% yield), yellow solid.

^{1}H NMR (400 MHz, $CDCl_3$): δ (ppm) 7.27-7.24 (m, 12H), 7.08-7.03 (m, 6H), 7.01-6.97 (m, 12H). According to literature. [48]

^{13}C-NMR (100 MHz, $CDCl_3$): δ (ppm) 152.4 (d, $^1J_{C,F}$= 257.9 Hz, *C*F), 151.8, 145.5, 145.3, 143.1, 129.4, 129.3, 124.6, 124.0, 122.7, 122.68, 112.6, 109.0. According to literature. [48]

^{19}F-NMR decoupled ^{1}H (376 MHz, $CDCl_3$): δ (ppm) -121.3 (s, 1F) According to literature. [48]

3(BrDPA)FIPN *(2,4,6 Tris(4-4'dibromodiphenylamino)-5-fluoroisophthalonitrile)*

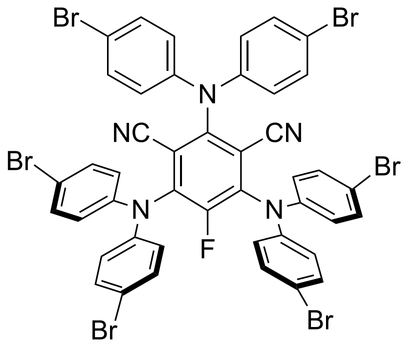

According to **general procedure B** using 1000.5 mg of tetrafluoroisophthalonitrile (5 mmol), 6867.0 mg of 4-4'dibromodiphenylamine, 21 mL of LiHMDS 1M and 79 mL of dry THF. Recrystallization with CH_2Cl_2/Pentane 1/2. 5000.0 mg of product obtained (90% yield), yellow solid.

^{1}H NMR (400 MHz, $CDCl_3$): δ (ppm) 7.39 (m, 12 H), 6.82 (m, 12 H).

^{13}C-NMR (100 MHz, $CDCl_3$): δ (ppm) 144.0, 143.8, 142.4, 142.3, 132.9, 132.8, 124.3, 124.3, 118.5, 117.8, 112.2, 108.7.

^{19}F-NMR decoupled ^{1}H (376 MHz, $CDCl_3$): δ (ppm) -120.2 (s, 1F).

3(OMeDPA)FIPN *(2,4,6 Tris(4-4'dimethoxydiphenylamino)-5-fluoroisophthalonitrile)*

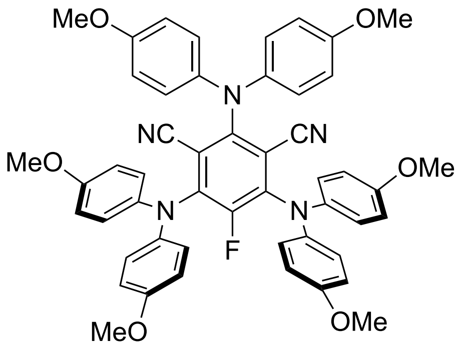

According to **general procedure B** using 1000.5 mg of tetrafluoroisophthalonitrile (5 mmol), 4814.7 mg of 4-4'dimethoxydiphenylamine, 21 mL of LiHMDS 1M and 79 mL of dry THF. Recrystallization with CH_2Cl_2/Pentane 1/2. 3020.0 mg of product obtained (73% yield), orange solid.

^{1}H NMR (400 MHz, $CDCl_3$): δ (ppm) 6.94-6.88 (m, 12H), 6.81-6.78 (m, 12H), 3.78 (s, 18H).

^{13}C-NMR (100 MHz, $CDCl_3$): δ (ppm) 156.4, 155.9, 152.4, 152.4, 152.1 (d, $^1J_{C,F}$=260 Hz), 149.6, 143.3, 143.1, 139.6, 139.3, 124.2, 124.1, 114.6, 114.6, 113.4, 113.4, 106.2, 106.1, 55.4, 55.4.

^{19}F-NMR decoupled ^{1}H (376 MHz, $CDCl_3$): δ (ppm) -124.0 (s, 1F).

3(BrCz)FIPN *(2,4,6, Tris(3,6-dibromo-carbazol-9-yl) 5-fluoroisophthalonitrile)*

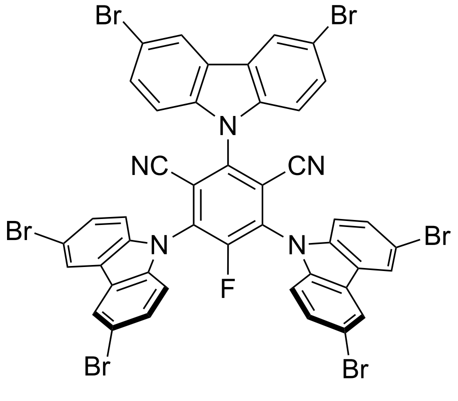

According to **general procedure C** using 1000.5 mg of tetrafluoroisophthalonitrile (5 mmol), 4875.0 mg of 3,6-dibromo-9H-carbazole, 3.83 mL of tetramethylpiperidine (TMP) and 62.5 mL of dry MeCN. The product precipitated during the reaction. It was washed with cooled MeCN and dry with vacuum pump. 4659.0 mg of product obtained (84% yield), yellow solid.

^{1}H NMR (400 MHz, $CDCl_3$): δ (ppm) 8.28-7.70 (m, 6H), 7.68-7.66 (m, 12H), 7.21-7.14 (m, 12H).

^{13}C-NMR (100 MHz, $CDCl_3$): δ (ppm) 138.9, 138.0, 130.7, 130.6, 125.6, 125.4, 124.6, 124.4, 116.3, 116.0, 111.3, 110.6.

^{19}F-NMR decoupled ^{1}H (376 MHz, $CDCl_3$): δ (ppm) -110.3 (s, 1F).

3(OMeCz)FIPN *(2,4,6, Tris(3,6-dimethoxy-carbazol-9-yl) 5-fluoroisophthalonitrile)*

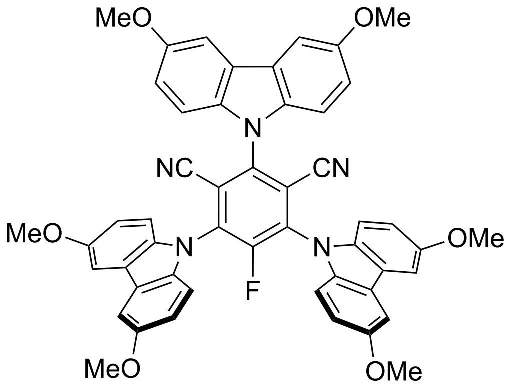

According to **general procedure C** using 1000.5 mg of tetrafluoroisophthalonitrile (5 mmol), 3408.9 mg of 3,6-dimethoxy-9H-carbazole, 3.83 mL of tetramethylpiperidine (TMP) and 62.5 mL of dry MeCN. Recrystallization with H_2O/MeCN to have the product as precipitate. 2000.0 mg of product obtained (50% yield), red solid.

^{1}H NMR (400 MHz, $CDCl_3$): δ (ppm) 7.57 (m, 6H), 7.36-7.08 (m, 12H), 3.98 (d, J = 10.0 Hz, 18H).

^{13}C-NMR (100 MHz, $CDCl_3$): δ (ppm) 155.8, 155.5, 134.5, 125.7, 125.4, 115.8, 115.5, 111.0, 110.2, 104.1, 103.9, 56.1.

^{19}F-NMR decoupled ^{1}H (376 MHz, $CDCl_3$): δ (ppm) -112.6 (s, 1F).

3DPATEGIPN *(2,4,6 Tris(diphenylamino)-5-triethylenglycol isophthalonitrile)*

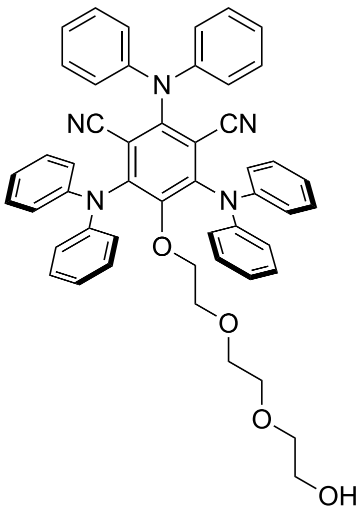

According to **general procedure D** using 323.9 mg of 3DPAFIPN (0.5 mmol), 230 μL of triethylene glycol, 24.0 mg of NaH (60% oil) and 5 mL of dry DMAc. Column chromatography with DCM/EtOAc, 10-50% EtOAc as gradient. 232.0 mg of product obtained (58% yield), yellow solid.

^{1}H NMR (400 MHz, $CDCl_3$): δ (ppm) 7.28-7.26 (m, 12H), 7.05-6.95 (m, 18H), 3.73 (m, 2H), 3.64 (bs, 2H), 3.46 (m, 2H), 3.32 (m, 2H), 3.01 (m, 2H), 2.87 (m, 2H).

^{13}C-NMR (100 MHz, $CDCl_3$): δ (ppm) 151.5, 150.8, 148.5, 145.7, 145.5, 129.4, 124.8, 124.0, 123.9, 123.1, 122.7, 122.3, 113.1, 111.2, 72.5, 72.4, 70.5, 70.3, 68.8, 61.8

3(BrDPA)TEGIPN *(2,4,6 Tris(4-4'dibromodiphenylamino)-5-triethylenglycol isophthalonitrile)*

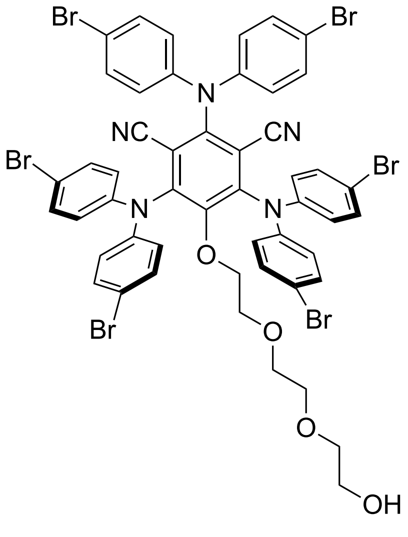

According to **general procedure D** using 3360 mg of 3(BrDPA)FIPN (3 mmol), 1,40 mL of triethylene glycol, 144 mg of NaH (60% oil) and 15 mL of dry DMAc. Column chromatography with DCM/EtOAc, 10-50% EtOAc as gradient. 1400.0 mg of product obtained (35% yield), yellow solid.

^{1}H NMR (400 MHz, $CDCl_3$): δ (ppm) 7.52-7.36 (m, 12H), 6.95-6.68 (m, 12H), 3.70 (dt, 4H), 3.52 (m, 2H), 3.44-3.39 (m, 2H), 3.20-3.16 (m, 2H), 3.02 (t, 2H).

^{13}C-NMR (100 MHz, $CDCl_3$): δ (ppm) 150.6, 150.3, 147.4, 144.1, 144.0, 132.7, 132.7, 124.1, 123.8, 117.6, 117.4, 112.6, 110.9, 73.1, 72.4, 70.6, 70.2, 69.1, 61.7.

3(OMeDPA)TEGIPN *(2,4,6 Tris(4-4'dimethoxydiphenylamino)-5-triethylenglycol isophthalonitrile)*

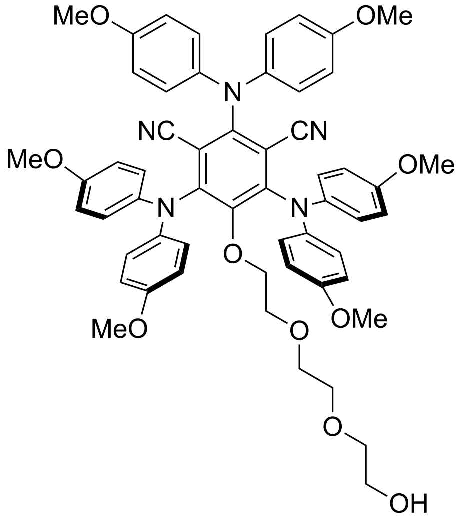

According to **general procedure D** using 413.9 mg of 3(OMeDPA)FIPN (0.5 mmol), 230 µL of triethylene glycol, 24.0 mg of NaH (60% oil) and 2.5 mL of dry DMAc. Column chromatography with DCM/EtOAc, 10-70% EtOAc as gradient. 344.8 mg of product obtained (70% yield), orange solid.

^{1}H NMR (400 MHz, $CDCl_3$): δ (ppm) 6.96-6.83 (m, 12H), 6.76 (m, 12H), 3.75 (s, 18H), 3.67 (m, 4H), 3.47 (m, 2H), 3.39-3.32 (m, 2H), 3.08-3.04 (m, 2H), 2.92 (m, 2H).

3(BrCz)TEGIPN *(2,4,6, Tris(3,6-dibromo-carbazol-9-yl) 5-triethylenglycol isophthalonitrile)*

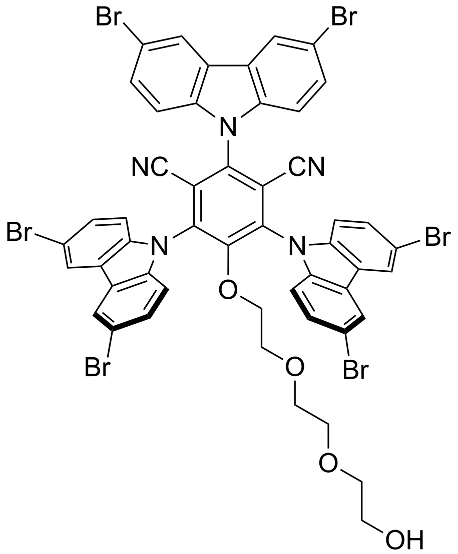

According to **general procedure E** using 2000.0 mg of 3(BrCz)FIPN (1.8 mmol), 0.85 mL of triethylene glycol, 86.0 mg of NaH (60% oil) and 9 mL of dry THF. Column chromatography with DCM/EtOAc, 10-50% EtOAc as gradient. 611 mg of product obtained (30% yield), yellow solid.

^{1}H NMR (400 MHz, $CDCl_3$): δ (ppm) 8.26 (m, 6H), 7.70 (m, 6H), 7.32-7.22 (m, 7H), 3.65 (bs, 2H), 3.45 (m, 2H), 3.13-3.06 (m, 2H), 3.04-2.97 (m, 2H), 2.69-2.59 (m, 4H).

^{13}C-NMR (100 MHz, $CDCl_3$): δ (ppm) 154.9, 139.4, 138.3, 130.5, 125.2, 124.4, 116.2, 115.6, 112.0, 110.9, 74.2, 72.2, 70.2, 69.7, 61.6, 60.4.

3(OMeCz)TEGIPN *(2,4,6, Tris(3,6-dimethoxy-carbazol-9-yl) 5-triethylenglycol isophthalonitrile)*

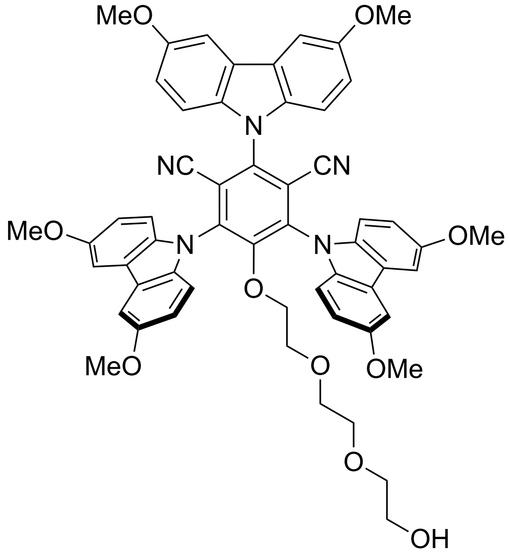

According to **general procedure E** using 1400.0 mg of 3(OMeCz)FIPN (1.7 mmol), 0.80 mL of triethylene glycol, 82.0 mg of NaH (60% oil) and 9 mL of dry THF. Column chromatography with DCM/EtOAc, 10-70% EtOAc as gradient. 829 mg of product obtained (51% yield), red solid.

^{1}H NMR (400 MHz, $CDCl_3$): δ (ppm) 7.57 (m, 6H), 7.33-7.24 (m, 6H), 7.18 (m, 6H), 3.97 (s, 18H), 3.58 (m, 2H), 3.38-3.31 (m, 2H), 2.96 (m, 4H), 2.56 (m, 4H).

^{13}C-NMR (100 MHz, $CDCl_3$): δ (ppm) 155.4, 155.3, 155.3, 154.0, 141.1, 139.3, 135.8, 134.9, 125.2, 125.1, 115.6, 115.4, 115.1, 111.7, 111.3, 110.3, 103.9, 103.6, 103.6.

3DPAIPN-^{i}but *(2,4,6 Tris(diphenylamino)-5-tryethylenglicolisobutyrate isophthalonitrile)*

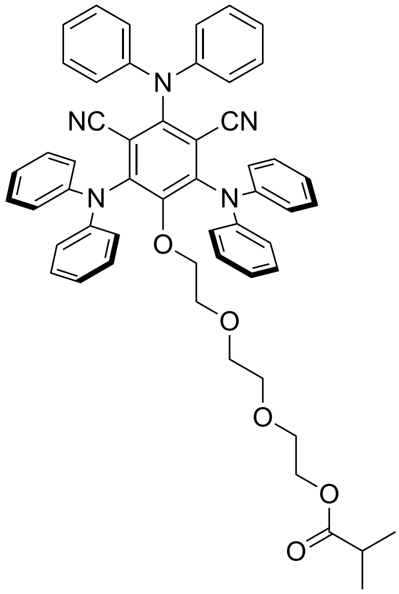

According to **general procedure F** using 86.5 mg of 3DPATEGIPN (0.1 mmol), 12 μL of isobutyryl chloride, 16 μL of triethylamine (TEA) and 0.7 mL of dry THF. Column chromatography with DCM/EtOAc, 10-30% EtOAc as gradient. 23.0 mg of product obtained (27% yield), yellow solid.

^{1}H NMR (400 MHz, $CDCl_3$): δ (ppm) 7.30-7.23 (m, 12H), 7.08-6.98 (m, 18H), 4.19-4.15 (m, 2H), 3.74 (t, *J* = 5.5 Hz, 2H), 3.56 (t, *J* = 5.7, 4.1 Hz, 2H), 3.33 (t, *J* = 5.7, 4.1 Hz, 2H), 3.06 – 3.01 (m, 2H), 2.88 (t, *J* = 5.5 Hz, 2H), 2.56 (hept, *J* = 7.0 Hz, 1H), 1.17 (d, *J* = 7.0 Hz, 6H).

^{13}C-NMR (100 MHz, CDCl$_3$): δ (ppm) 151.5, 150.9, 148.5, 145.7, 145.6, 129.4, 129.4, 124.1, 123.9, 122.7, 122.4, 113.1, 111.2, 72.4, 70.5, 70.4, 69.2, 68.9, 63.4, 34.0, 19.1

3(BrDPA)IPN-^{i}but *(2,4,6 Tris(4-4'dibromodiphenylamino)-5-tryethylenglicolisobutyrate isophthalonitrile)*

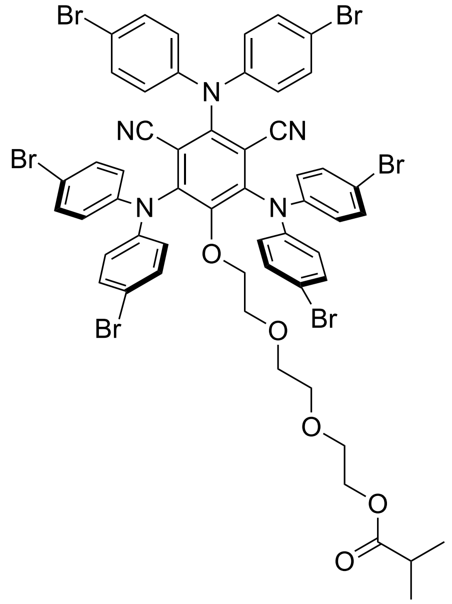

According to **general procedure F** using 25.0 mg of 3(BrDPA)TEGIPN (0.02 mmol), 2.5 μL of isobutyryl chloride, 3.5 μL of triethylamine (TEA) and 0.26 mL of dry THF (0.075 M). Column chromatography with DCM/EtOAc, 10-30% EtOAc as gradient. 13.2 mg of product obtained (50% yield), yellow solid.

^{1}H NMR (400 MHz, CDCl$_3$): δ (ppm) 7.38 (m, 12H), 6.81 (m, 12H), 4.18 (t, *J* = 5.0 Hz, 2H), 3.71 (m, 2H), 3.59 (t, *J* = 5.0 Hz, 2H), 3.39 (m, 2H), 3.18 (m, 2H), 3.02 (m, 2H), 2.55 (hept, 1H), 1.15 (d, *J*=6 Hz, 6H)

3(OMeDPA)IPN-^{i}but *(2,4,6 Tris(4-4'dimethoxydiphenylamino)-5-tryethylenglicolisobutyrate isophthalonitrile)*

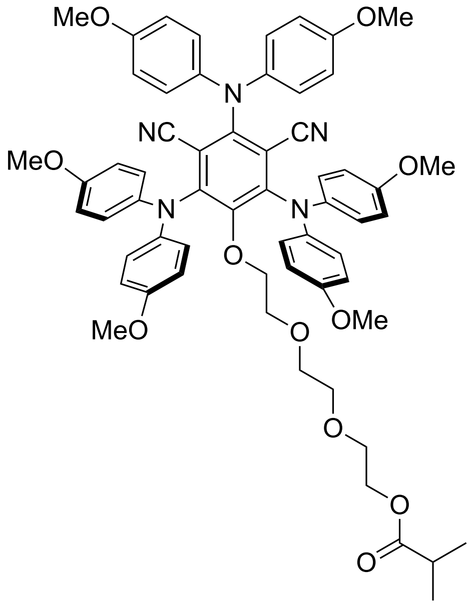

According to **general procedure F** using 63.0 mg of 3(OMeDPA)TEGIPN (0.07 mmol), 8 μL of isobutyryl chloride, 12 μL of triethylamine (TEA) and 0.5 mL of dry THF. Column chromatography with DCM/EtOAc, 10-50% EtOAc as gradient. 39.0 mg of product obtained (54% yield), red solid.

^{1}H NMR (400 MHz, $CDCl_3$): δ (ppm) 6.93-6.84 (m, 12H), 6.84-6.72 (m, 12H), 4.15 (m, 2H), 3.76 (s, 18H), 3.66 (t, 2H), 3.56 (t, 2H), 3.37-3.32 (m, 2H), 3.14-3.08 (m, 2H), 2.90 (t, 2H), 2.61-2.49 (hept, 1H), 1.14 (d, *J* = 7.0 Hz, 6H).

^{13}C-NMR (100 MHz, $CDCl_3$): δ (ppm) 155.9, 152.1, 148.9, 139.7, 124.0, 123.5, 114.5, 113.7, 108.5, 76.7, 71.9, 70.4, 70.3, 69.1, 68.9, 63.3, 55.4, 55.4, 33.9, 19.0.

3(BrCz)IPN-^{i}but *(2,4,6 Tris(3,6-dibromo-carbazol-9-yl)-5-tryethylenglicolisobutyrate isophthalonitrile)*

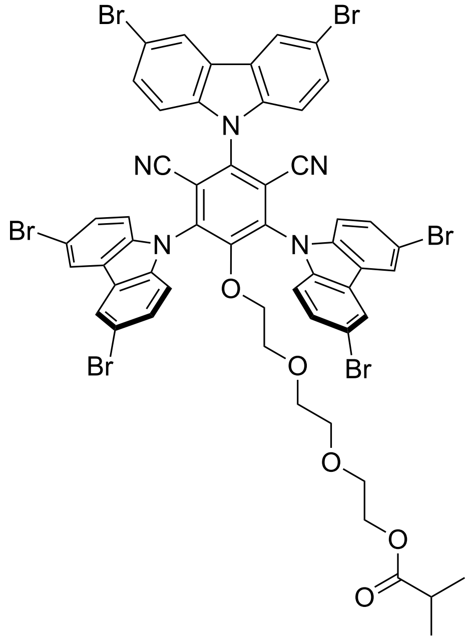

According to **general procedure F** using 148.6 mg of 3(BrCz)TEGIPN (0.12 mmol), 20 μL of isobutyryl chloride, 14 μL of triethylamine (TEA) and 0.80 mL of dry THF. Column chromatography with DCM/EtOAc, 10-30% EtOAc as gradient. 60.6 mg of product obtained (42% yield), yellow solid.

^{1}H NMR (400 MHz, $CDCl_3$): δ (ppm) 8.24 (m, 6H), 7.68 (m, 6H), 7.18 (m, 6H), 4.17-4.06 (m, 2H), 3.54-3.41 (m, 2H), 2.97 (m, 4H), 2.64 (m, 2H), 2.60 (m, 2H), 2.50 (hept, *J* = 7.0 Hz, 1H), 1.10 (d, *J* = 7.0 Hz, 6H).

^{13}C-NMR (100 MHz, $CDCl_3$): δ (ppm) 155.0, 139.3, 139.1, 138.3, 138.2, 130.5, 130.4, 125.2, 124.4, 124.1, 116.1, 115.6, 111.8, 110.7, 74.1, 69.9, 69.4, 69.1, 62.9, 33.9, 19.0.

3(OMeCz)IPN-^{i}but *(2,4,6 Tris(3,6-dimethoxy-carbazol-9-yl)-5-tryethylenglicolisobutyrate isophthalonitrile)*

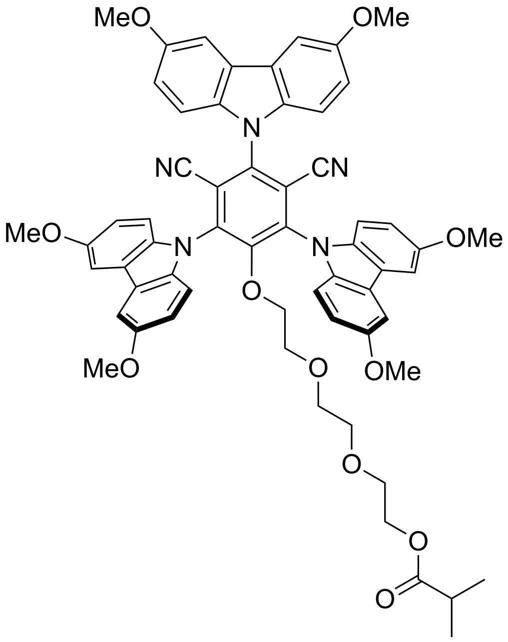

According to **general procedure F** using 75.0 mg of 3(OMeCz)TEGIPN (0.08 mmol), 9 µL of isobutyryl chloride, 13 µL of triethylamine (TEA) and 0.53 mL of dry THF. Column chromatography with DCM/EtOAc, 10-50% EtOAc as gradient. 30 mg of product obtained (37% yield), red solid.

^{1}H NMR (400 MHz, $CDCl_3$): δ (ppm) 7.56 (m, 6H), 7.27 (m, 4H), 7.17 (m, 6H), 4.11-4.04 (m, 2H), 3.97 (m, 18H), 3.43-3.34 (m, 2H), 2.98-2.91 (m, 4H), 2.57 (m, 2H), 2.56 (m, 2H), 2.51 (hept, 1H), 1.12 (d, *J* = 7.0 Hz, 6H).

^{13}C-NMR (100 MHz, $CDCl_3$): δ (ppm) 155.4, 154.1, 141.0, 139.3, 135.8, 134.9, 125.2, 115.7, 115.0, 111.7, 111.3, 110.3, 103.9, 103.6, 73.9, 69.9, 69.7, 69.2, 68.9, 63.1, 33.8, 18.9.

3DPAIPN-MA *(2,4,6 Tris(diphenylamino)-5-tryethylenglicolmethacrylate isophthalonitrile)*

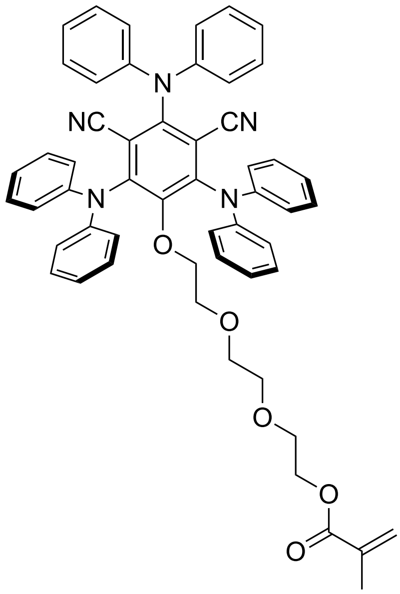

According to **general procedure G** using 207.0 mg of 3DPATEGIPN (0.25 mmol), 27 μL of methacryloyl chloride, 44 μL triethylamine (TEA) and 2.0 mL of dry THF. Column chromatography with DCM/EtOAc, 10-20% EtOAc as gradient. 139 mg of product obtained (58% yield), yellow solid.

^{1}H NMR (400 MHz, $CDCl_3$): δ (ppm) 7.26 (m, 12H), 7.08-6.97 (m, 18H), 6.12 (s, 1H), 5.57 (t, 1H), 4.28-4.22 (m, 2H), 3.74 (t, *J* = 5.5 Hz, 2H), 3.61 (t, *J* = 4.8 Hz, 2H), 3.34 (m, 2H), 3.04 (t, *J* = 4.8 Hz, 2H), 2.88 (t, *J* = 5.5 Hz, 2H), 1.95 (s, 3H).

^{13}C-NMR (100 MHz, $CDCl_3$): δ (ppm) 151.5, 150.9, 148.5, 145.7, 145.6, 136.3, 129.4, 129.4, 122.4, 113.1, 111.2, 72.5, 70.5, 70.4, 69.2, 68.9, 63.9, 31.1, 18.5.

3(BrDPA)IPN-MA *(2,4,6 Tris(4-4'dibromodiphenylamino)-5-tryethylenglicolmethacrylate isophthalonitrile)*

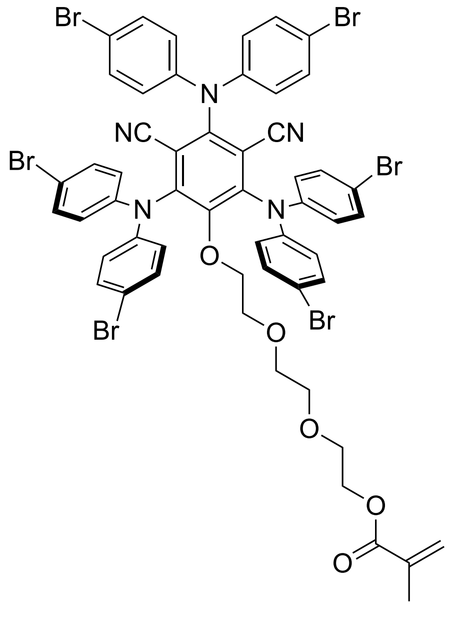

According to **general procedure G** using 1350.0 mg of 3(BrDPA)TEGIPN (1.0 mmol), 150 μL of methacryloyl chloride, 230 μL triethylamine (TEA) and 6.7 mL of dry THF. Column chromatography with DCM/EtOAc, 10-20% EtOAc as gradient. 659.5 mg of product obtained (50% yield), yellow solid.

^{1}H NMR (400 MHz, $CDCl_3$): δ (ppm) 7.49-7.35 (m, 12H), 6.84 (m, 12H), 6.12 (s, 1H), 5.58 (s, 1H), 4.28 (t, 2H), 3.74 (m, 2H), 3.66 (m, 2H), 3.46-3.39 (m, 2H), 3.25-3.17 (m, 2H), 3.04 (m, 2H), 1.95 (s, 3H).

^{13}C-NMR (100 MHz, $CDCl_3$): δ (ppm) 150.7, 150.3, 147.5, 144.1, 136.1, 132.7, 129.0, 128.5, 125.9, 124.1, 123.8, 117.6, 117.4, 112.6, 110.9, 73.1, 70.6, 70.3, 69.2, 63.6.

3(OMeDPA)IPN-MA *(2,4,6 Tris(4-4'dimethoxydiphenylamino)-5-tryethylenglicolmethacrylate isophthalonitrile)*

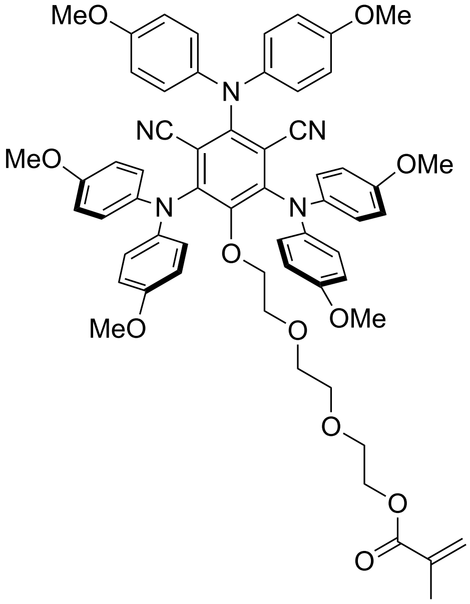

According to **general procedure G** using 1730.0 mg of 3(OMeDPA)TEGIPN (1.8 mmol), 260 μL of methacryloyl chloride, 0.4 mL triethylamine (TEA) and 12.0 mL of dry THF. Column chromatography with DCM/EtOAc, 10-20% EtOAc as gradient. 700.0 mg of product obtained (50% yield), red solid.

^{1}H NMR (400 MHz, $CDCl_3$): δ (ppm) 6.94-6.86 (m, 12H), 6.80-6.70 (m, 12H), 6.09 (s, 1H), 5.54 (s, 1H), 4.23 (t, *J* = 5.8, 2H), 3.75 (m, 18H), 3.73-3.65 (m, 2H), 3.60 (m, 2H), 3.41-3.33 (m, 2H), 3.15 – 3.06 (m, 2H), 2.91 (t, *J* = 5.8 Hz, 2H), 1.92 (t, *J* = 1.3 Hz, 3H).

^{13}C-NMR (100 MHz, $CDCl_3$): δ (ppm) 155.9, 152.1, 148.9, 148.5, 139.7, 139.5, 136.1, 125.8, 124.0, 123.5, 114.5, 113.7, 108.5, 71.9, 70.4, 69.1, 68.8, 64.3, 63.7, 55.4, 30.6, 18.3.

3(BrCz)IPN-MA *(2,4,6 Tris(3,6-dibromo-carbazol-9-yl)-5-tryethylenglicolmethacrylate isophthalonitrile)*

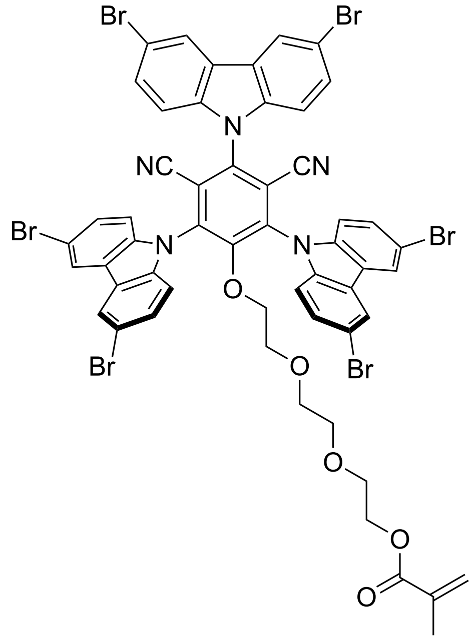

According to **general procedure G** using 611.0 mg of 3(BrCz)TEGIPN (0.5 mmol), 73 μL of methacryloyl chloride, 110 μL triethylamine (TEA) and 3.4 mL of dry THF. Column chromatography with DCM/EtOAc, 10-20% EtOAc as gradient. 328.3 mg of product obtained (50% yield), yellow solid.

^{1}H NMR (400 MHz, $CDCl_3$): δ (ppm) 8.21 (m, 6H), 7.69 (m, 6 H), 7.33-7.17 (m, 6H), 6.06 (s, 1H), 5.54 (s, 1H), 4.13 (m, 4H), 3.76 (m, 2H), 3.51 (m, 2H), 3.46, 3.39 (m, 4H), 1.91 (s, 3H).

^{13}C-NMR (100 MHz, $CDCl_3$): δ (ppm) 155.0, 139.3, 138.3, 130.5, 125.2, 124.4, 116.1, 115.6, 111.8, 110.7, 74.1, 69.9, 69.4, 62.9, 33.9, 19.0.

3(OMeCz)IPN-MA *(2,4,6 Tris(3,6-dimethoxy-carbazol-9-yl)-5-*tryethylenglicolmethacrylate *isophthalonitrile)*

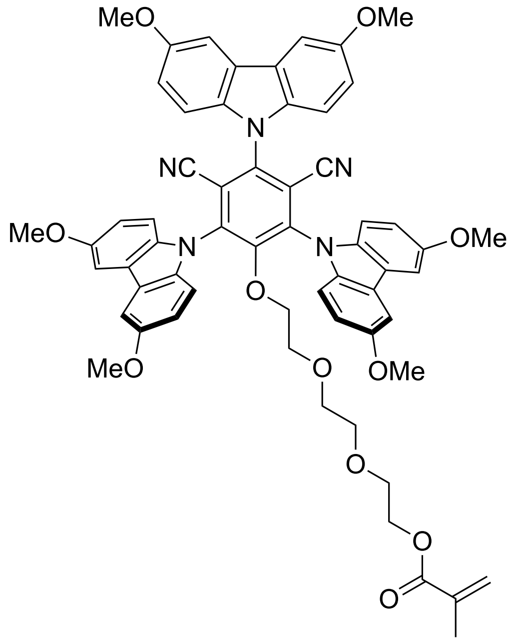

According to **general procedure G** using 710.0 mg of 3(OMeCz)TEGIPN (0.75 mmol), 110 μL of methacryloyl chloride, 170 μL triethylamine (TEA) and 5.0 mL of dry THF. Column chromatography with DCM/EtOAc, 10-20% EtOAc as gradient. 382.5 mg of product obtained (50% yield), red solid.

^{1}H NMR (400 MHz, $CDCl_3$): δ (ppm) 7.56 (m, 6H), 7.36-7.22 (m, 6H), 7.17 (m, 6H), 6.05 (s, 1H), 5.44 (m, 1H), 4.14 (m, 4H), 3.97 (s, 18H), 3.43 (m, 2H), 2.94 (t, 4H), 1.90 (s, 3H).

^{13}C-NMR (100 MHz, $CDCl_3$): δ (ppm) 155.4, 155.3, 134.9, 125.1, 115.7, 115.5, 111.3, 110.3, 103.9, 103.6, 73.9, 70.0, 69.7, 69.2, 68.8, 63.5, 60.4, 30.9, 18.3.

Figure 13. Some final monomers, from the left to the right: 3(OMeCz)IPN-MA, 3(OMeDPA)IPN-MA, 3(BrDPA)IPN-MA.

5.5 Photophysical Properties of Photocatalysts

All the photophysical properties were executed with the saturated versions of the photocatalyst-functionalized monomers.

5.5.1 Steady-State Absorption and Emission Spectra ($E_{0,0}$)

3DPAIPN-^{i}but

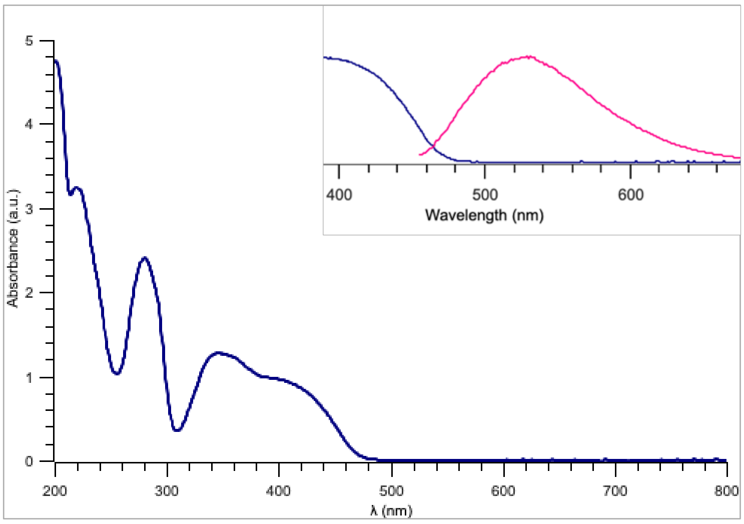

Figure 14. UV/Vis absorption and emission spectrum of 3DPAIPN-^{i}but in MeCN (10^{-4} M) measured at room temperature. λ_{exc}= 440 nm. Intersection point λ= 486 nm.

3(BrDPA)IPN-^{i}but

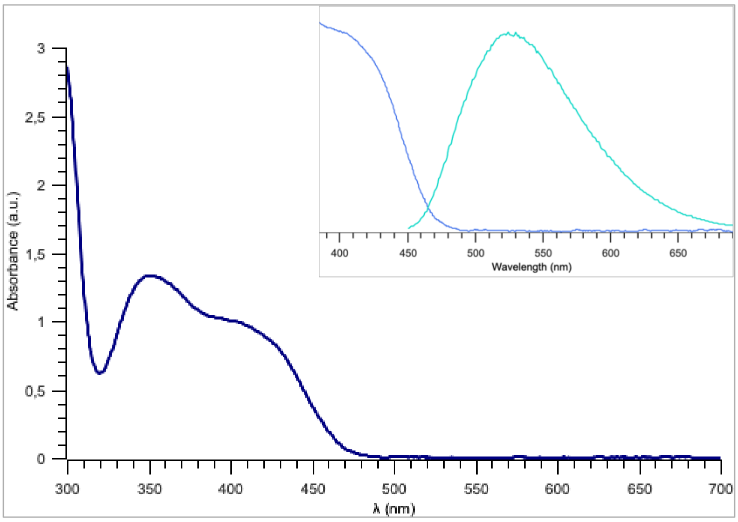

Figure 15. UV/Vis absorption and emission spectrum of 3(BrDPA)IPN-^{i}but in MeCN (10^{-4} M) measured at room temperature. λ_{exc}= 434 nm. Intersection point λ= 464 nm.

3(OMeDPA)IPN-^{i}but

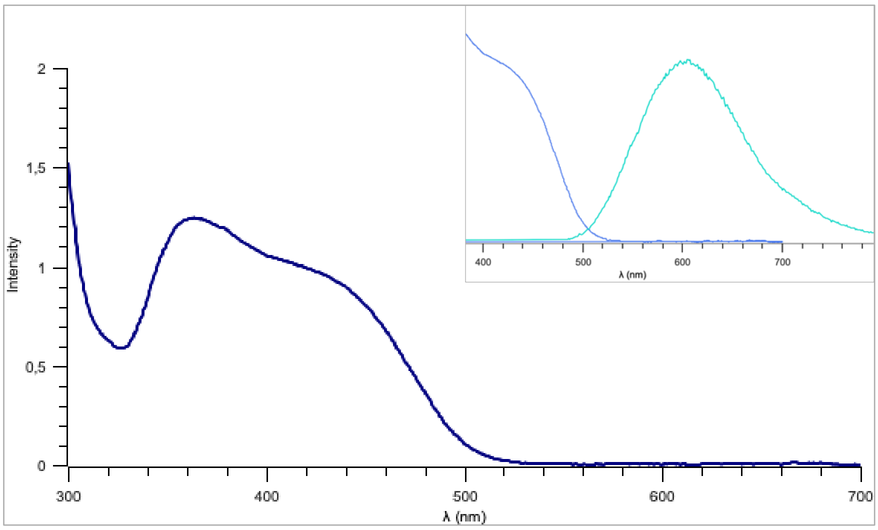

Figure 16. UV/Vis absorption and emission spectrum of 3(OMeDPA)IPN-^{i}but in MeCN (10^{-4} M) measured at room temperature. λ_{exc}= 465 nm. Intersection point λ= 505 nm.

3(BrCz)IPN-^{i}but

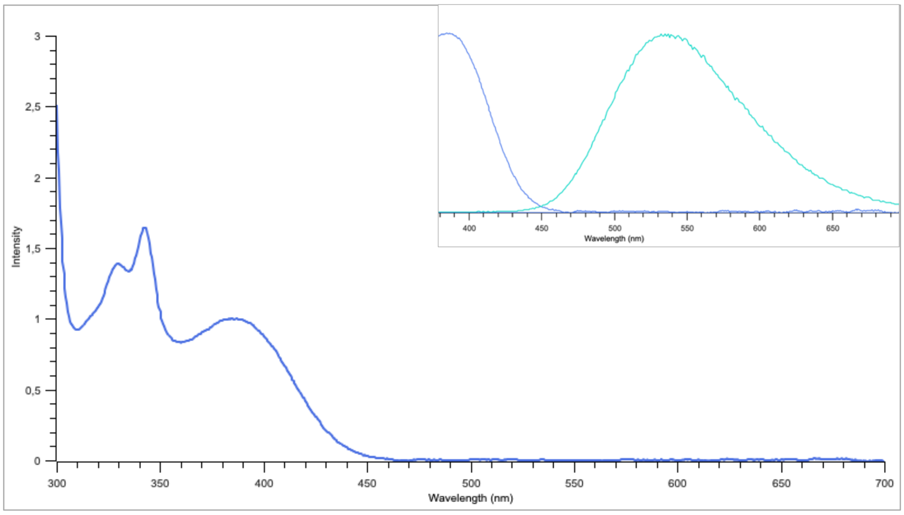

Figure 17. UV/Vis absorption and emission spectrum of 3(BrCz)IPN-^{i}but in MeCN (10^{-4} M) measured at room temperature. λ_{exc}= 390 nm. Intersection point λ= 450 nm.

3(OMeCz)IPN-^{i}but

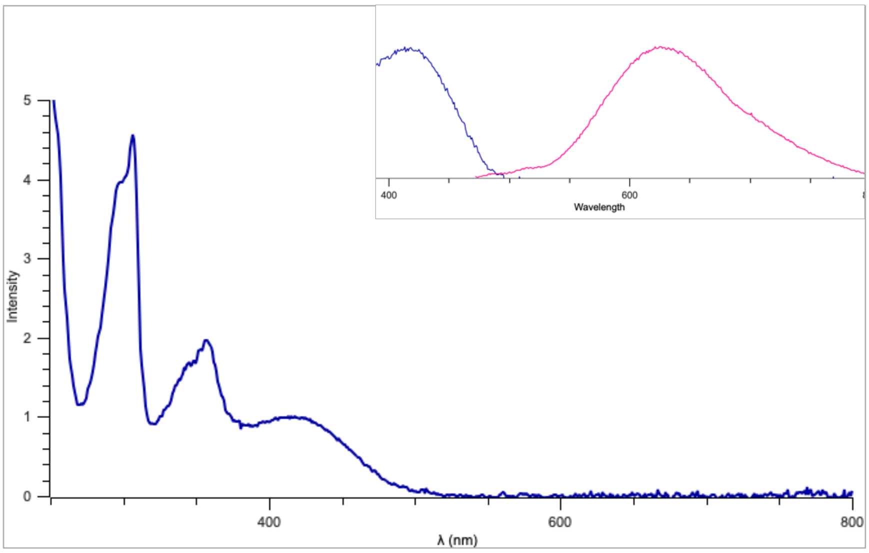

Figure 18. UV/Vis absorption and emission spectrum of 3(OMeCz)IPN-^{i}but in MeCN (10^{-4} M) measured at room temperature. λ_{exc}= 455 nm. Intersection point λ= 490 nm.

5.5.2 Cyclic Voltammetry

3DPAIPN-^{i}but

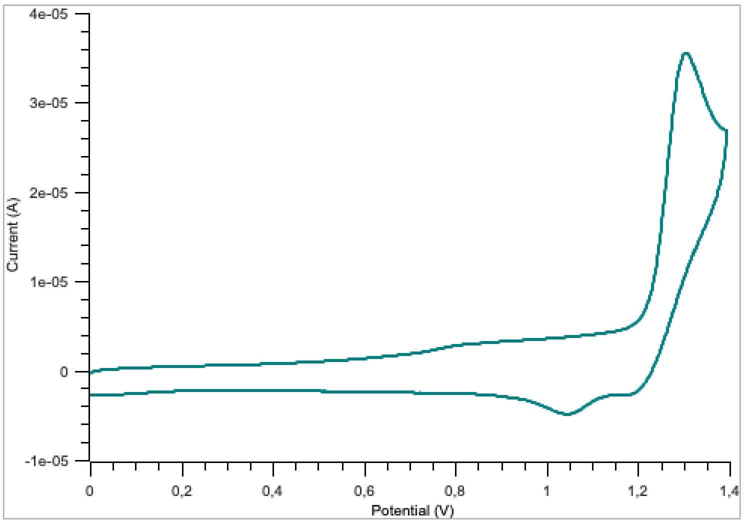

Figure 19. CV in the oxidation direction of 3DPAIPN-^{i}but in MeCN (10^{-3}M) using tetrabutylammonium hexafluorophosphate (TBAPF$_6$) 0.1 M as supporting electrolyte. Ferrocene was used as internal standard. Calculated $E_{p,a}$= +1.26 V vs SCE.

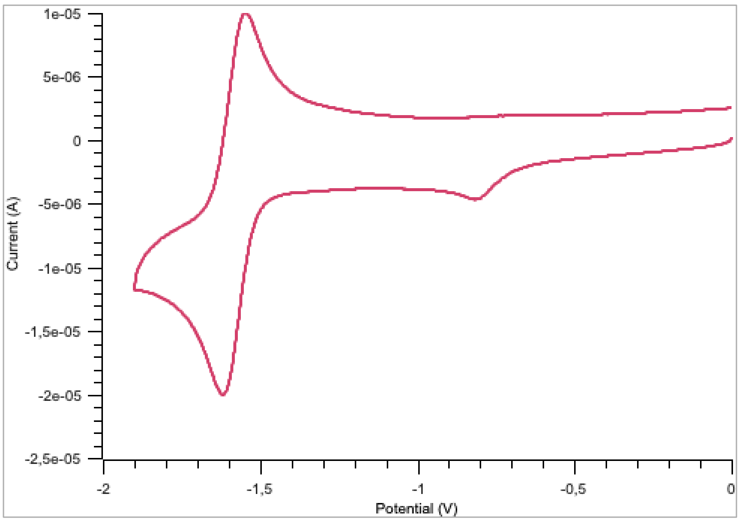

Figure 20. CV in the reduction direction of 3DPAIPN-^{i}but in MeCN (10^{-3}M) using tetrabutylammonium hexafluorophosphate (TBAPF$_6$) 0.1 M as supporting electrolyte. Ferrocene was used as internal standard. Calculated $E_{1/2}$= -1.63 V vs SCE.

3(BrDPA)IPN-^{i}but

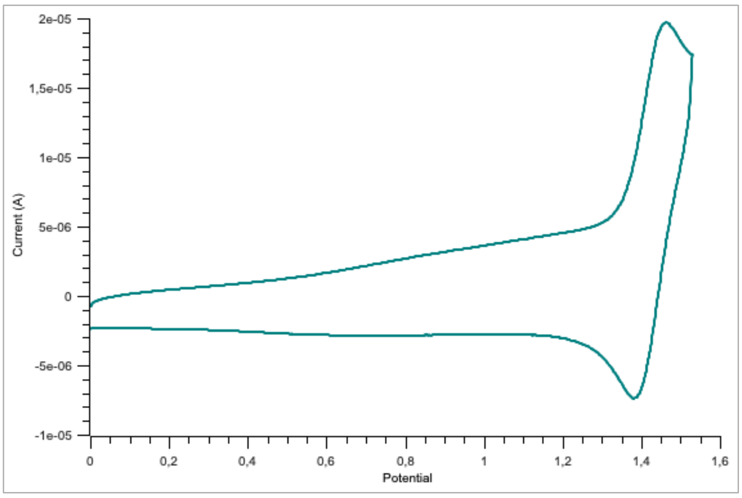

Figure 21. CV in the oxidation direction of 3(BrDPA)IPN-^{i}but in MeCN (10^{-3}M) using tetrabutylammonium hexafluorophosphate (TBAPF$_6$) 0.1 M as supporting electrolyte. Ferrocene was used as internal standard. Calculated $E_{p,a}$= +1.39 V vs SCE.

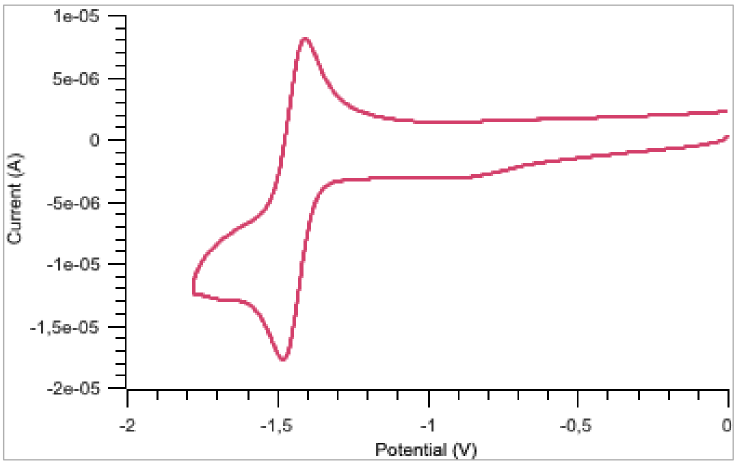

Figure 22. CV in the reduction direction of 3(BrDPA)IPN-^{i}but in MeCN (10^{-3}M) using tetrabutylammonium hexafluorophosphate (TBAPF$_6$) 0.1 M as supporting electrolyte. Ferrocene was used as internal standard. Calculated $E_{1/2}$= -1.48 V vs SCE.

3(OMeDPA)IPN-^{i}but

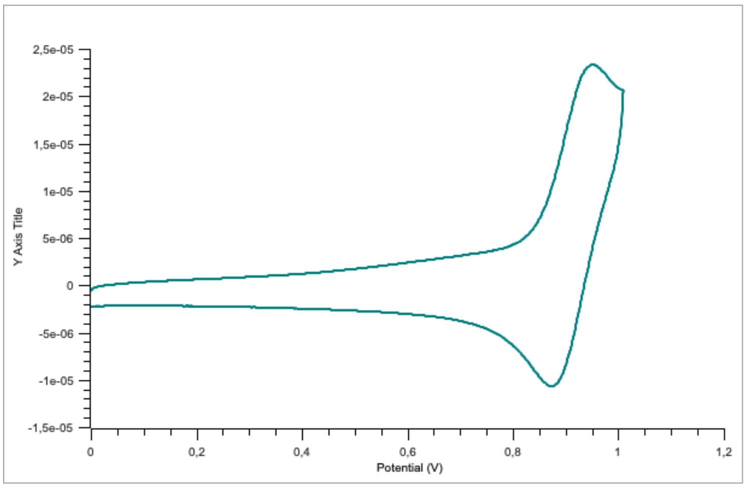

Figure 23. CV in the oxidation direction of 3(OMeDPA)IPN-^{i}but in MeCN (10^{-3}M) using tetrabutylammonium hexafluorophosphate ($TBAPF_6$) 0.1 M as supporting electrolyte. Ferrocene was used as internal standard. Calculated $E_{p,a}$= +0.87 V vs SCE.

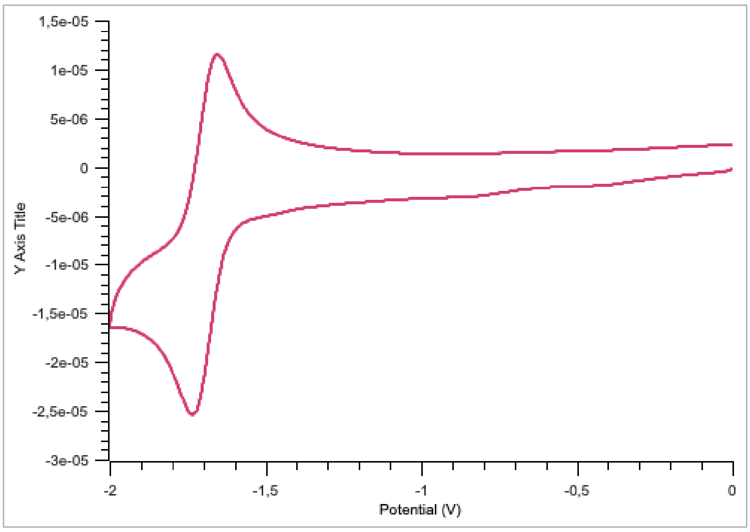

Figure 24. CV in the reduction direction of 3(OMeDPA)IPN-^{i}but in MeCN (10^{-3}M) using tetrabutylammonium hexafluorophosphate ($TBAPF_6$) 0.1 M as supporting electrolyte. Ferrocene was used as internal standard. Calculated $E_{1/2}$= -1.75 V vs SCE.

3(BrCz)IPN-^{i}but

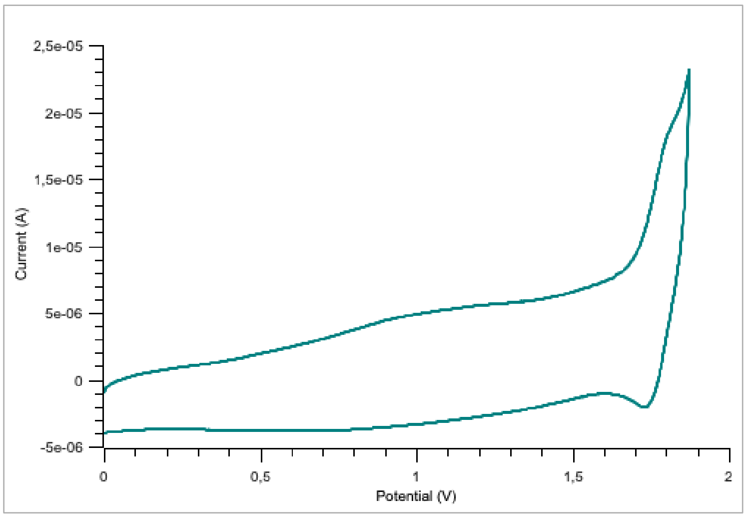

Figure 25. CV in the oxidation direction of 3(BrCz)IPN-^{i}but in MeCN (10^{-4}M) using tetrabutylammonium hexafluorophosphate (TBAPF$_6$) 0.1 M as supporting electrolyte. Ferrocene was used as internal standard. Calculated $E_{p,a}$= +1.75 V vs SCE.

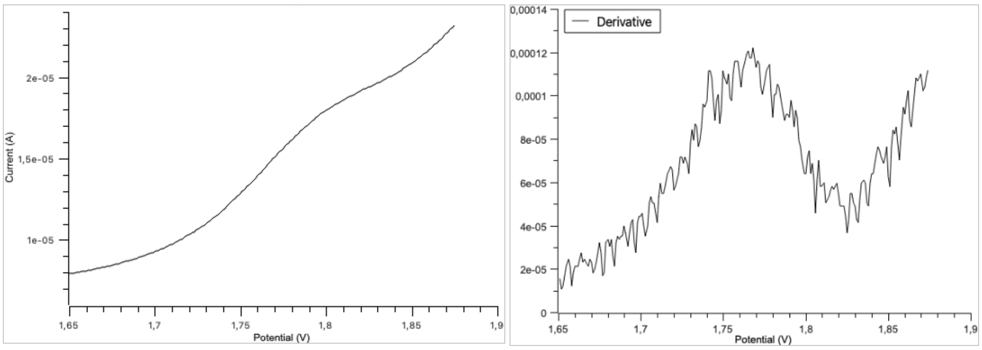

Figure 26. Value range of potential (V) indicating the presence of the peak (on the left) and derivative of the value range (on the right).

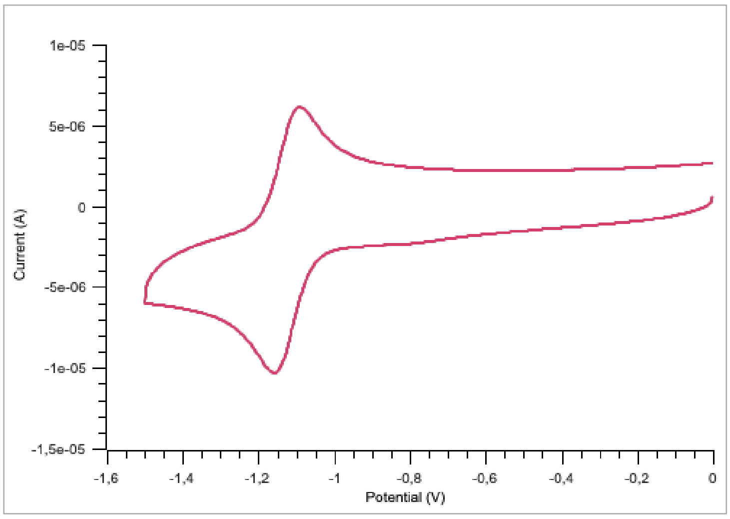

Figure 27. CV in the reduction direction 3(BrCz)IPN-^{i}but in MeCN (10^{-4}M) using tetrabutylammonium hexafluorophosphate (TBAPF$_6$) 0.1 M as supporting electrolyte. Ferrocene was used as internal standard. Calculated $E_{1/2}$= -1.17 V vs SCE.

3(OMeCz)IPN-^{i}but

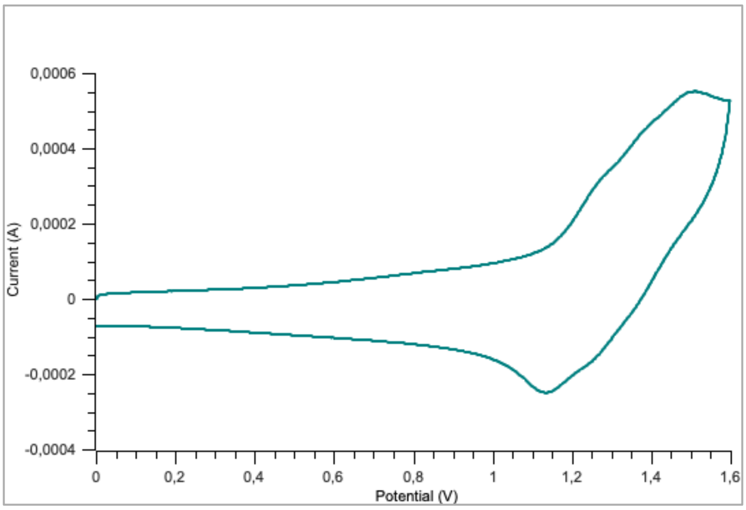

Figure 28. CV in the oxidation direction of 3(OMeCz)IPN-^{i}but in MeCN (10^{-3}M) using tetrabutylammonium hexafluorophosphate ($TBAPF_6$) 0.1 M as supporting electrolyte. Ferrocene was used as internal standard. Calculated $E_{p,a}$= +1.22 V vs SCE.

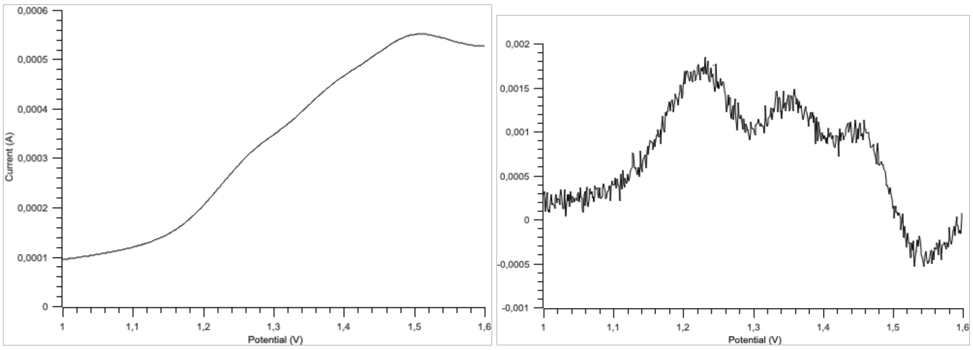

Figure 29. Value range of potential (V) indicating the presence of three peaks (on the left) and derivative of the value range (on the right).

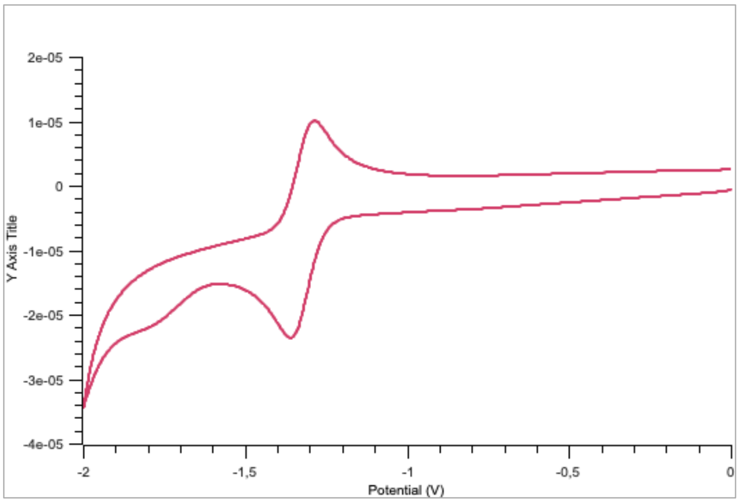

Figure 30. CV in the reduction direction 3(OMeCz)IPN-^{i}but in MeCN (10^{-3}M) using tetrabutylammonium hexafluorophosphate ($TBAPF_6$) 0.1 M as supporting electrolyte. Ferrocene was used as internal standard. Calculated $E_{1/2}$= -1.36 V vs SCE.

5.6 Polymerization in solution

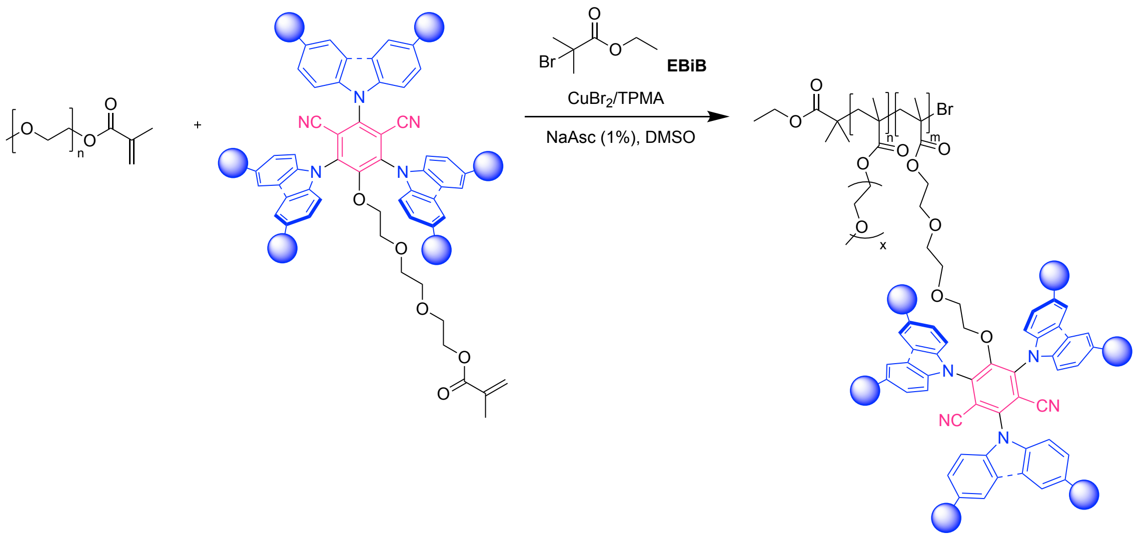

OEGMA **7** or **8** **p(OEGMA-*co*-3(“Donor-Group”)IPN-MA)**

Solution 50:50 $OEGMA_{300}$:DMSO, V_{tot}= 4 mL, NaAsc 5mM, PC 5%

In a vial equipped with a magnetic stir bar, 2.0 mL of $OEGMA_{300}$ (7 mmol, 1.75 M, prefiltered with basic alumina and PTFE filter), PC **7** or **8** (5 mol%, 0.35 mmol), 0.2 mL from a stock solution of EBiB 175 mM (8.75 mM), 0.2 mL from a stock solution of $CuBr_2$/TPMA 20/40 mM (1mM/2mM), 0.2 mL of internal standard (DMF) and 1.36 mL of DMSO were added and degassed with argon for 30 minutes. For the stock solution, DMSO must be used as solvent. In a vial, a stock solution of sodium ascorbate 500 mM (in distilled water) was degassed with argon for 30 minutes, separately. A small amount of the polymerization solution was taken as “time zero” t_0 for the ^{1}H-NMR kinetic. Finally, 0.04 mL from the stock solution of NaAsc (1% of V_{tot}, 5 mM) was added to start the polymerization. After 24h, or 48h referring to the % of conversion checked with ^{1}H-NMR, the polymers incorporating the PC were purified using 12-14 kDa dialysis membrane, for 2 days in 100% ACN.

Solution 20:80 $OEGMA_{500}$:DMSO, V_{tot}= 2 mL

In a vial equipped with a magnetic stir bar, 0.4 mL of $OEGMA_{500}$ (0.864 mmol, 432 mM, prefiltered with basic alumina and PTFE filter), 0.04 mL from a stock solution of EBiB 108 mM (2.16 mM), 0.04 mL from a stock solution of $CuBr_2$/TPMA 25/50 mM (0.5mM/1mM), 0.04 mL of internal standard (DMF) and 1.4 mL of DMSO were added and degassed with argon for 30 minutes. For the stock solution, DMSO must be used as solvent.
In a vial, a stock solution of sodium ascorbate 62.5 mM (in distilled water) was degassed with argon for 30 minutes, separately. A small amount of the polymerization solution was taken as “time zero” t_0 for the ^{1}H-NMR kinetic. Finally, 0.08 mL from the stock solution of NaAsc (4% of V_{tot}, 2.5 mM) was added to start the polymerization. After 24h the polymer was purified using 12-14 kDa dialysis membrane, for 2 days in 100% ACN.

1H-NMR spectra

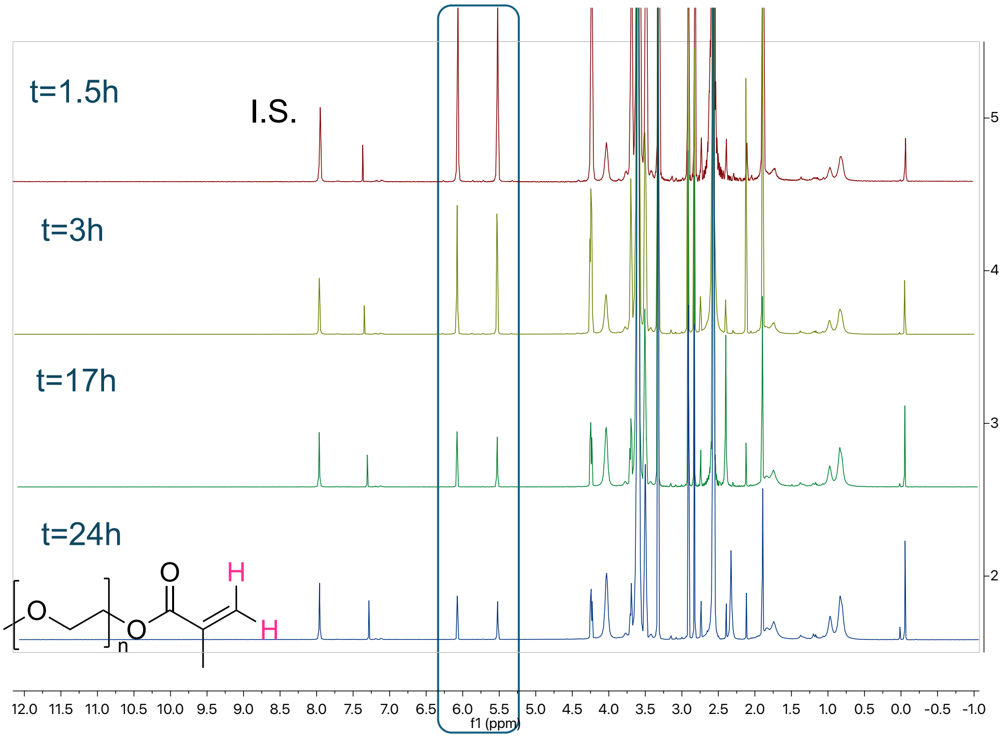

*Figure 31. ^{1}H-NMR spectra (400 MHz, $CDCl_3$) of the polymerization of **OEGMA$_{300}$** at different times (without PCs). The signal used as internal standard is the DMF signal at 7.90 ppm and for the polymer the decrease of the double bond signals were monitored (H, 5.98 and 5.44 ppm). 80% conversion after 24h.*

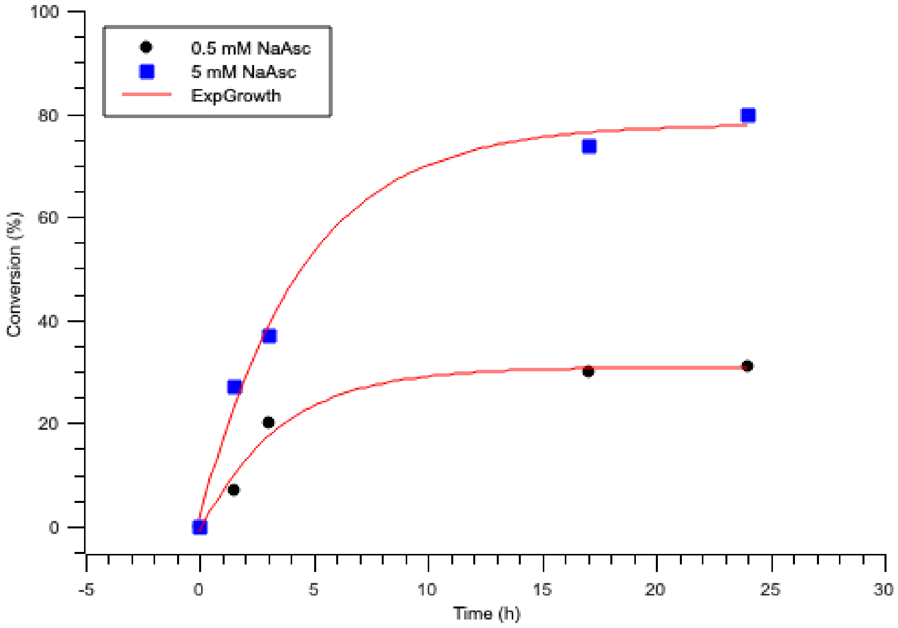

Figure 32. Polymeric conversion vs Time in kinetic study. Polymerization with 5 mM of NaAsc (80% conversion after 24 h) and 0.5 mM of NaAsc (40%conversion after 24h)

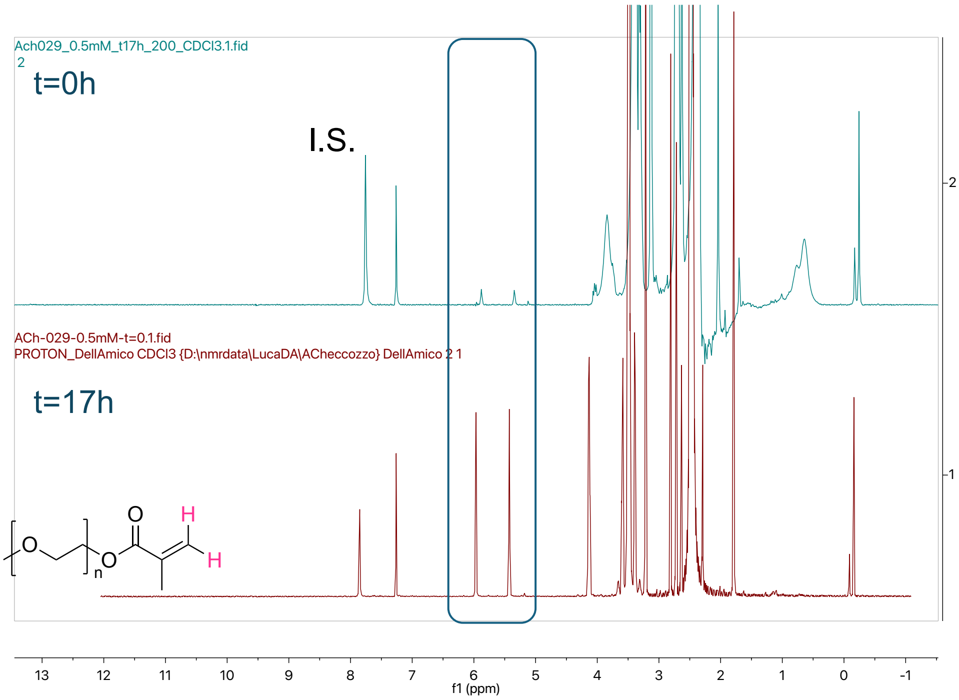

*Figure 33. ^{1}H-NMR spectra (400 MHz, CDCl$_3$) of the polymerization of **OEGMA$_{500}$** at different times (without PCs). The signal used as internal standard is the DMF signal at 7.90 ppm and for the polymer the decrease of the double bond signals were monitored (H, 5.98 and 5.44 ppm). 90% conversion after 17h.*

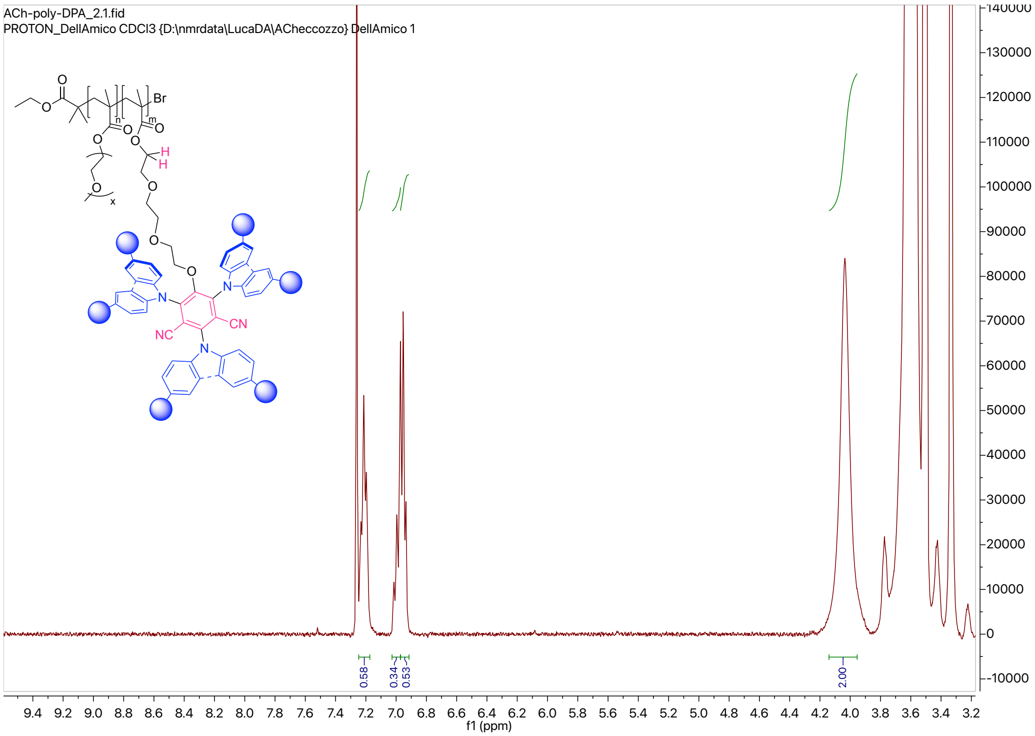

*Figure 34. ^{1}H-NMR spectrum (400 MHz, CDCl$_3$) of **poly(OEGMA-co-3DPAIPN-MA)**. The broad singlet at 4.17 ppm correspond to the first methylene of the glycolic chain (2H), while the two multiplets from 6.9 to 7.2 ppm correspond to the 30 aromatic protons of the diphenylamine.*

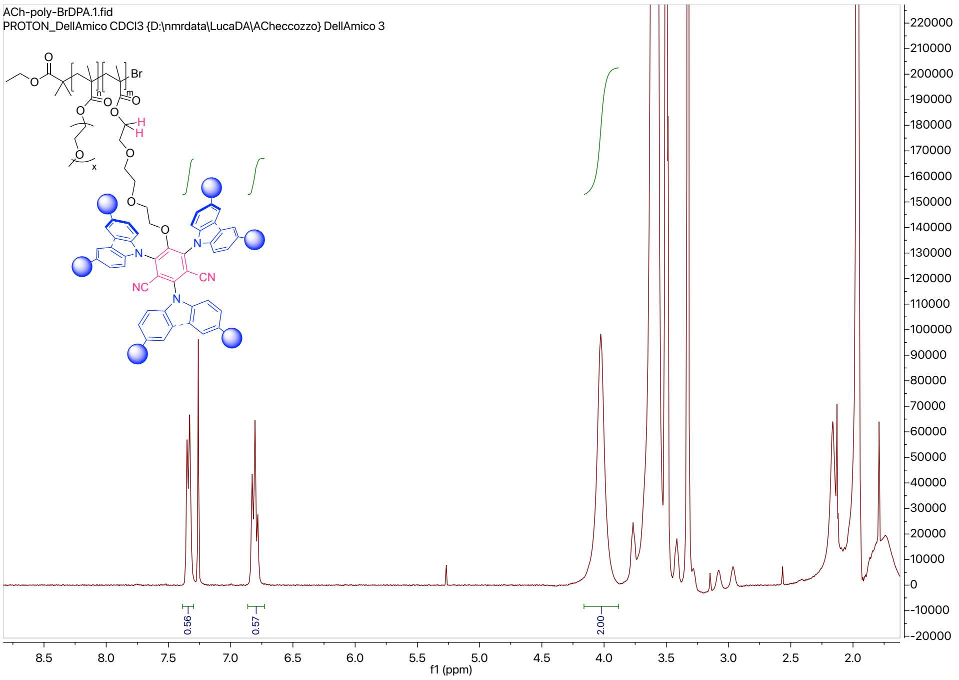

*Figure 35. ^{1}H-NMR spectrum (400 MHz, CDCl$_3$) of **poly(OEGMA-co-3(BrDPA)IPN-MA)**. The broad singlet at 4.17 ppm correspond to the first methylene of the glycolic chain (2H), while the two multiplets from 6.8 to 7.4 ppm correspond to the 24 aromatic protons of the 4,4'-dibromodiphenylamine.*

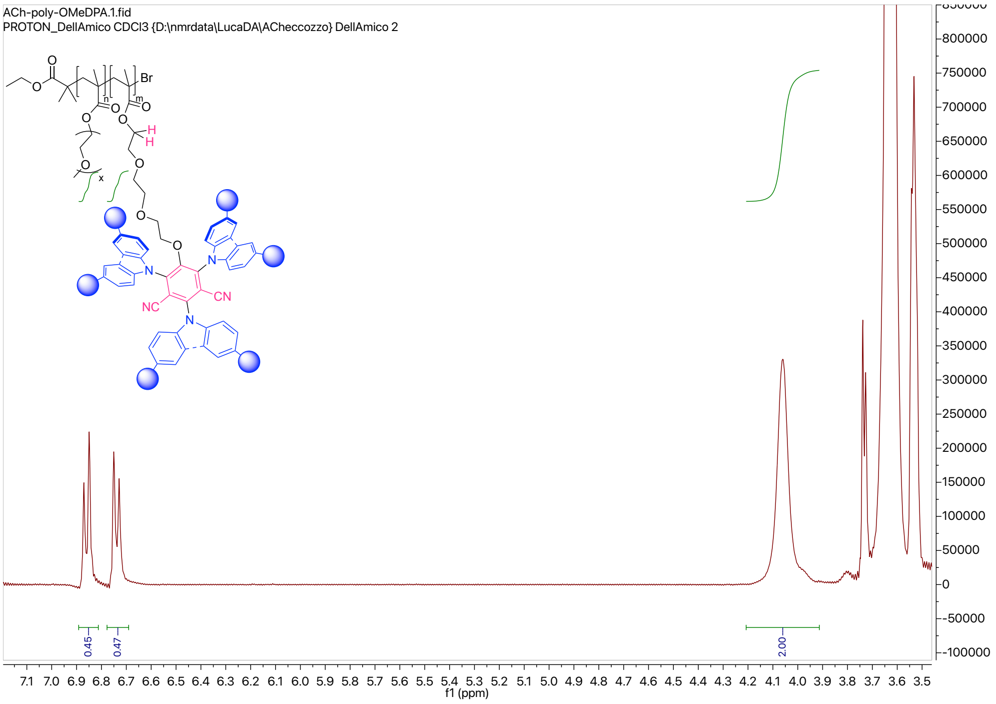

*Figure 36. ^{1}H-NMR spectrum (400 MHz, CDCl$_3$) of **poly(OEGMA-co-3(OMeDPA)IPN-MA)**. The broad singlet at 4.17 ppm correspond to the first methylene of the glycolic chain (2H), while the two multiplets from 6.7 to 6.9 ppm correspond to the 24 aromatic protons of the 4,4'-dimethoxydiphenylamine.*

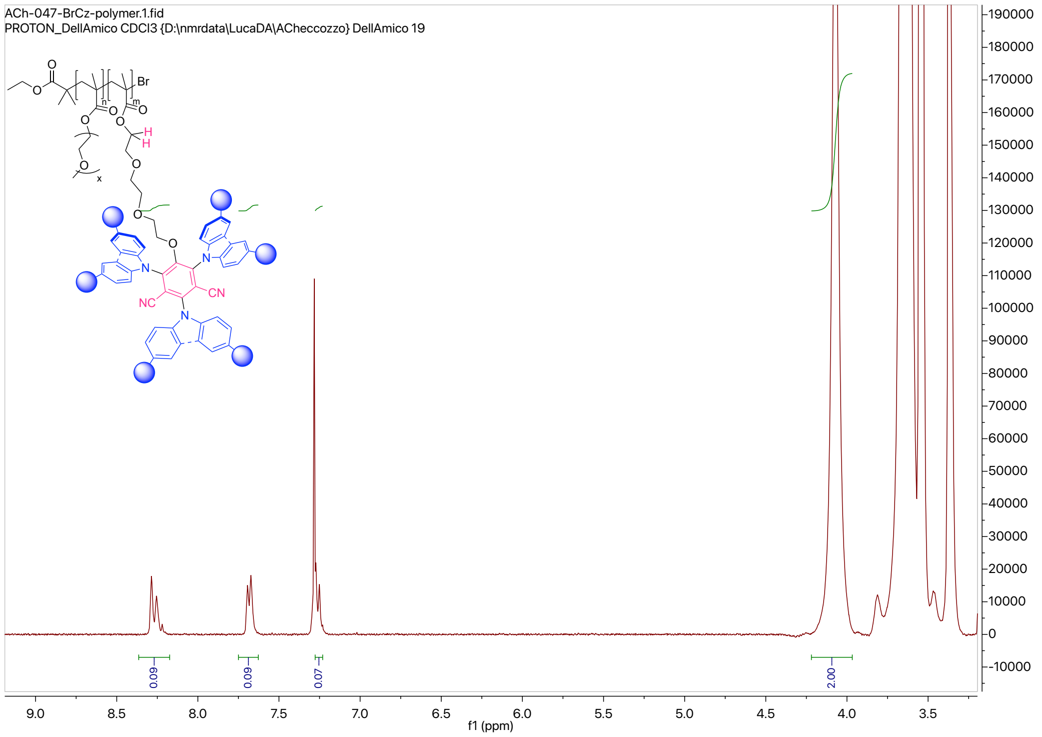

*Figure 37. ^{1}H-NMR spectrum (400 MHz, CDCl$_3$) of **poly(OEGMA-co-3(BrCz)IPN-MA)**. The broad singlet at 4.17 ppm correspond to the first methylene of the glycolic chain (2H), while the three multiplets from 7.2 to 8.3 ppm correspond to the 18 aromatic protons of the 3,6-dibromo-carbazole.*

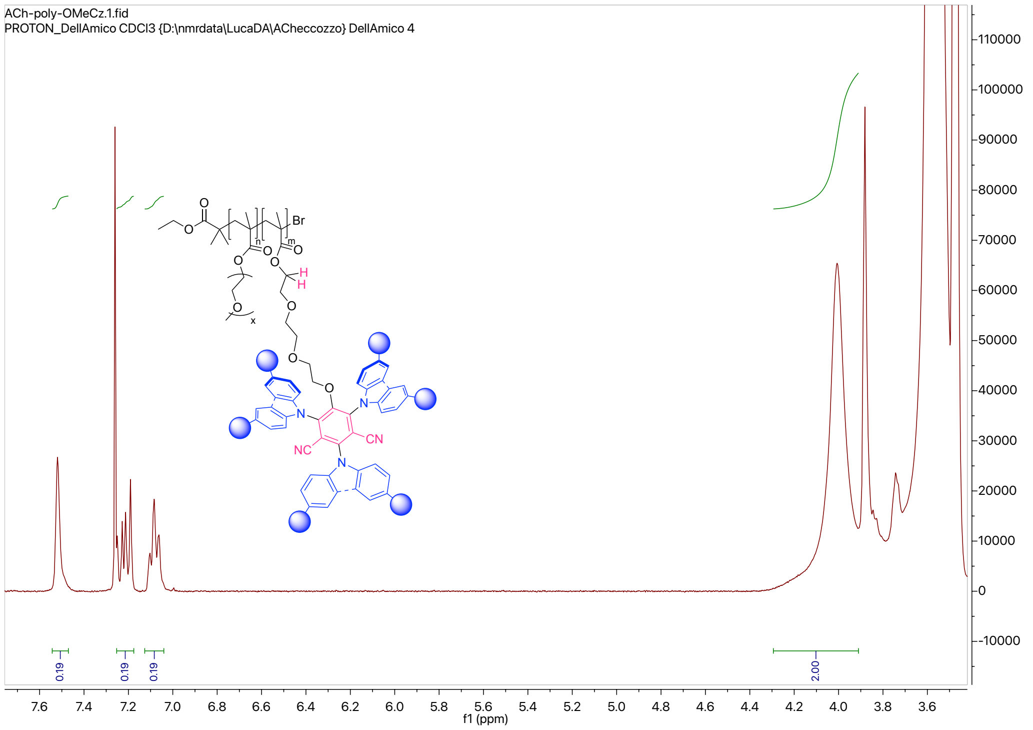

*Figure 38. ^{1}H-NMR spectrum (400 MHz, CDCl$_3$) of **poly(OEGMA-co-3(OMeCz)IPN-MA)**. The broad singlet at 4.17 ppm correspond to the first methylene of the glycolic chain (2H), while the three multiplets from 7.1 to 7.5 ppm correspond to the 18 aromatic protons of the 3,6-dimethoxy-carbazole.*

5.7 UV-Visible Calibration

3DPAIPN-^{i}but

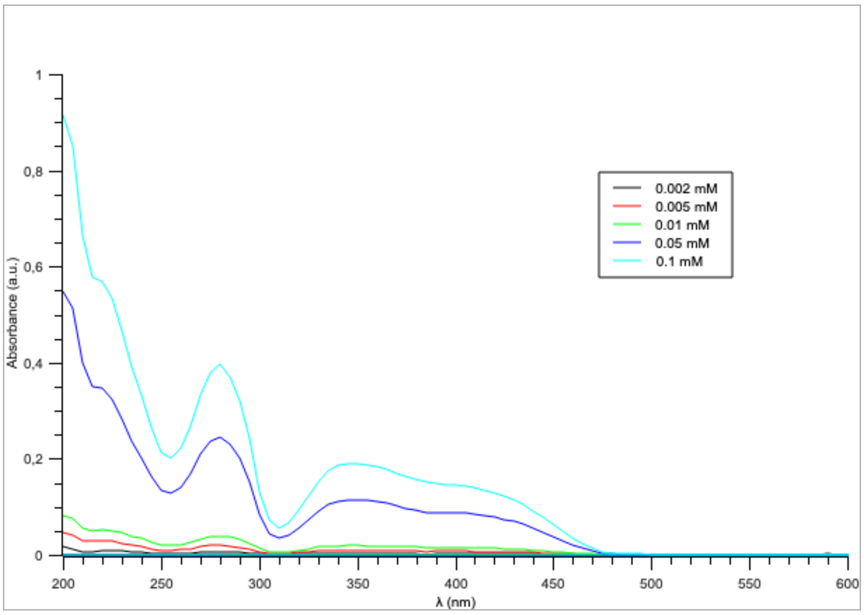

Figure 39. Absorption spectra at different concentrations of the monomer 3DPAIPN-^{i}but in ACN at room temperature.

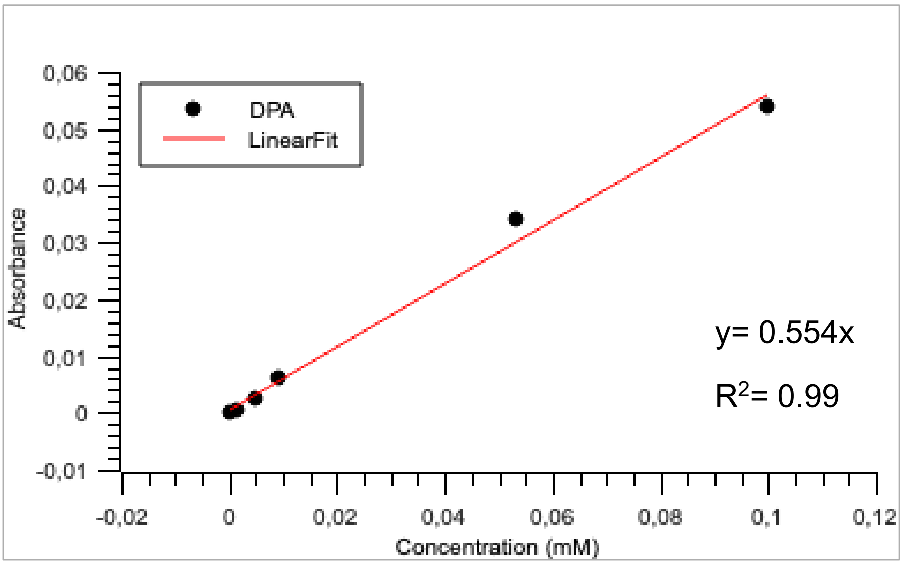

Figure 40. Absorbance values at 310 nm vs Concentration.

3(BrDPA)IPN-^{i}but

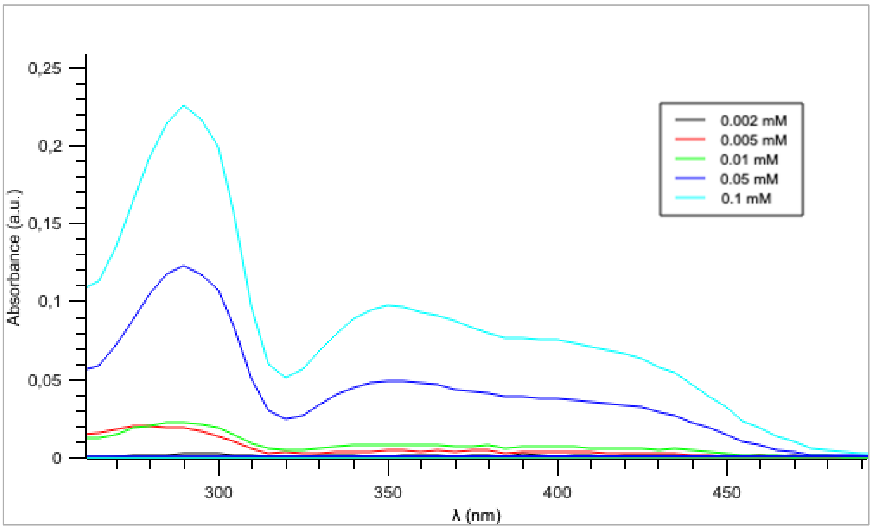

Figure 41. Absorption spectra at different concentrations of the monomer 3(BrDPA)IPN-^{i}but in ACN at room temperature.

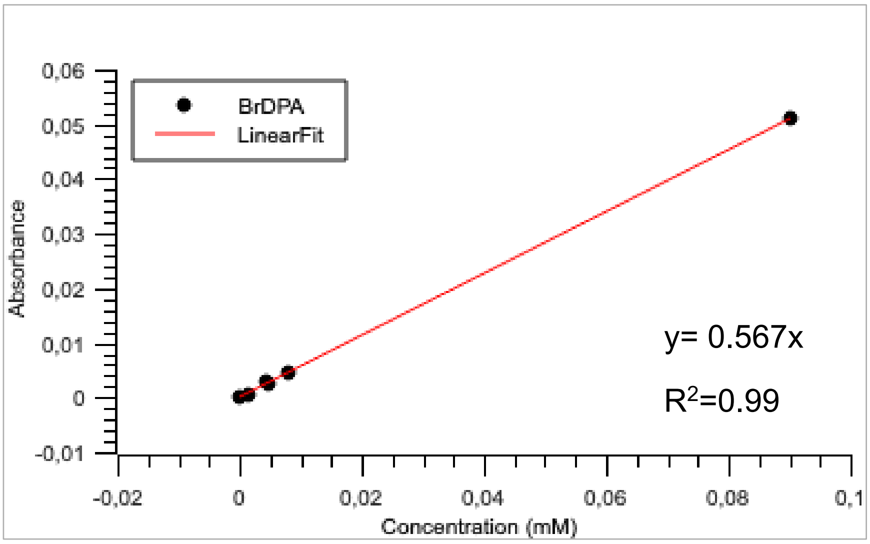

Figure 42. Absorbance values at 320 nm vs Concentration.

3(OMeDPA)IPN-^{i}but

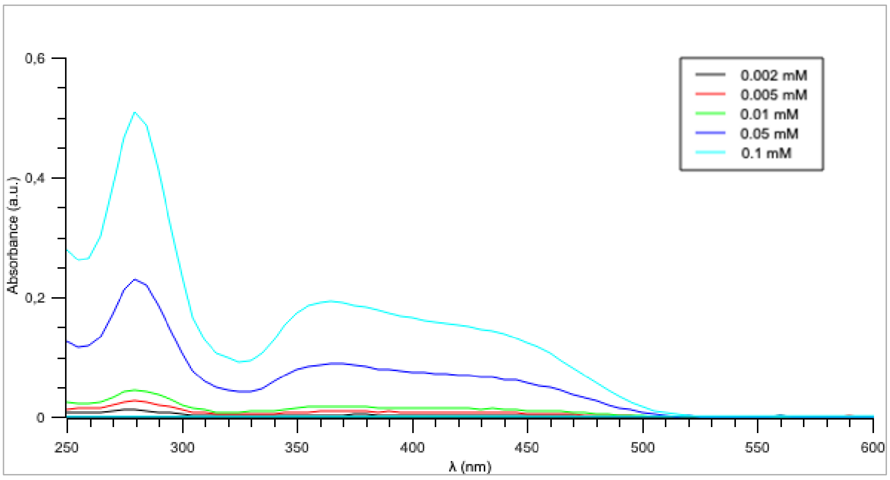

Figure 43. Absorption spectra at different concentrations of the monomer 3(OMeDPA)IPN-^{i}but in ACN at room temperature.

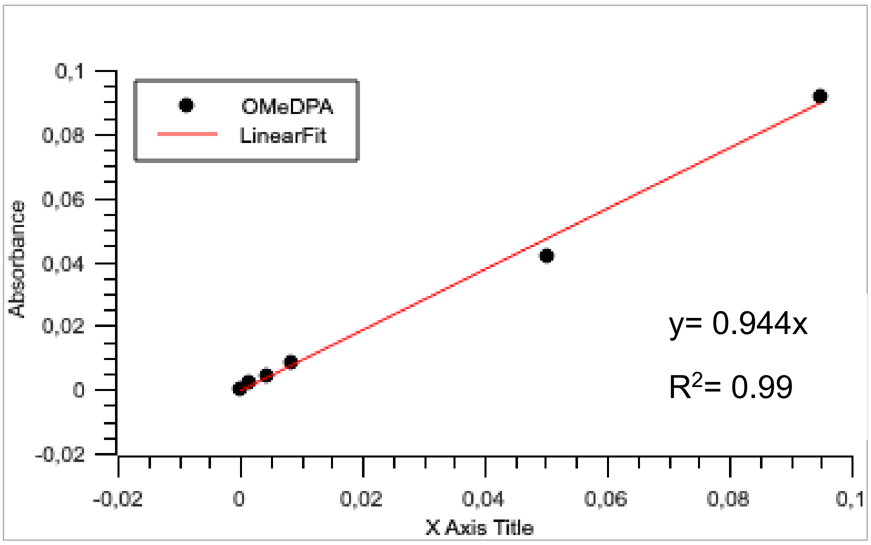

Figure 44. Absorbance values at 325 nm vs Concentration.

3(OMeCz)IPN-^{i}but

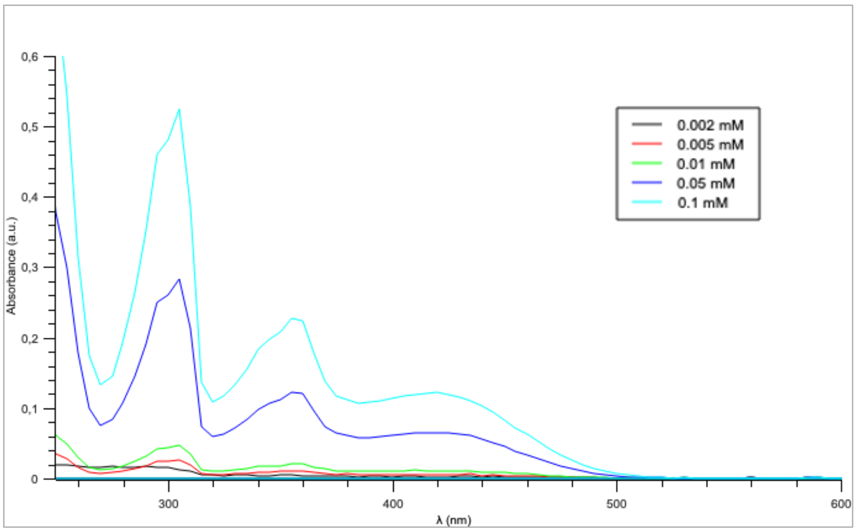

Figure 45. Absorption spectra at different concentrations of the monomer 3(OMeCz)IPN-^{i}but in ACN at room temperature.

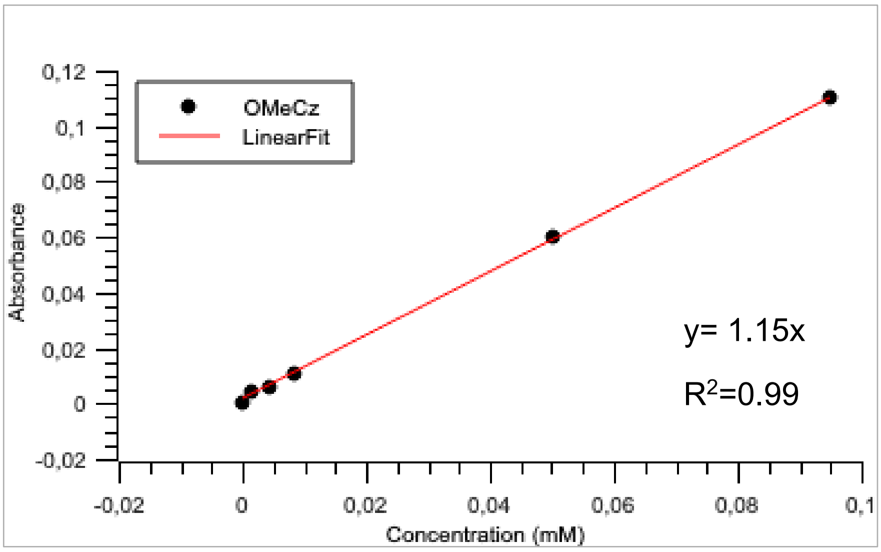

Figure 46. Absorbance values at 320 nm vs Concentration.

Absorption profile of polymers

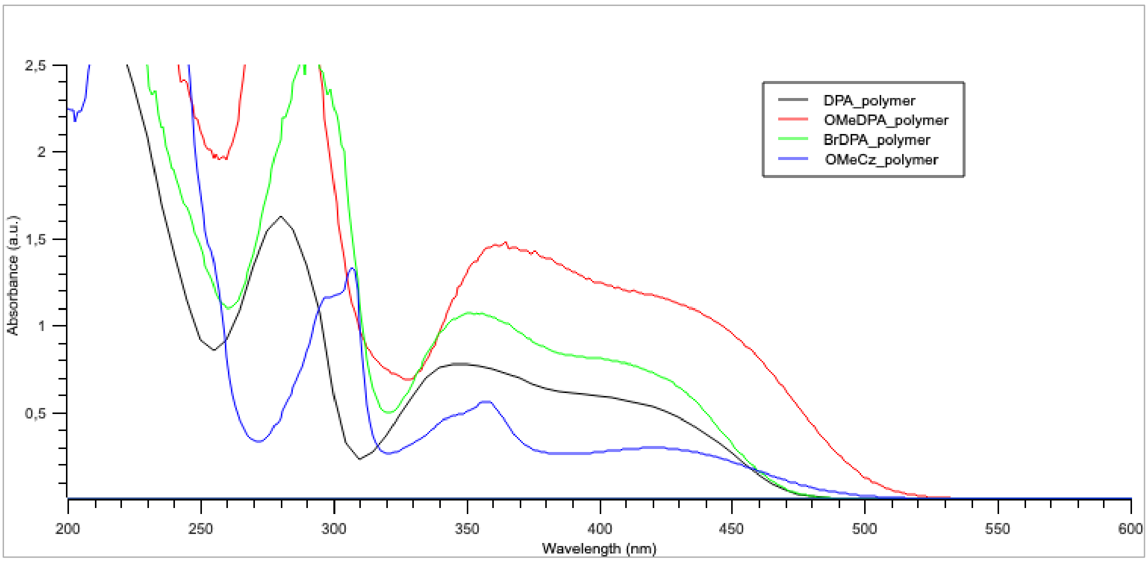

Figure 47. Absorption of the polymers in ACN at room temperature.

Polymer	**Concentration (solution)**	***λ (nm)***	**Absorbance**	**Conc. (mM)**	**mmol$_{PC}$/mg$_{polymer}$**
p(OEGMA-*co*-3DPAIPN-MA)	13 mg/mL	310	0.233	0.42	$3.23*10^{-5}$
p(OEGMA-*co*-3(BrDPA)IPN-MA)	7.8 mg/mL	320	0.485	0.85	$1.09*10^{-4}$
p(OEGMA-*co*-3(OMeDPA)IPN-MA)	7.8 mg/mL	325	0.681	0.72	$9.2*10^{-5}$
p(OEGMA-*co*-3(OMeCz)IPN-MA)	7.5 mg/mL	320	0.271	0.23	$3.1*10^{-5}$

Table 11. Absorbance of the polymers at minimum (λ), calculated concentration from the linear fits and calculated mmol of incorporated PCs vs mg of polymer.

5.8 General Procedures for Test Reactions

5.8.1 Giese-type addition

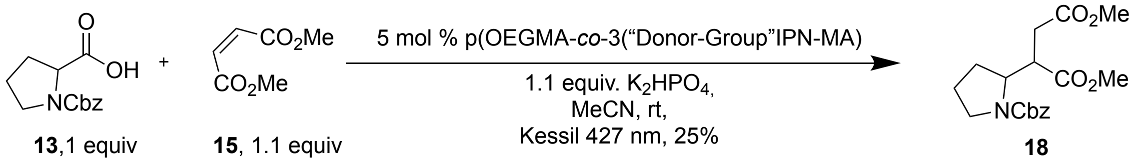

The procedure was followed according to literature[48]. An oven-dried 10 mL Schlenk flask with a glass cap and a magnetic stir bar was charged with the selected photocatalyst (0.005 mmol, 5 mol% cat. loading), Cbz-Pro-OH **13** (37.4 mg, 0.15 mmol, 1.0 equiv), methyl maleate **15** (25 µL, 0.17 mmol, 1.1 equiv), K_2HPO_4 (31.4 mg, 0.18 mmol, 1.1 equiv), and 3.75 mL of dry MeCN. The reaction mixture was degassed by using the freeze-pump- thaw technique, cycles (3×), then irradiated with Kessil lamp for 3.5h. The polymeric system was precipitate with diethyl ether. The product **18** was detected by ^{1}H-NMR from the crude of reaction and the yield was calculated using CH_2Br_2 as internal standard (5.25 µL, 0.075 mmol).

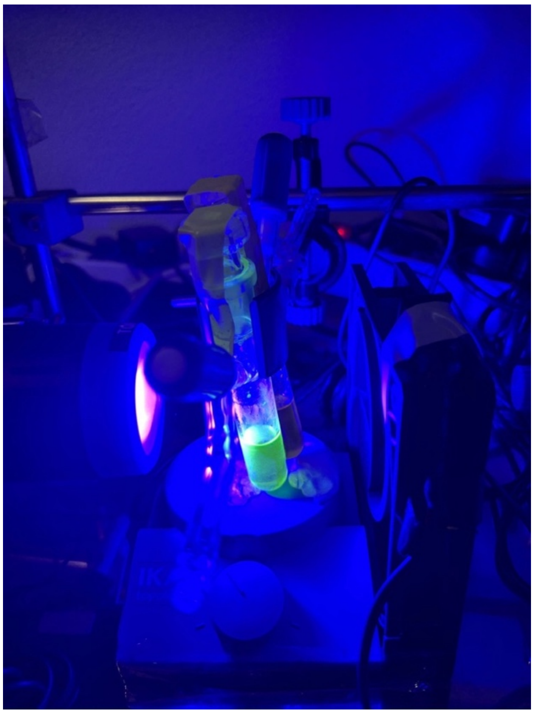

Figure 48. Photochemical setup for the Giese-type addition. The distance between the Schlenk and the Kessil lamp is 3 cm. The system is ventilated with a fan.

1H-NMR spectra

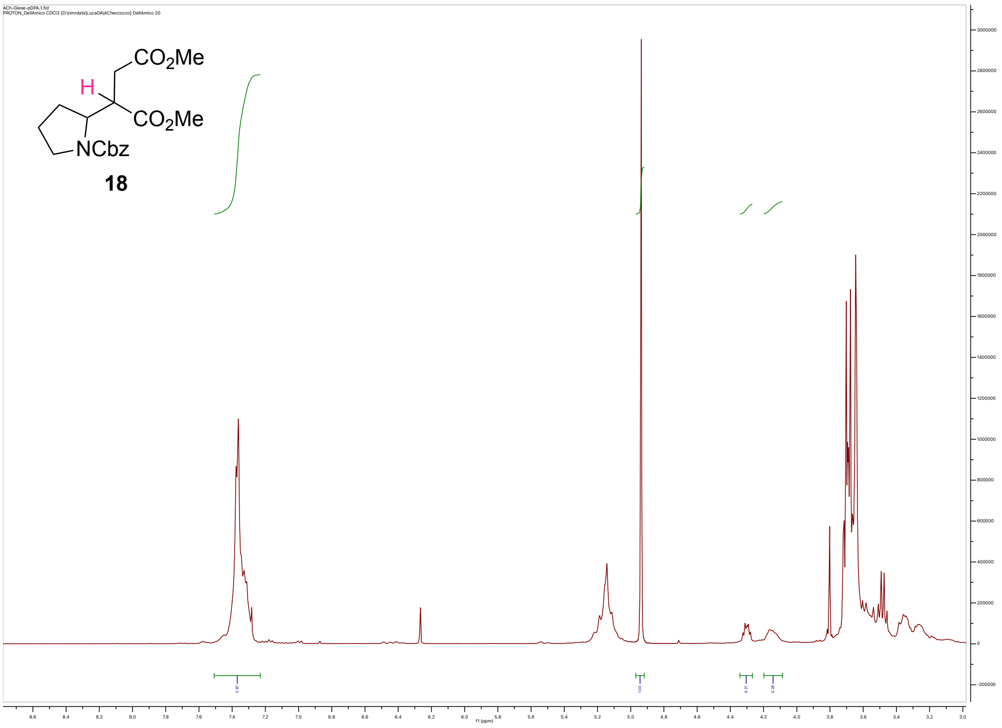

Figure 49. ^{1}H-NMR (400 MHz, CDCl$_3$) reaction crude of the Giese-type photoreaction with ***poly(OEGMA-co-3DPAIPN-MA)*** *as PC and CH$_2$Br$_2$ as internal standard (4.9 ppm, 2H). The highlighted proton H is the diagnostic one used for the calculation of the NMR yield which correspond to the two peaks, the* ***broad signal at 4.15 ppm*** *and the* ***multiplet at 4.30*** *due to the formation of the rotamers.*

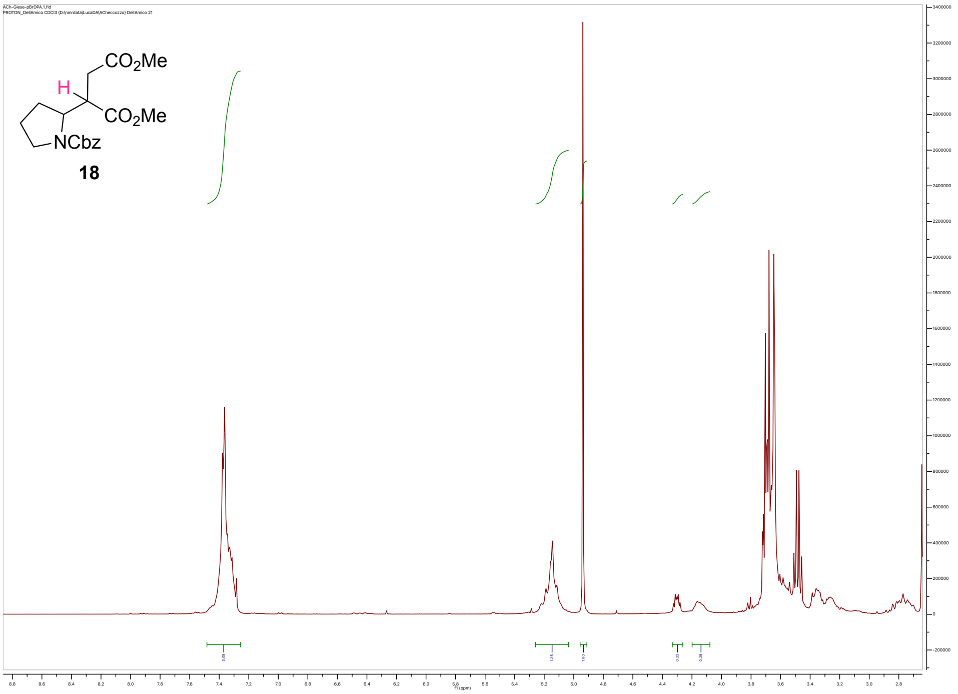

Figure 50. ^{1}H-NMR (400 MHz, CDCl$_3$) reaction crude of the Giese-type photoreaction with ***poly(OEGMA-co-3(BrDPA)IPN-MA)*** *as PC and CH$_2$Br$_2$ as internal standard (4.9 ppm, 2H). The highlighted proton H is the diagnostic one used for the calculation of the NMR yield which correspond to the two peaks, the* ***broad signal at 4.15 ppm*** *and the* ***multiplet at 4.30*** *due to the formation of the rotamers.*

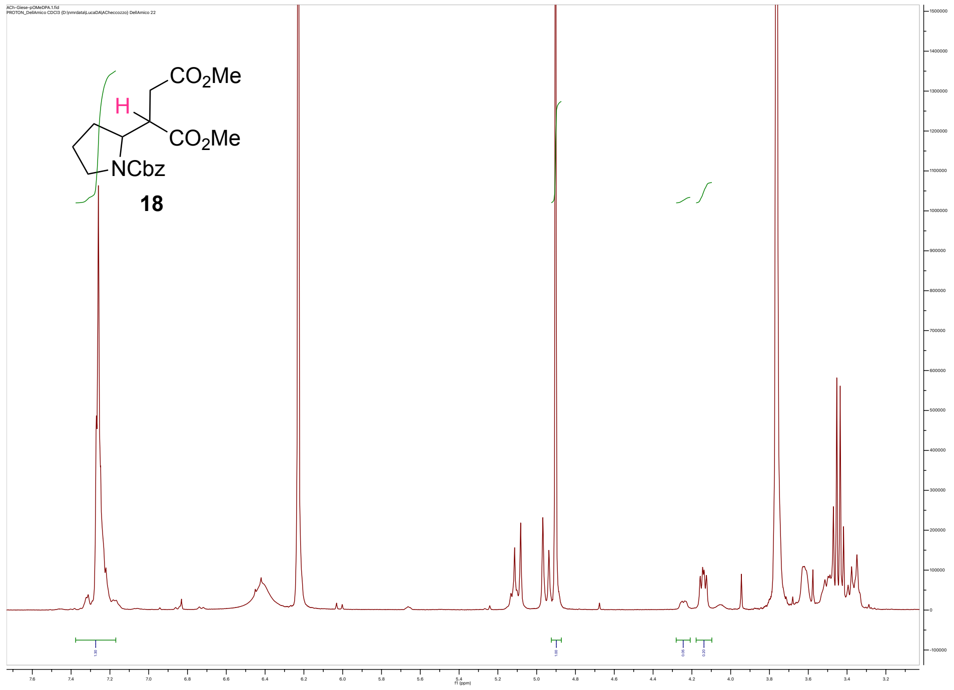

Figure 52. ^{1}*H-NMR (400 MHz,* $CDCl_3$*) reaction crude of the Giese-type photoreaction with* ***poly(OEGMA-co-3(OMeDPA)IPN-MA)*** *as PC and* CH_2Br_2 *as internal standard (4.9 ppm, 2H). The highlighted proton H is the diagnostic one used for the calculation of the NMR yield which correspond to the two peaks, the* ***broad signal at 4.15 ppm*** *and the* ***multiplet at 4.30*** *due to the formation of the rotamers.*

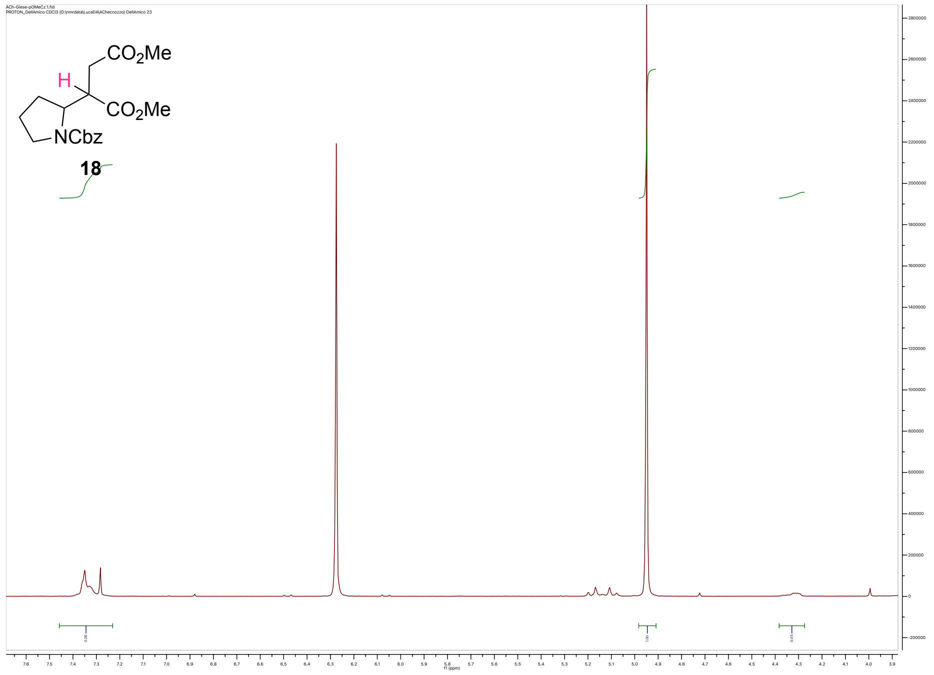

Figure 51. ^{1}*H-NMR (400 MHz,* $CDCl_3$*) reaction crude of the Giese-type photoreaction with* ***poly(OEGMA-co-3(OMeCz)IPN-MA)*** *as PC and* CH_2Br_2 *as internal standard (4.9 ppm, 2H). The highlighted proton H is the diagnostic one used for the calculation of the NMR yield which correspond to the two peaks, the* ***broad signal at 4.15 ppm*** *and the* ***multiplet at 4.30*** *due to the formation of the rotamers.*

5.8.2 Povarov-type cyclization

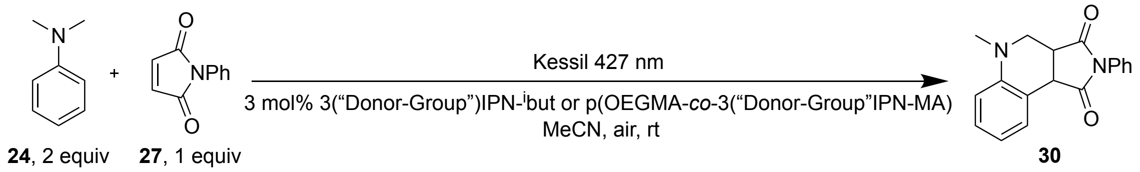

The procedure was followed according to literature[94]. *N*-phenylmaleimide **27** (17.3 mg, 1 equiv, 0.10 mmol) and the selected photocatalyst (3.0 mol% catalyst loading) was dissolved in dry MeCN (1.2 mL). To the resulting solution, *N,N*-dimethylaniline **24** (25 µL, 2 equiv, 0.2 mmol) was added dropwise under vigorous stirring at room temperature. The solution (0.083 M) was stirred at room temperature and irradiated using the Kessil lamp. The polymeric system was precipitate with diethyl ether. The product **30** was detected by ^{1}H-NMR from the reaction crude and the yield was calculated using CH_2Br_2 as internal standard (3.5 µL, 0.05 mmol).

Figure 53. Photochemical setup for the Povarov-type cyclization. The distance between the vial and the Kessil lamp is 3 cm. The system is ventilated with a fan.

1H-NMR spectra

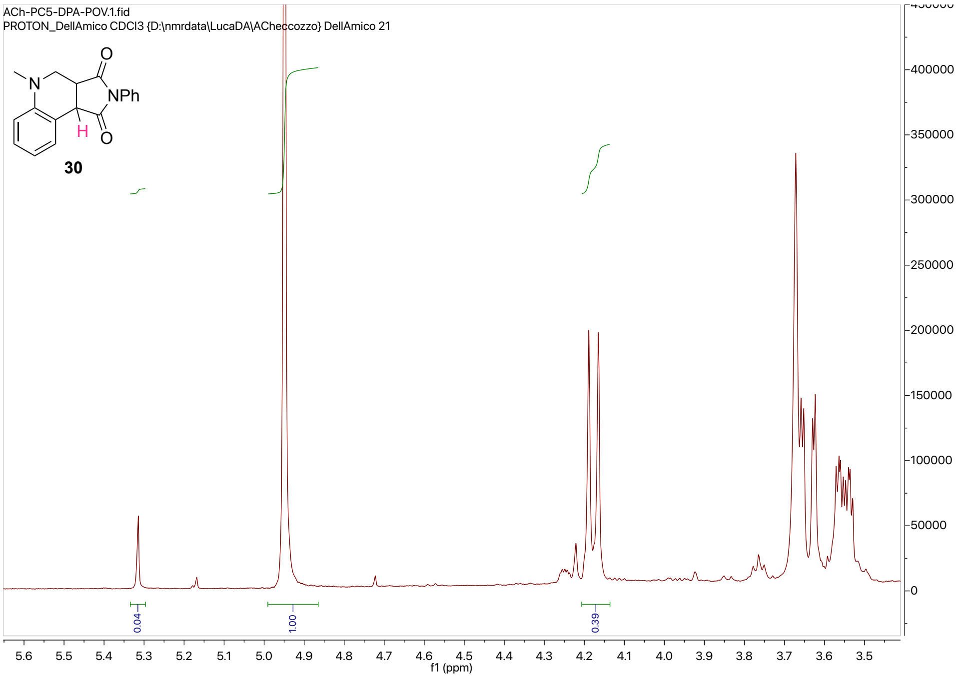

Figure 54. ^{1}H-NMR (400 MHz, $CDCl_3$) reaction crude of the Povarov-type photoreaction after 4 h irradiation with a 427 nm Kessil lamp with ***3DPAIPN-^{i}but*** *as PC and CH_2Br_2 as internal standard (4.9 ppm, 2H). The highlighted proton H is the diagnostic one used for the calculation of the NMR yield which correspond to the* ***doublet at 4.18 ppm****.*

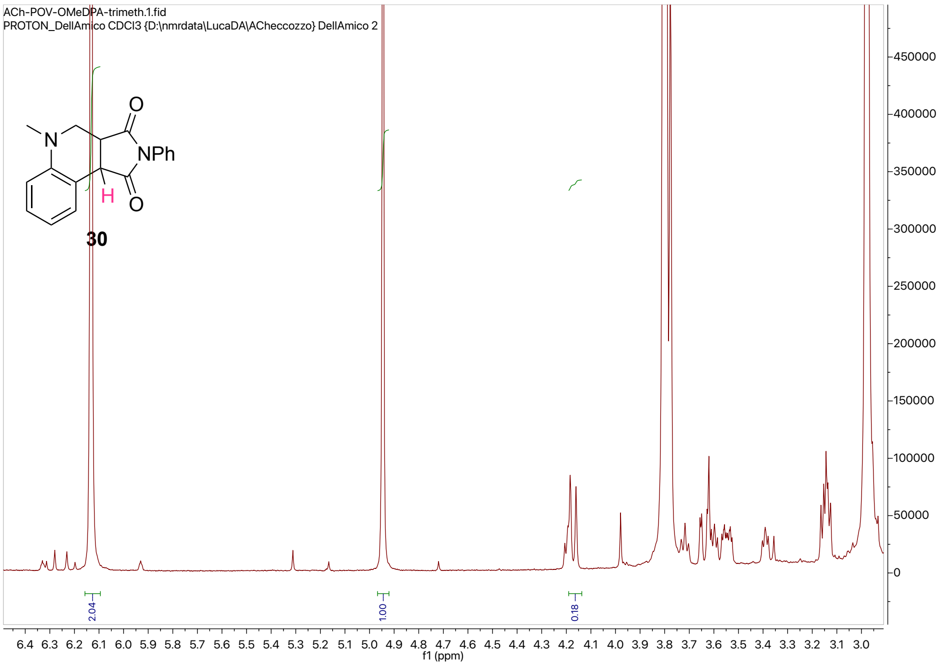

Figure 55. ^{1}H-NMR (400 MHz, $CDCl_3$) reaction crude of the Povarov-type photoreaction after 4 h irradiation with a 427 nm Kessil lamp with ***3(OMeDPA)IPN-^{i}but*** *as PC and CH_2Br_2 as internal standard (4.9 ppm, 2H). The highlighted proton H is the diagnostic one used for the calculation of the NMR yield which correspond to the* ***doublet at 4.18 ppm****.*

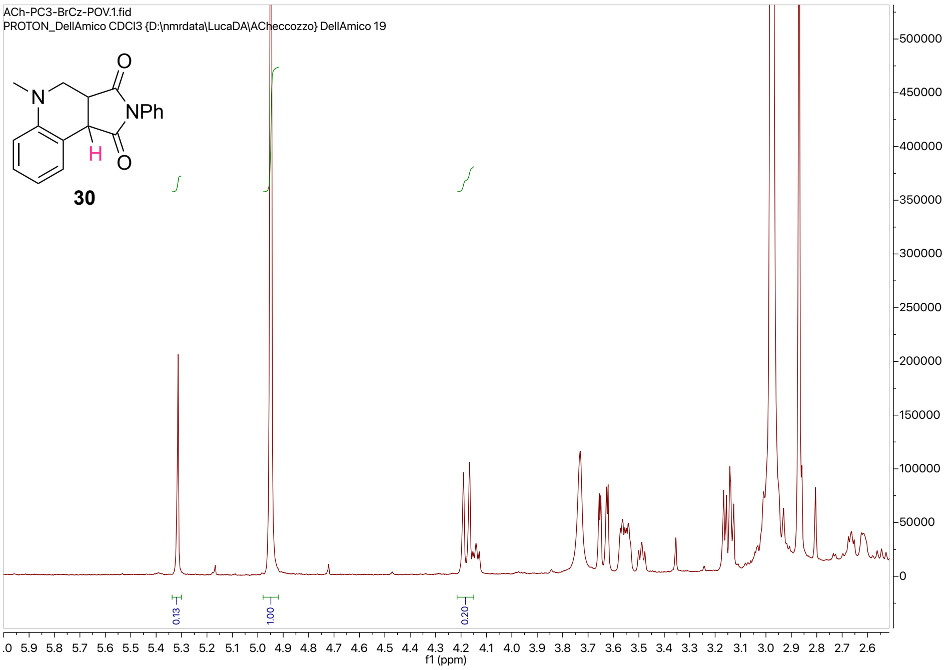

Figure 56. ^{1}H-NMR (400 MHz, $CDCl_3$) reaction crude of the Povarov-type photoreaction after 4 h irradiation with a 427 nm Kessil lamp with **3(BrCz)IPN-^{i}**but as PC and CH_2Br_2 as internal standard (4.9 ppm, 2H). The highlighted proton H is the diagnostic one used for the calculation of the NMR yield which correspond to the **doublet at 4.18 ppm**.

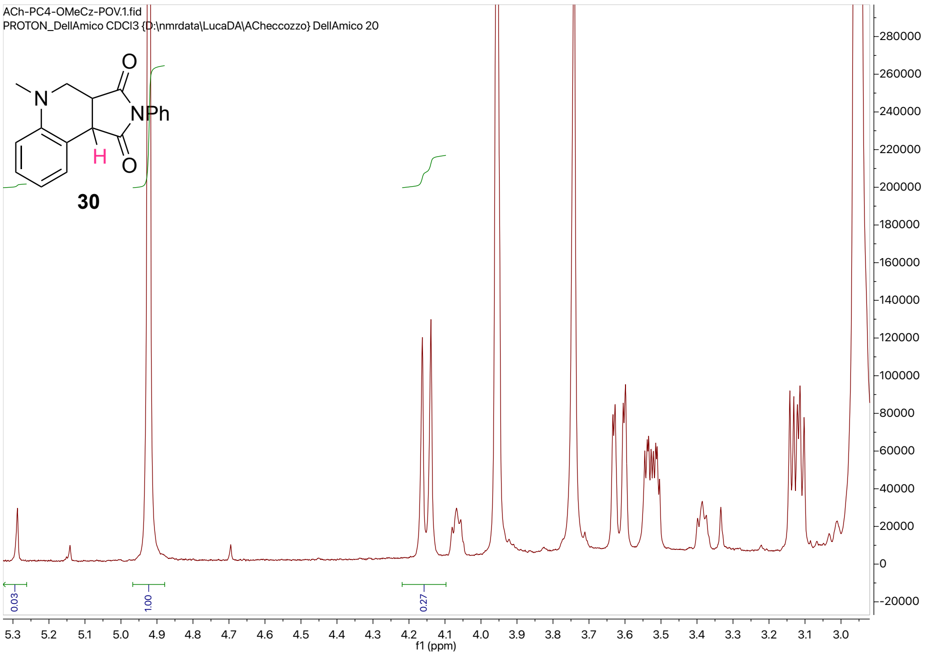

Figure 57. ^{1}H-NMR (400 MHz, $CDCl_3$) reaction crude of the Povarov-type photoreaction after 4 h irradiation with a 427 nm Kessil lamp with **3(OMeCz)IPN-^{i}but** as PC and CH_2Br_2 as internal standard (4.9 ppm, 2H). The highlighted proton H is the diagnostic one used for the calculation of the NMR yield which correspond to the **doublet at 4.18 ppm**.

5.8.3 Dehalogenation of benzylhalide

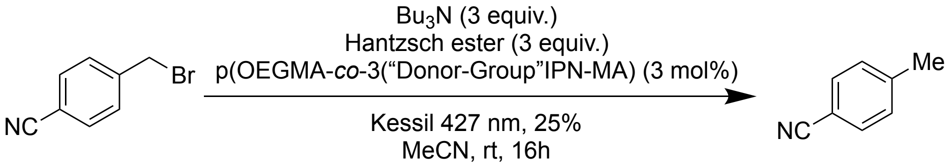

31, 1 equiv

32

The procedure was followed according to literature[94]. An oven-dried 10 mL Schlenk with a glass cap and a magnetic stir bar was charged with 4-(Bromomethyl)benzonitrile **31** (19.6 mg, 0.10 mmol, 1.0 equiv), MeCN (1.0 mL), tributylamine (70 μL,0.30 mmol, 3.0 equiv), Hantzsch ester (75.9 mg, 0.30 mmol, 3.0 equiv) and the selected photocatalyst (0.003 mmol, 3.0 mol% cat. loading). The reaction mixture was degassed by using the freeze-pump-thaw technique, cycles (3×), then irradiated with the Kessil lamp for 16h. The polymeric system was precipitate with diethyl ether. The product **32** was detected by ^{1}H-NMR from the reaction crude and the yield was calculated using CH_2Br_2 as internal standard (3.5 μL, 0.05 mmol).

1H-NMR spectra

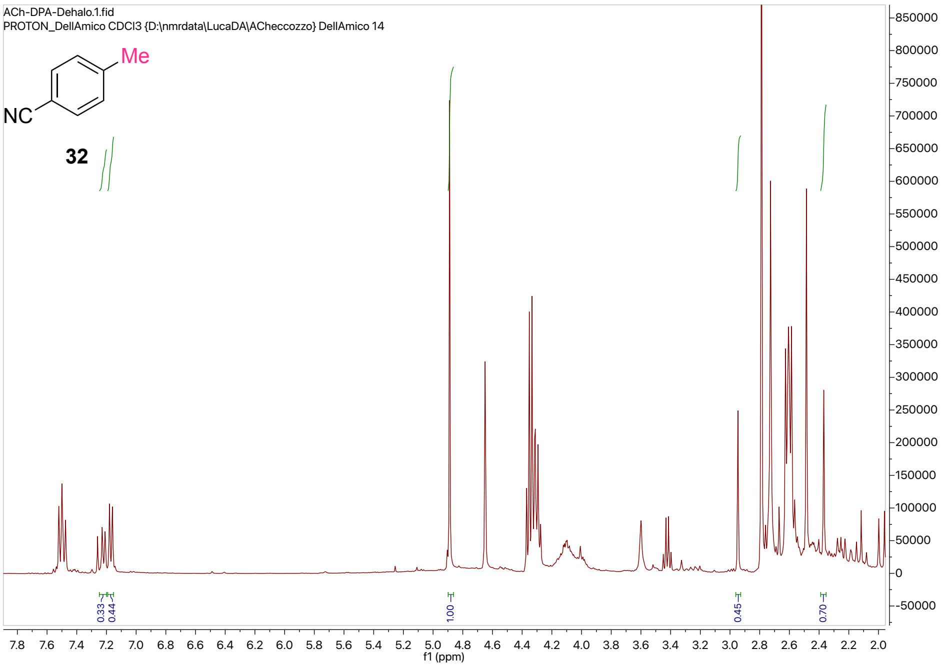

*Figure 58. ^{1}H-NMR (400 MHz, CDCl$_3$) reaction crude of the dehalogenation of benzyl halide photoreaction with **poly(OEGMA-co-3DPAIPN-MA)** as PC and CH$_2$Br$_2$ as internal standard (4.9 ppm, 2H). The highlighted protons Me are the diagnostic one used for the calculation of the NMR yield which correspond to the **singlet at 2.4 ppm**. The singlet at 2.9 ppm is probably relatives the two -CH$_2$- of the dimer (4H). The integration of the **multiplet at 7.18 ppm** is in line with one of the couples of the aromatic protons (2H) of the product while the multiplet at 7.21 ppm is consistent with the dimer.*

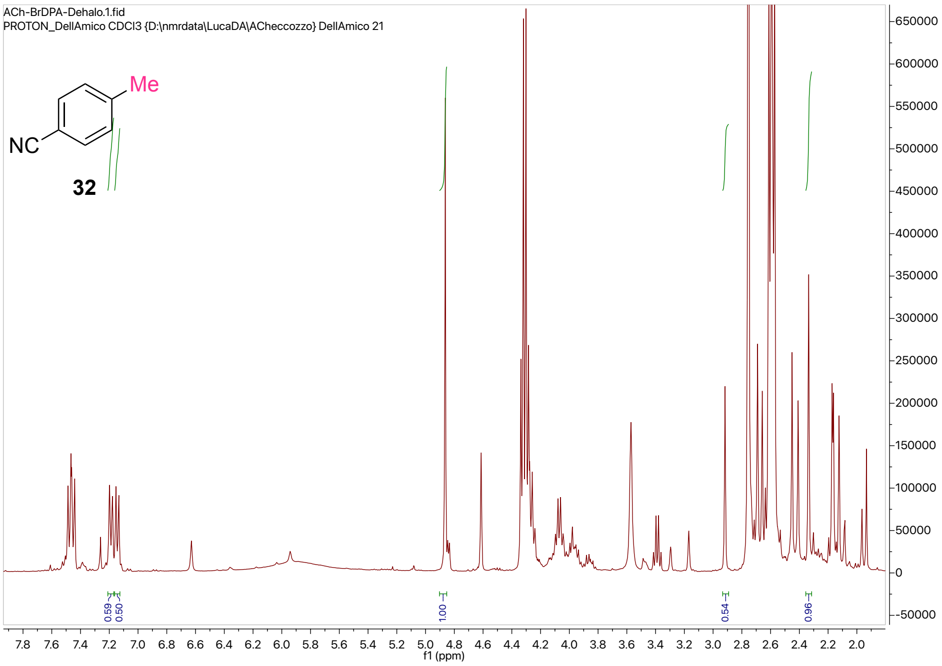

*Figure 59. ^{1}H-NMR (400 MHz, CDCl$_3$) reaction crude of the dehalogenation of benzyl halide photoreaction with **poly(OEGMA-co-3(BrDPA)IPN-MA)** as PC and CH$_2$Br$_2$ as internal standard (4.9 ppm, 2H). The highlighted protons Me are the diagnostic one used for the calculation of the NMR yield which correspond to the **singlet at 2.4 ppm**. The singlet at 2.9 ppm is probably relatives the two -CH$_2$- of the dimer (4H). The integration of the **multiplet at 7.18 ppm** is in line with one of the couples of the aromatic protons (2H) of the product while the multiplet at 7.2 ppm is consistent with the dimer.*

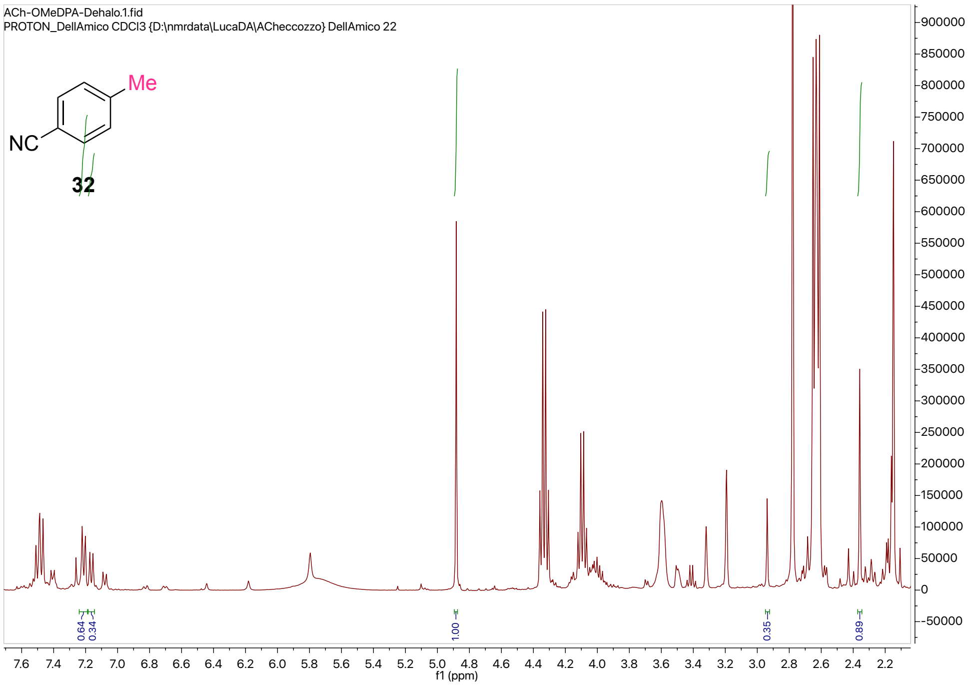

*Figure 60. ^{1}H-NMR (400 MHz, $CDCl_3$) reaction crude of the dehalogenation of benzyl halide photoreaction with **poly(OEGMA-co-3(OMeDPA)IPN-MA)** as PC and CH_2Br_2 as internal standard (4.9 ppm, 2H). The highlighted protons Me are the diagnostic one used for the calculation of the NMR yield which correspond to the **singlet at 2.4 ppm**. The singlet at 2.9 ppm is probably relatives the two -CH_2- of the dimer (4H). The integration of the **multiplet at 7.18 ppm** is in line with one of the couples of the aromatic protons (2H) of the product while the multiplet at 7.2 ppm is consistent with the dimer.*

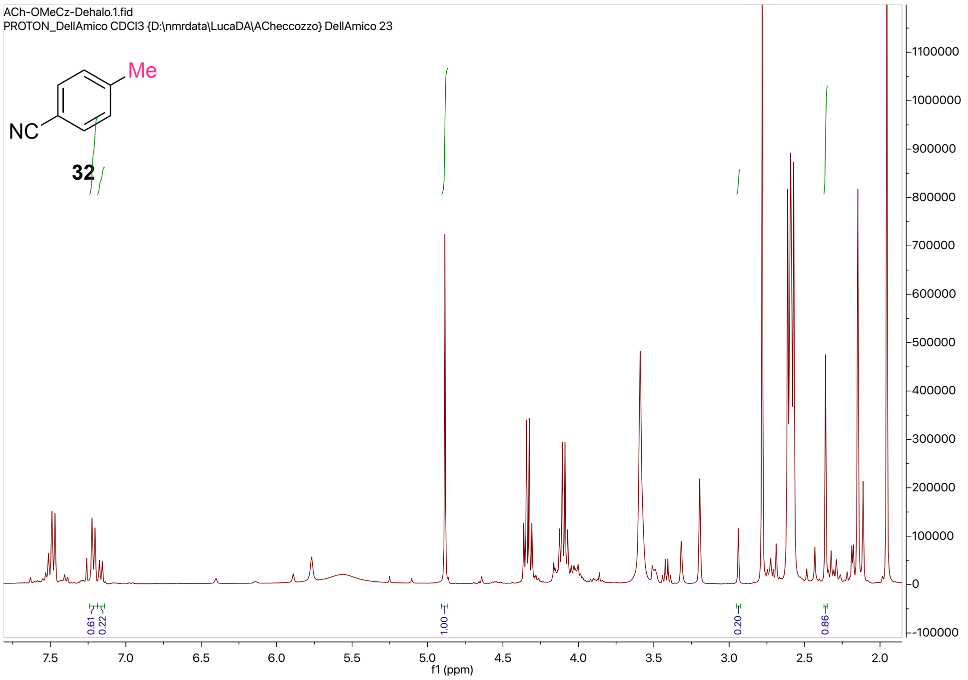

*Figure 61. ^{1}H-NMR (400 MHz, $CDCl_3$) reaction crude of the dehalogenation of benzyl halide photoreaction with **poly(OEGMA-co-3(OMeCz)IPN-MA)** as PC and CH_2Br_2 as internal standard (4.9 ppm, 2H). The highlighted protons Me are the diagnostic one used for the calculation of the NMR yield which correspond to the **singlet at 2.4 ppm.** The singlet at 2.9 ppm is probably relatives the two -CH_2- of the dimer (4H). The integration of the **multiplet at 7.18 ppm** is in line with one of the couples of the aromatic protons (2H) of the product while the multiplet at 7.2 ppm is consistent with the dimer.*

6. NMR spectra

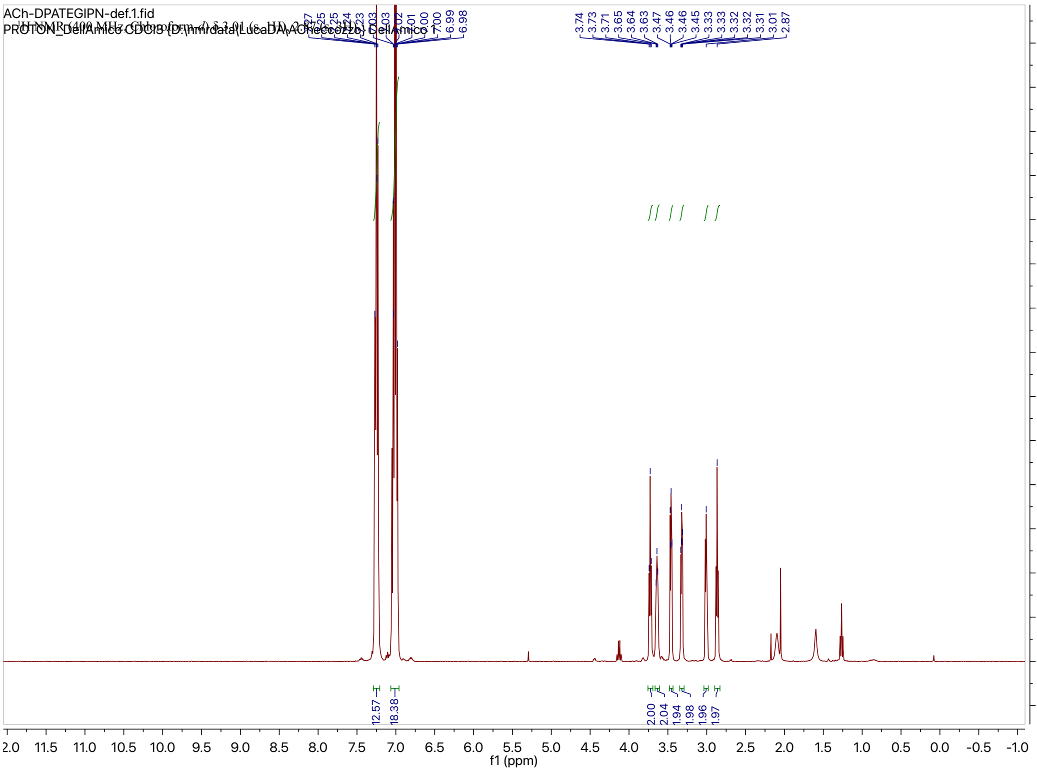

Figure 62. ^{1}H-NMR of 3DPATEGIPN ($CDCl_3$).

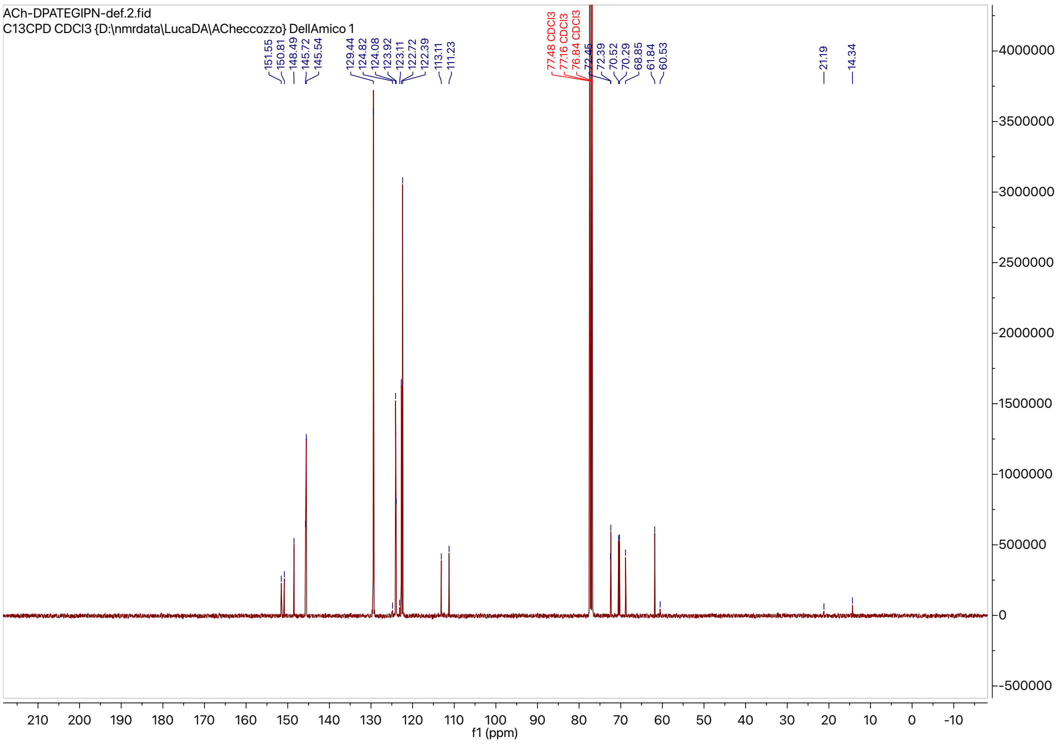

Figure 63. ^{13}C-NMR of 3DPATEGIPN ($CDCl_3$).

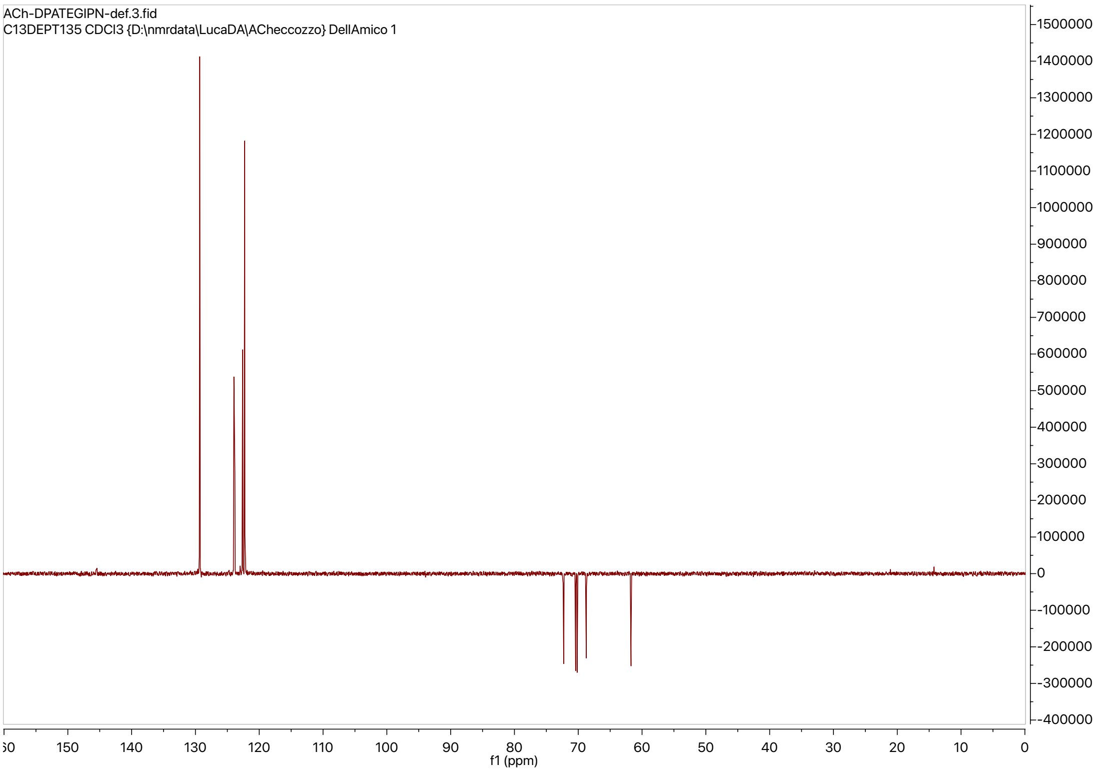

Figure 64. ^{13}C-NMR DEPT-135 of 3DPATEGIPN ($CDCl_3$).

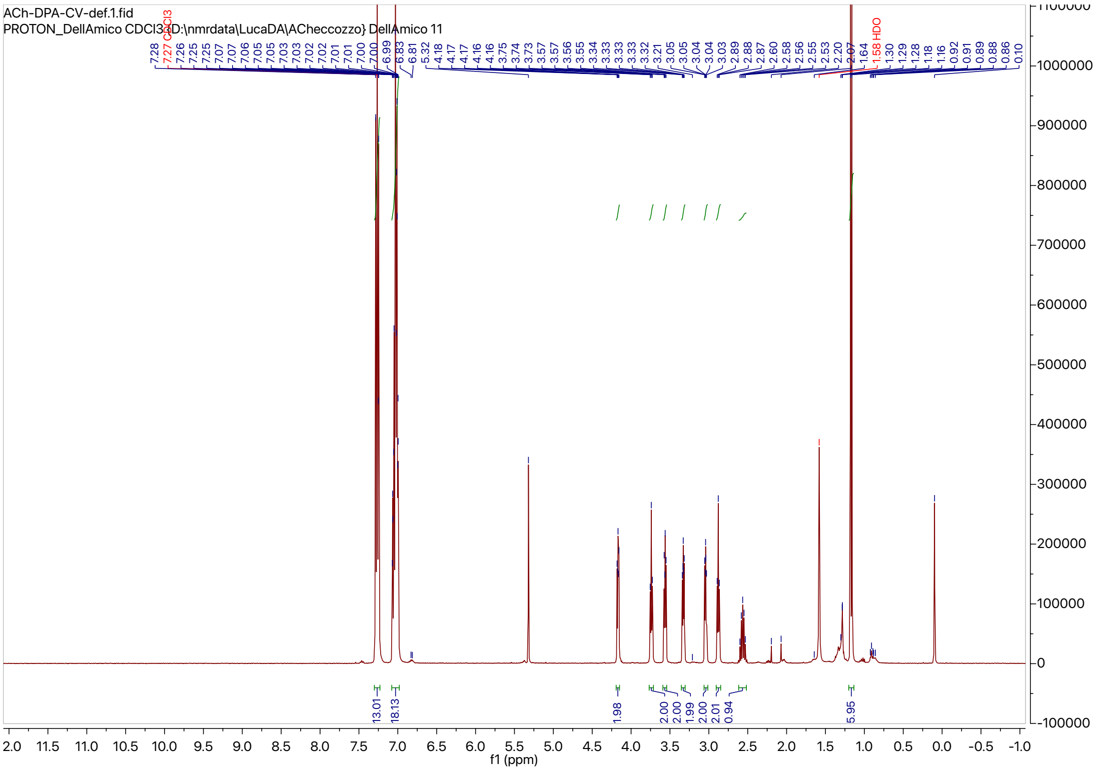

Figure 65. ^{1}H-NMR of 3DPAIPN-^{i}but ($CDCl_3$).

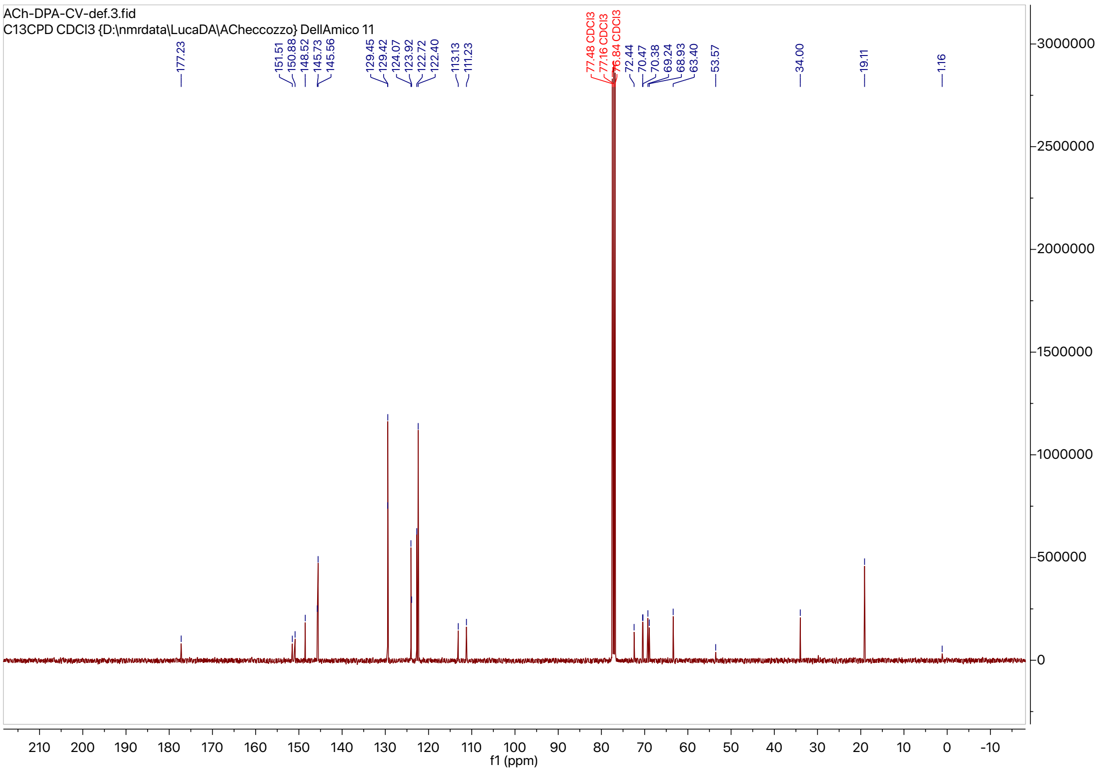

Figure 66. ^{13}C-NMR of 3DPAIPN-^{i}but (CDCl$_3$).

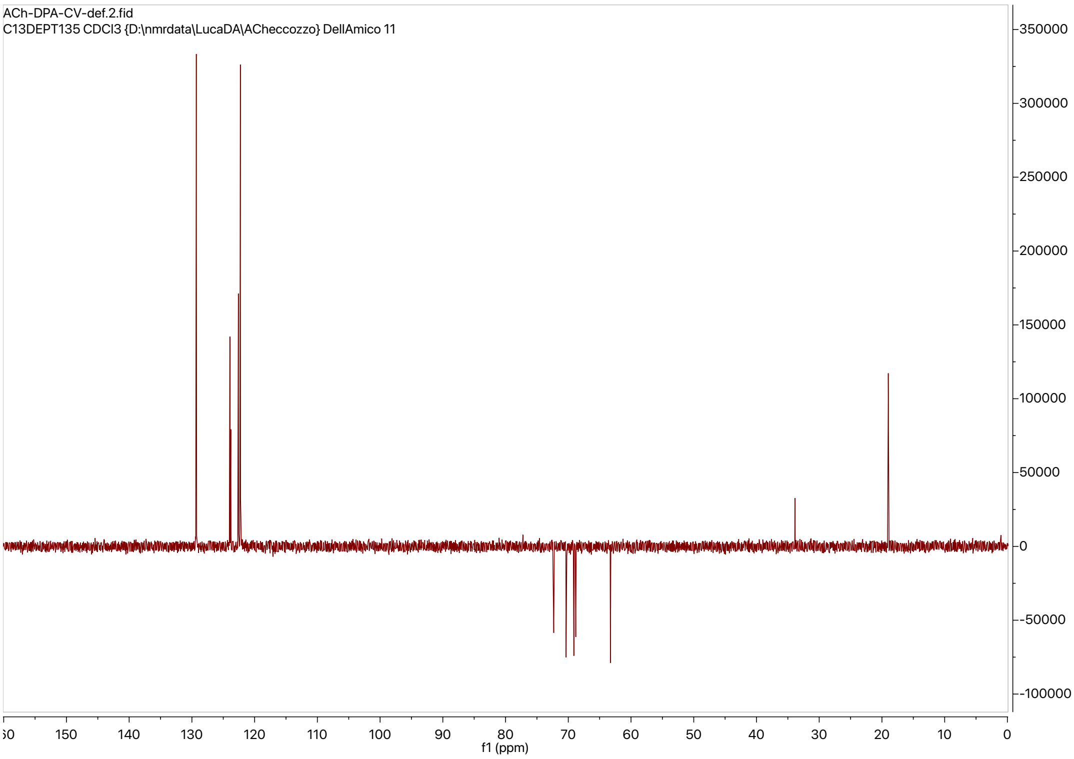

Figure 67. ^{13}C-NMR DEPT-135 of 3DPAIPN-^{i}but (CDCl$_3$).

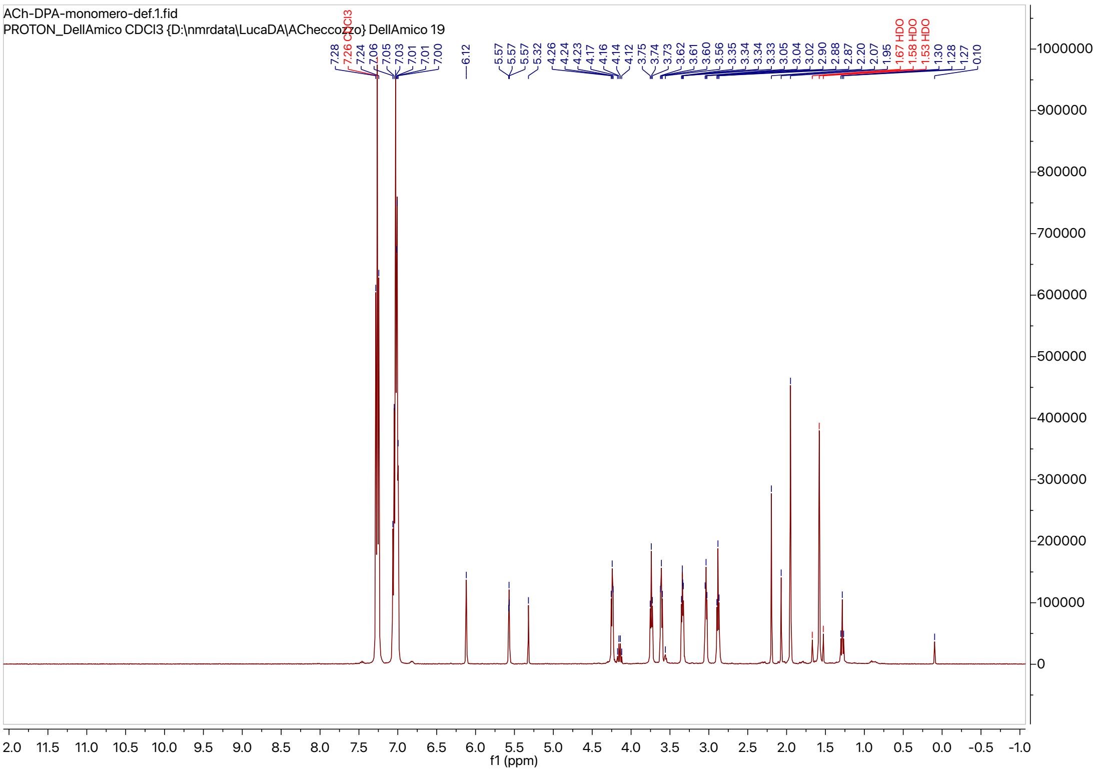

Figure 67. ^{1}H-NMR of 3DPAIPN-MA (CDCl$_3$).

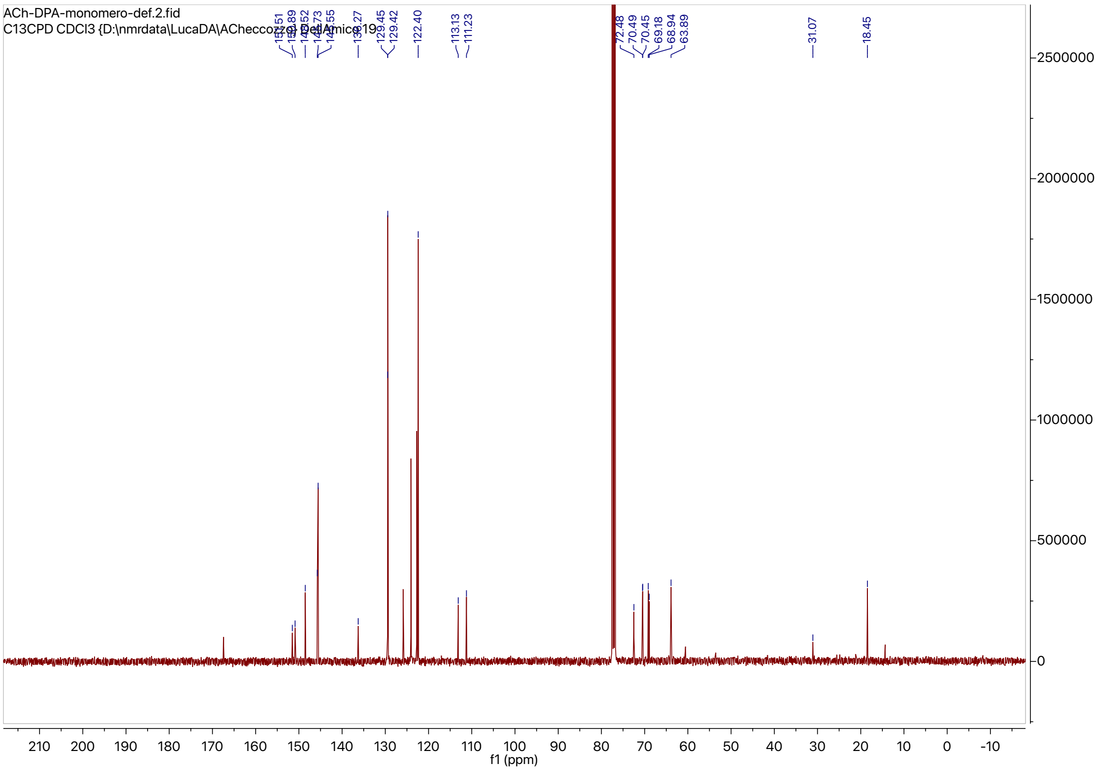

Figure 68. ^{13}C-NMR of 3DPAIPN-MA (CDCl$_3$).

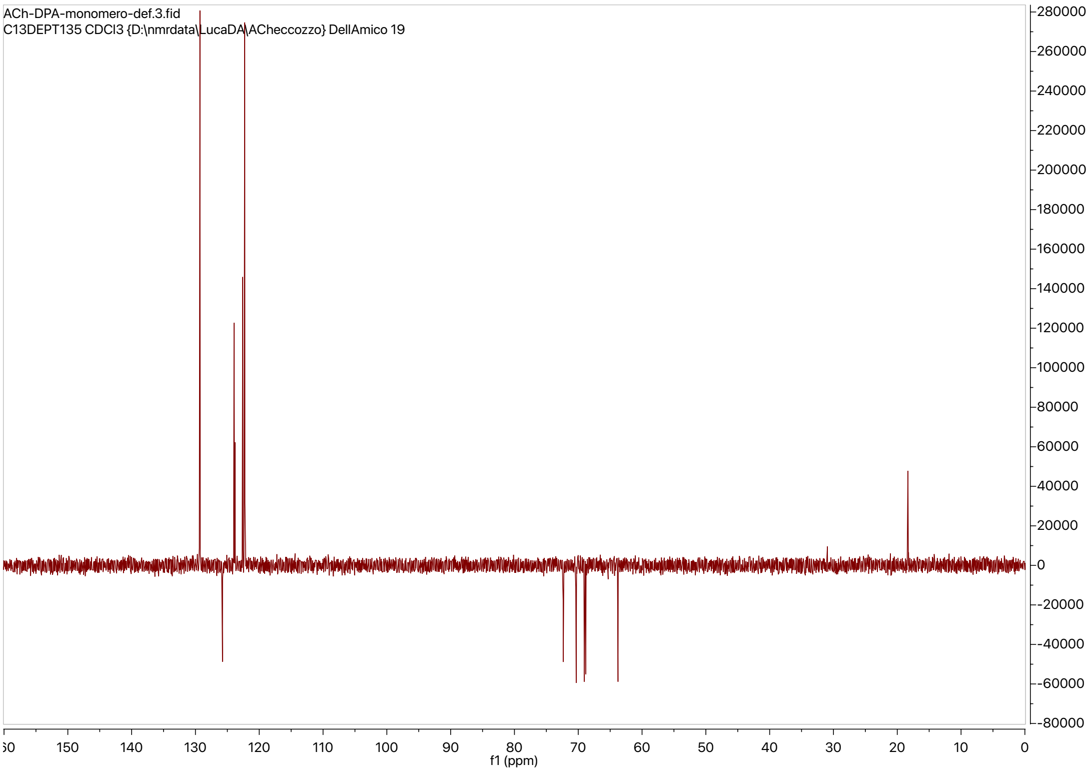

Figure 69. ^{13}C-NMR DEPT-135 of 3DPAIPN-MA (CDCl$_3$).

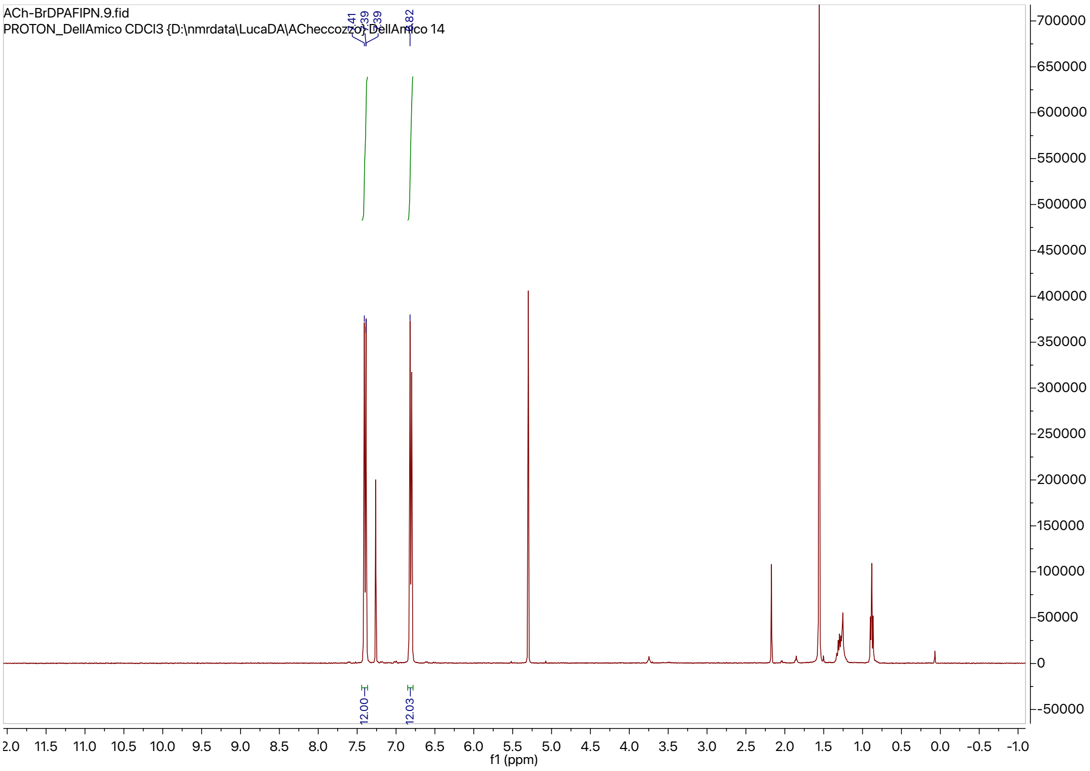

Figure 70. ^{1}H-NMR of 3(BrDPA)FIPN (CDCl$_3$).

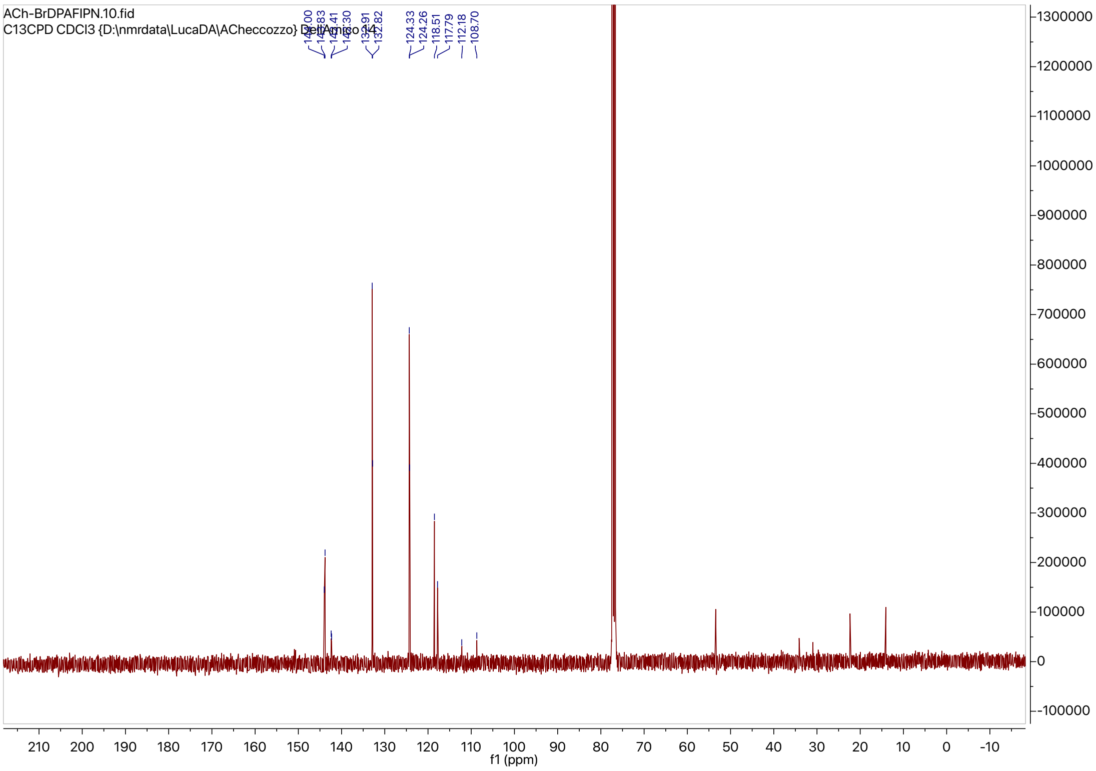

Figure 71. ^{13}C-NMR of 3(BrDPA)FIPN ($CDCl_3$).

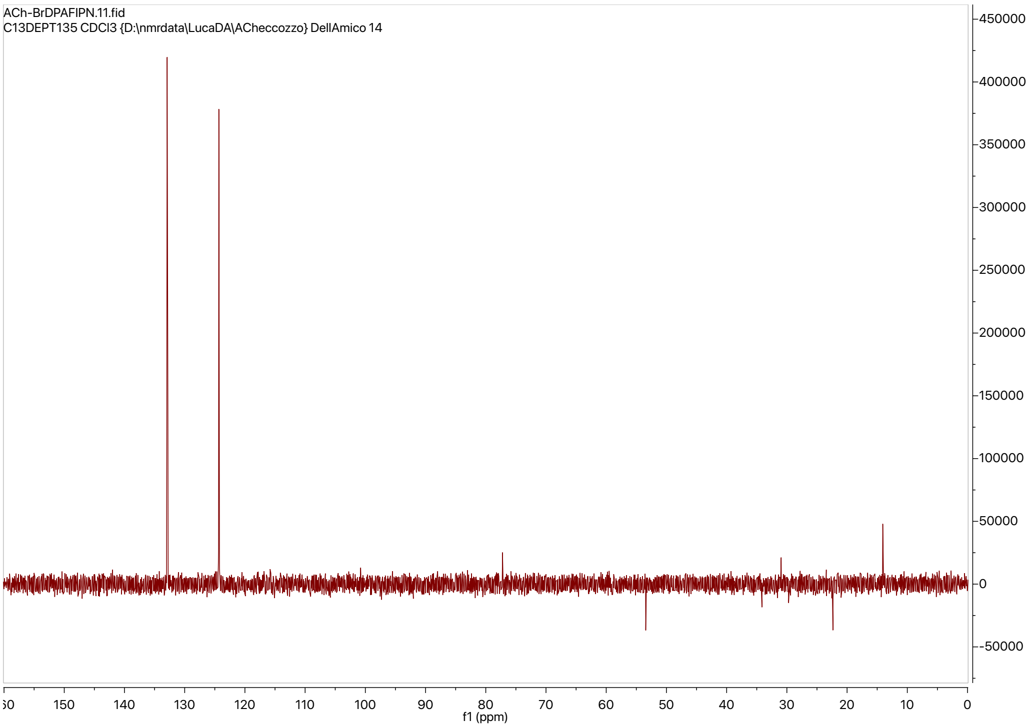

Figure 72. ^{13}C-NMR DEPT-135 of 3(BrDPA)FIPN ($CDCl_3$).

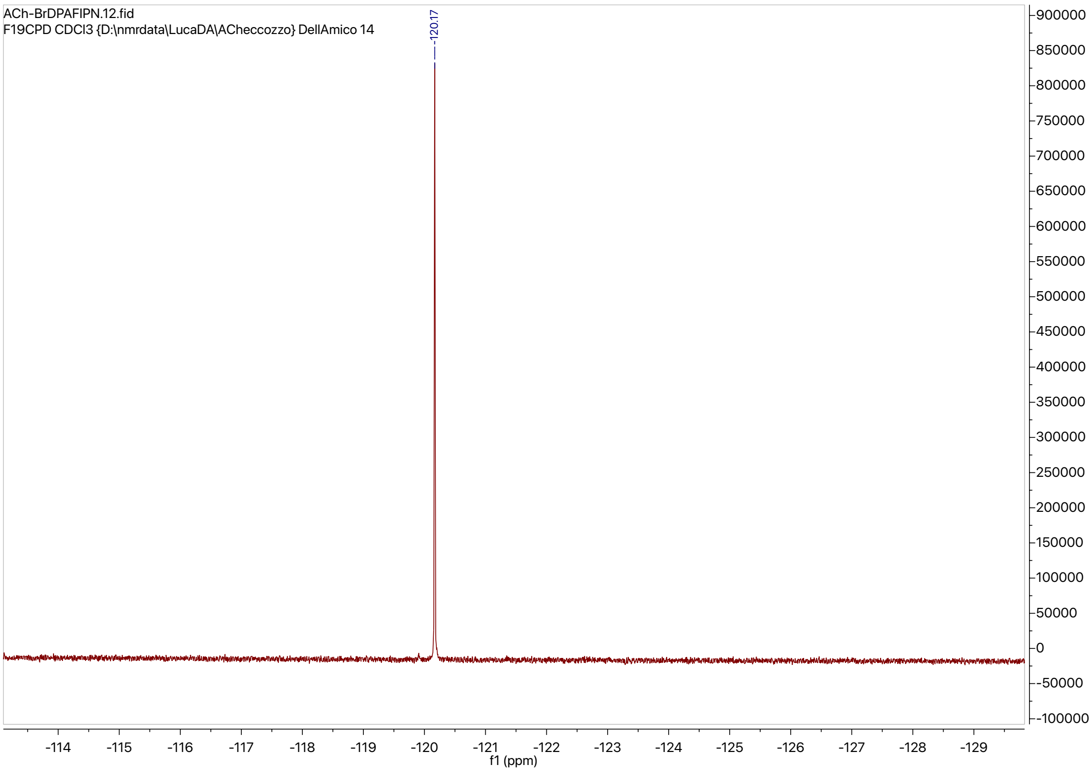

Figure 73. ^{19}F-NMR of 3(BrDPA)FIPN (CDCl$_3$).

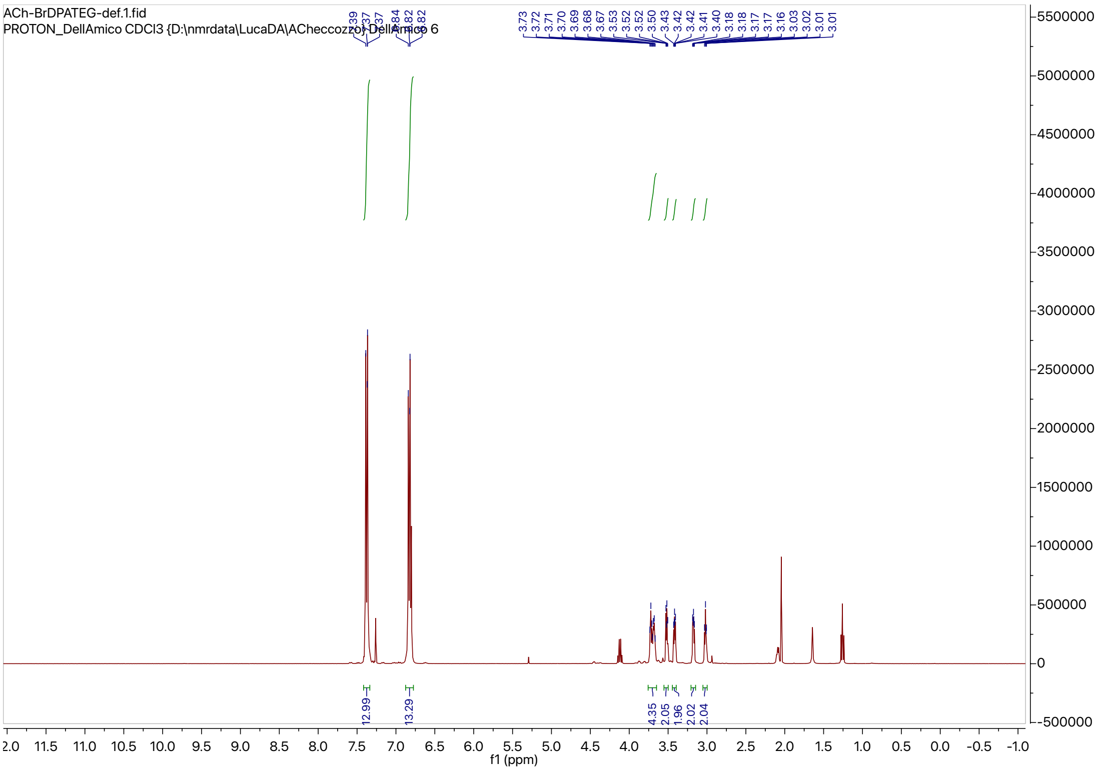

Figure 74. ^{1}H-NMR of 3(BrDPA)TEGIPN (CDCl$_3$).

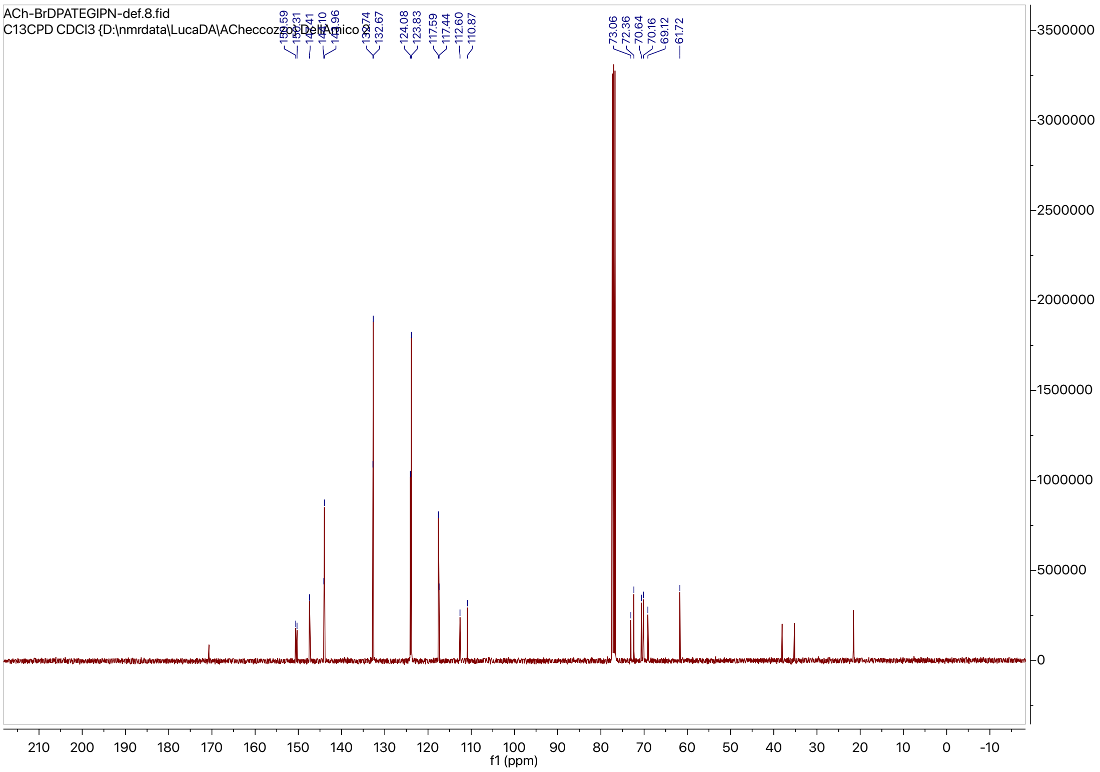

Figure 75. ^{13}C-NMR of 3(BrDPA)TEGIPN ($CDCl_3$).

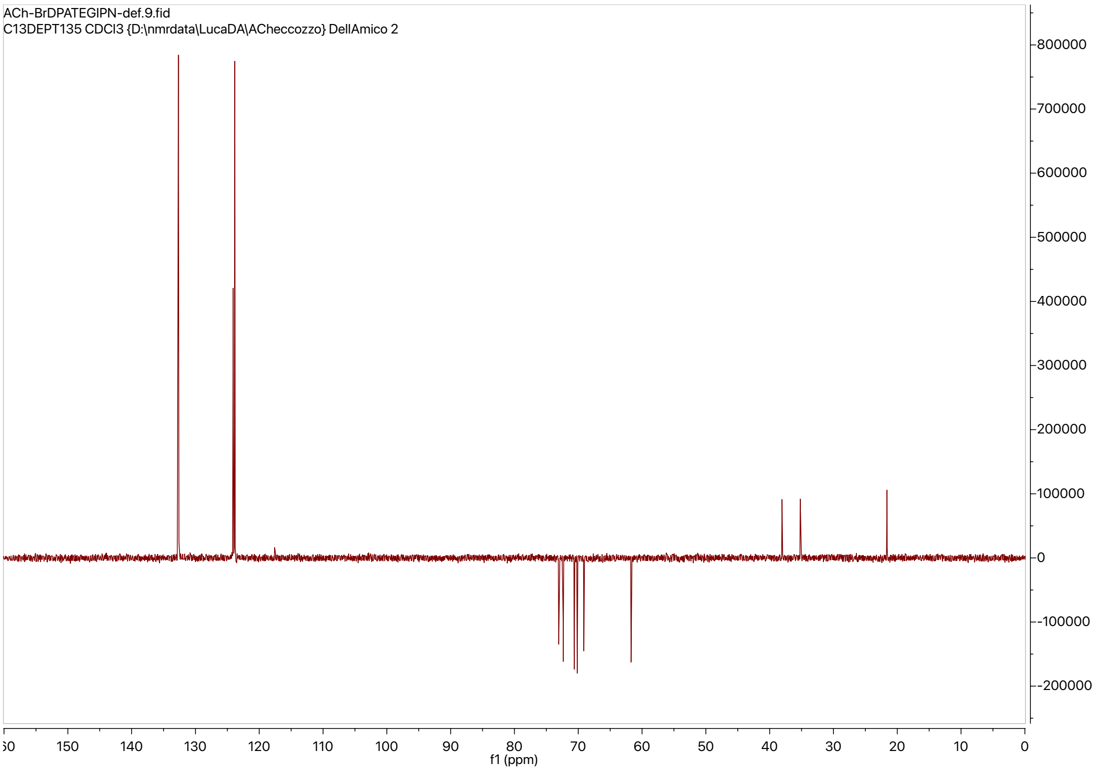

Figure 76. ^{13}C-NMR DEPT-135 of 3(BrDPA)TEGIPN ($CDCl_3$).

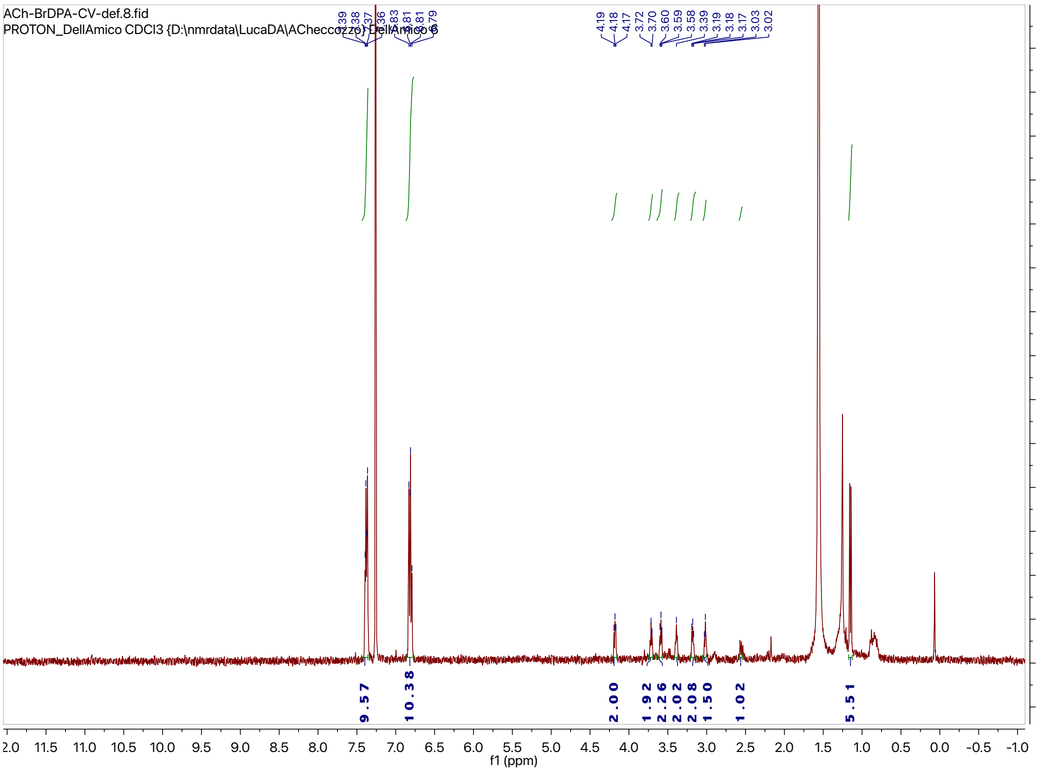

Figure 77. ^{1}H-NMR of 3(BrDPA)IPN-^{i}but (CDCl$_3$).

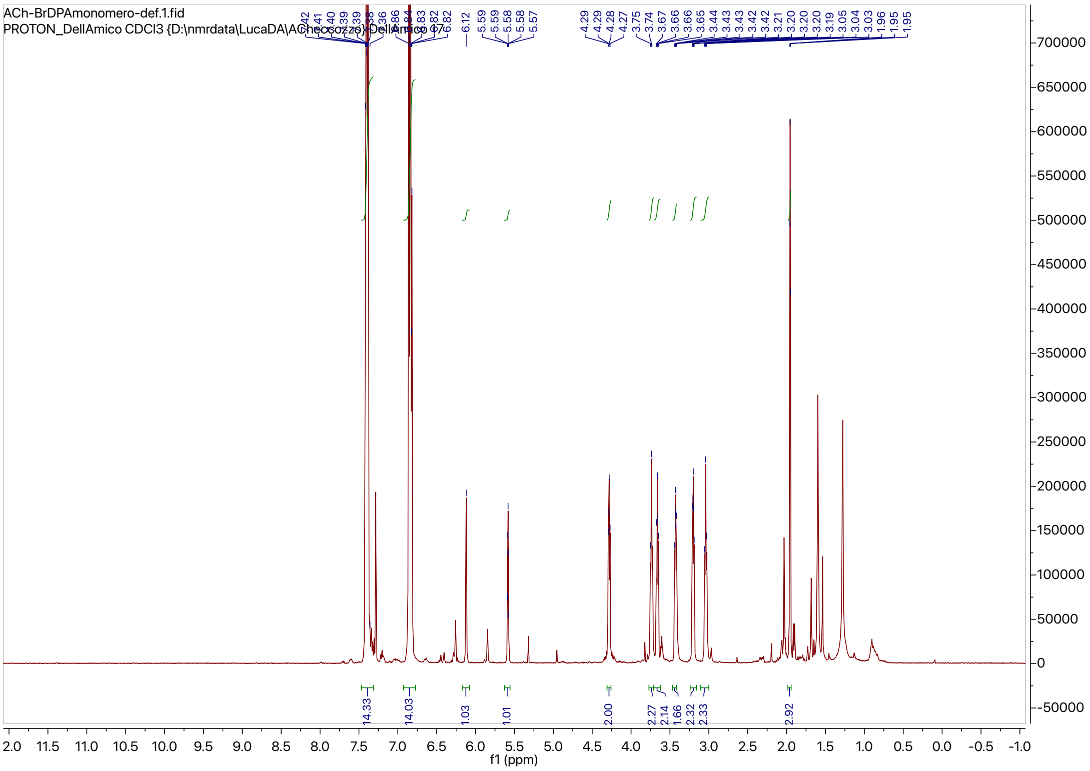

Figure 78. ^{1}H-NMR of 3(BrDPA)IPN-MA (CDCl$_3$).

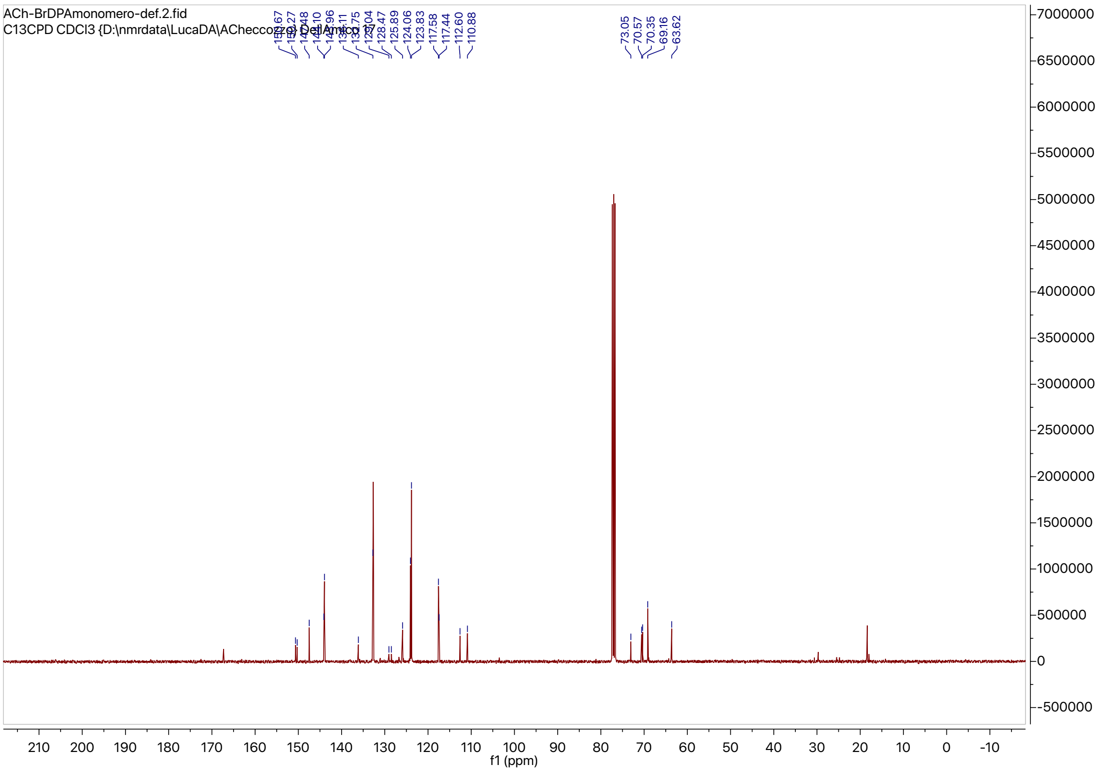

Figure 79. ^{13}C-NMR of 3(BrDPA)IPN-MA ($CDCl_3$).

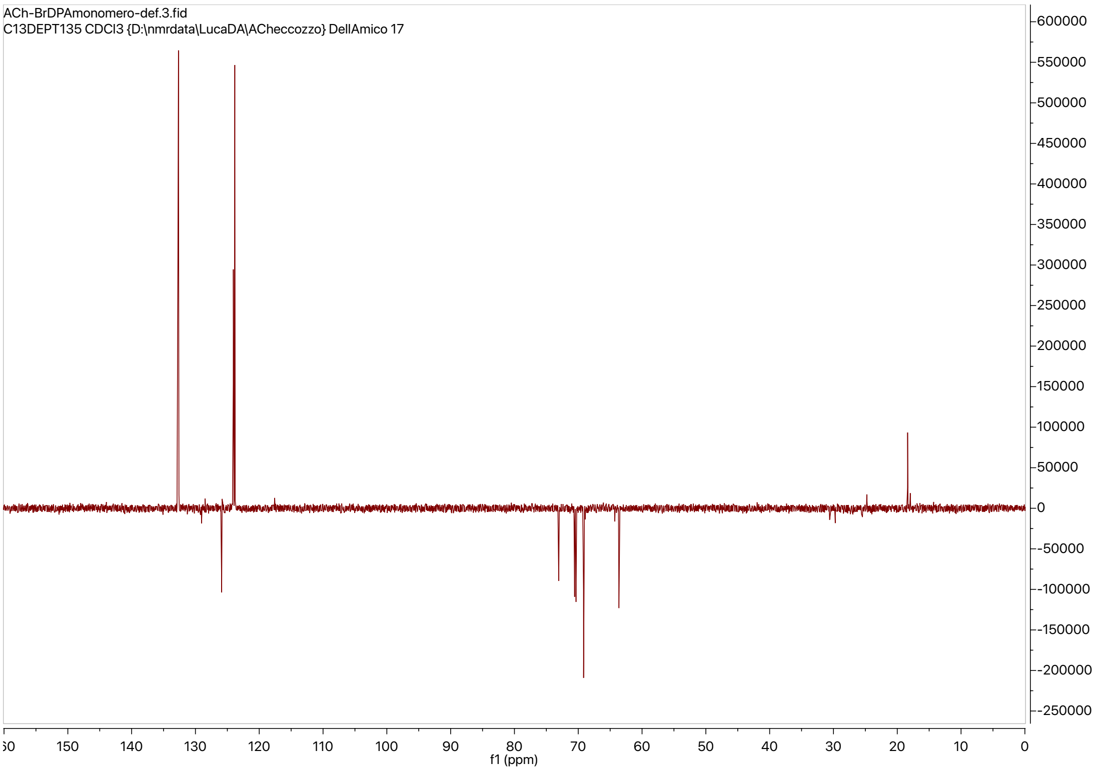

Figure 80. ^{13}C-NMR DEPT-135 of 3(BrDPA)IPN-MA ($CDCl_3$).

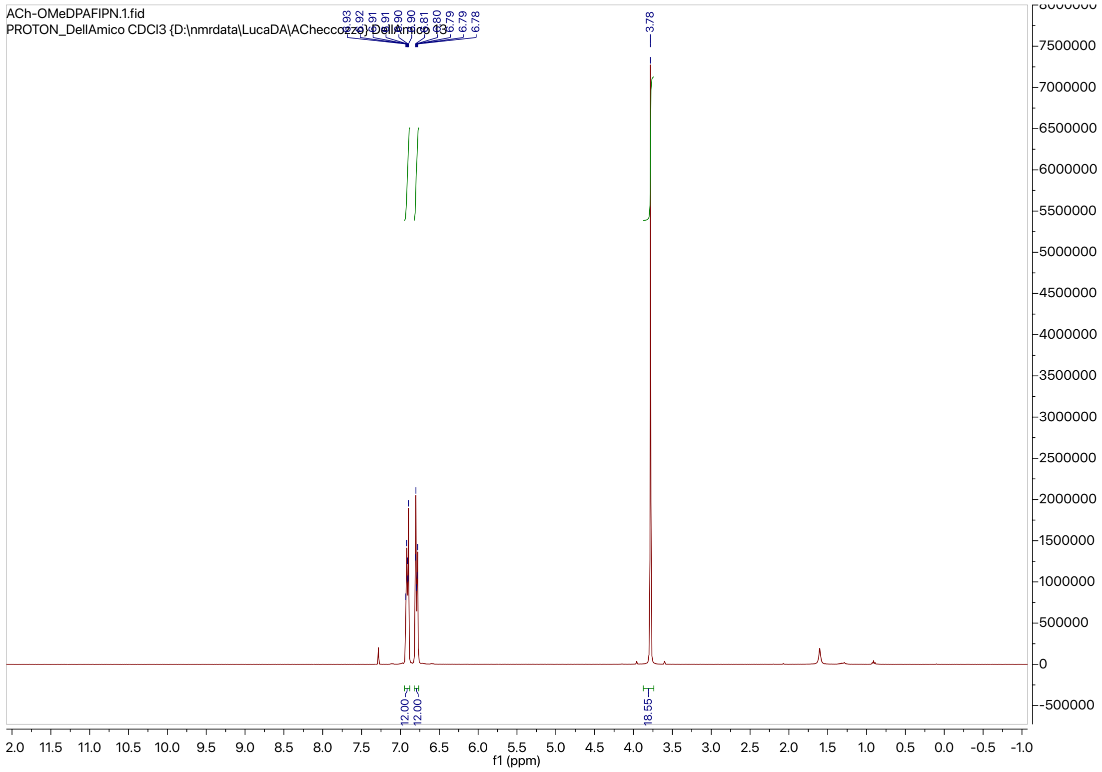

Figure 81. ^{1}H-NMR of 3(OMeDPA)FIPN ($CDCl_3$).

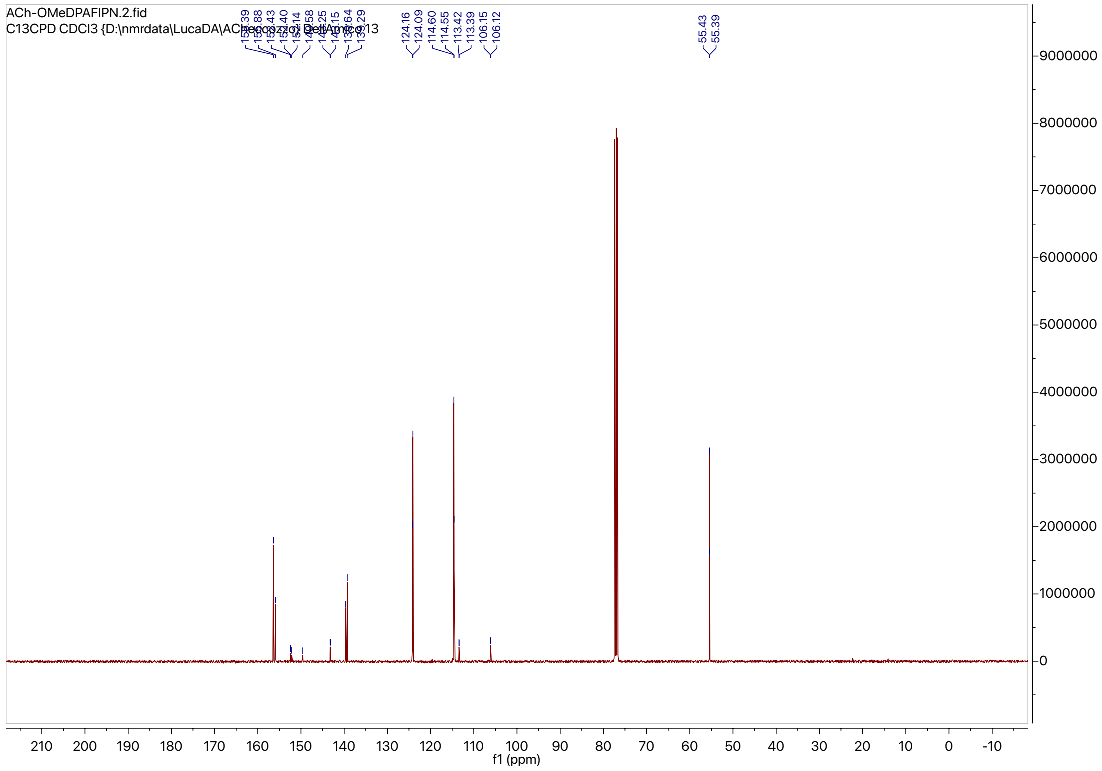

Figure 82. ^{13}C-NMR of 3(OMeDPA)FIPN ($CDCl_3$).

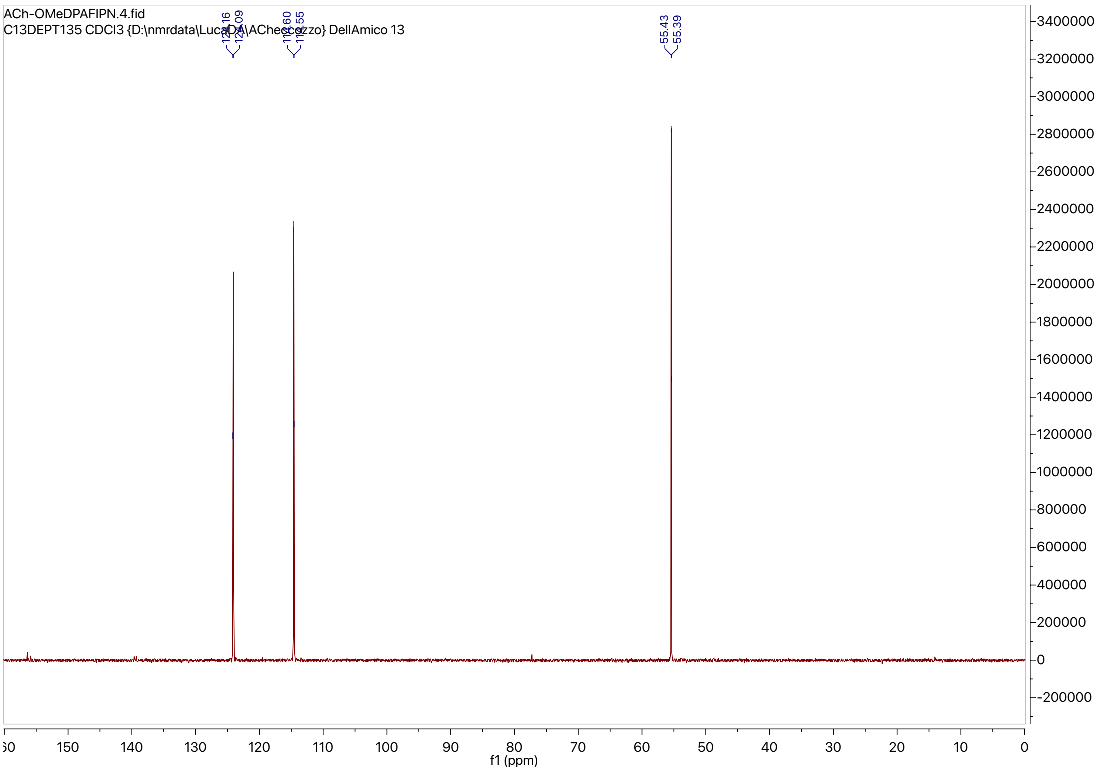

Figure 83. ^{13}C-NMR DEPT-135 of 3(OMeDPA)FIPN ($CDCl_3$).

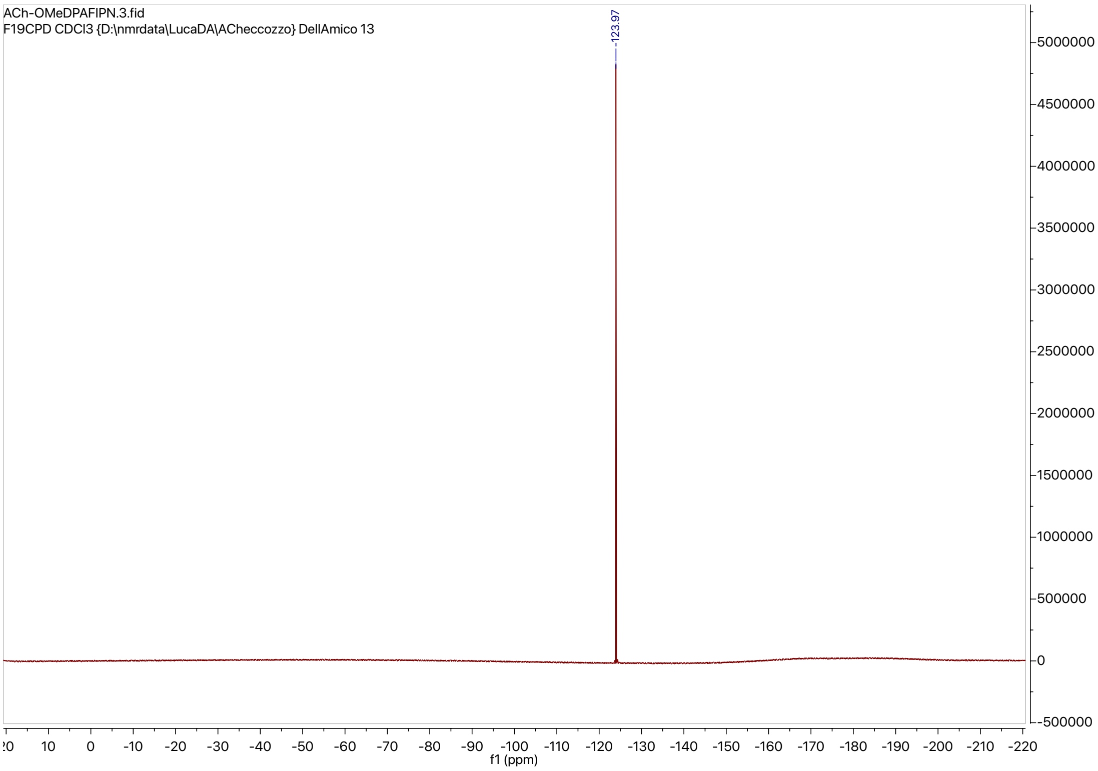

Figure 84. ^{19}F-NMR of 3(OMeDPA)FIPN ($CDCl_3$).

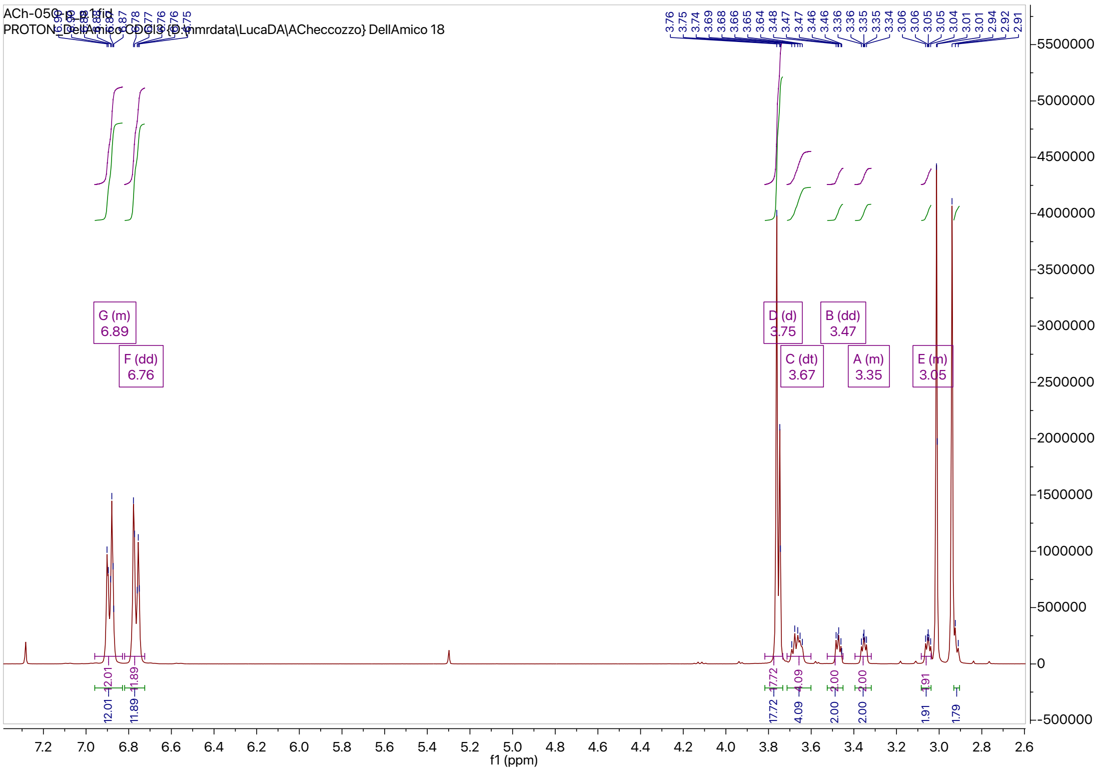

Figure 85. ^{1}H-NMR of 3(OMeDPA)TEGIPN (CDCl$_3$).

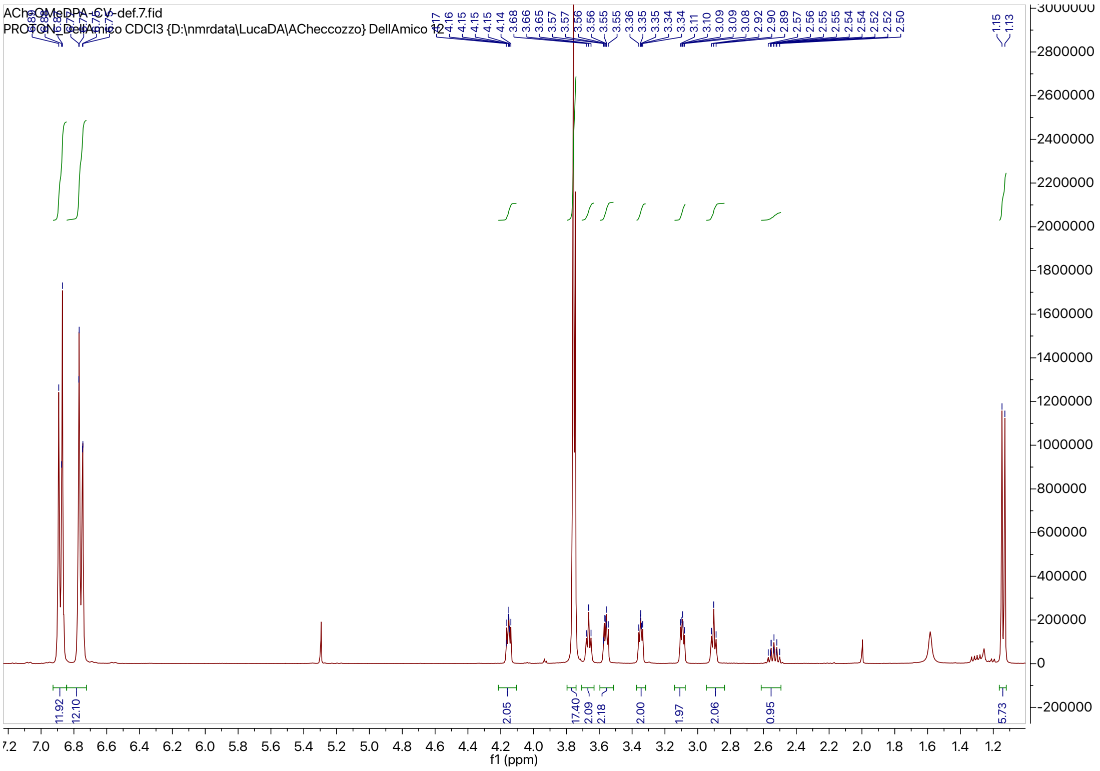

Figure 86. ^{1}H-NMR of 3(OMeDPA)IPN-^{i}but (CDCl$_3$).

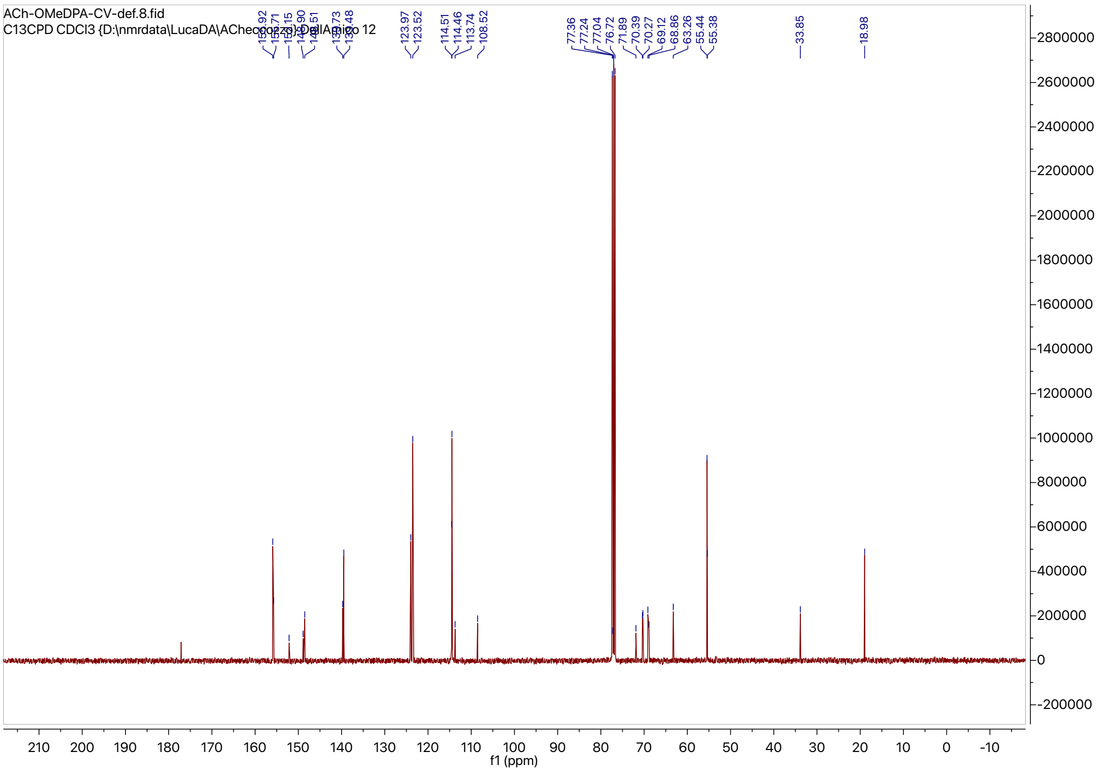

Figure 87. ^{13}C-NMR of 3(OMeDPA)IPN-^{i}but (CDCl$_3$).

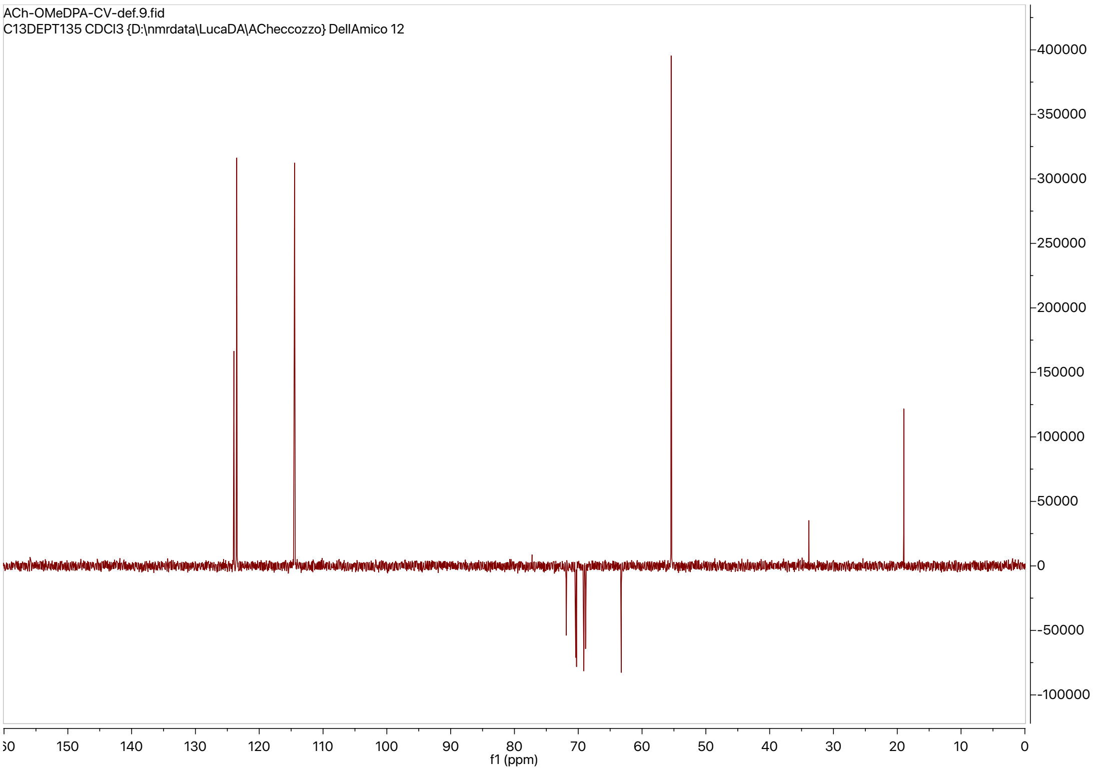

Figure 88. ^{13}C-NMR DEPT-135 of 3(OMeDPA)IPN-^{i}but (CDCl$_3$).

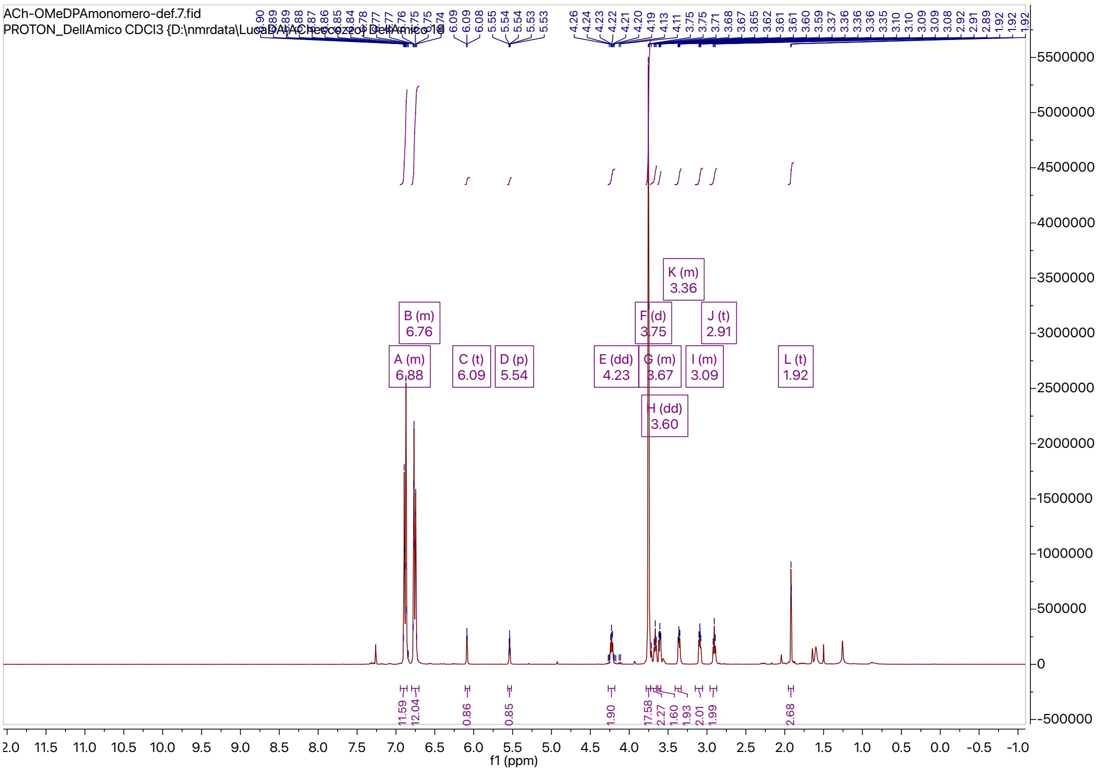

Figure 89. ^{1}H-NMR of 3(OMeDPA)IPN-MA (CDCl$_3$).

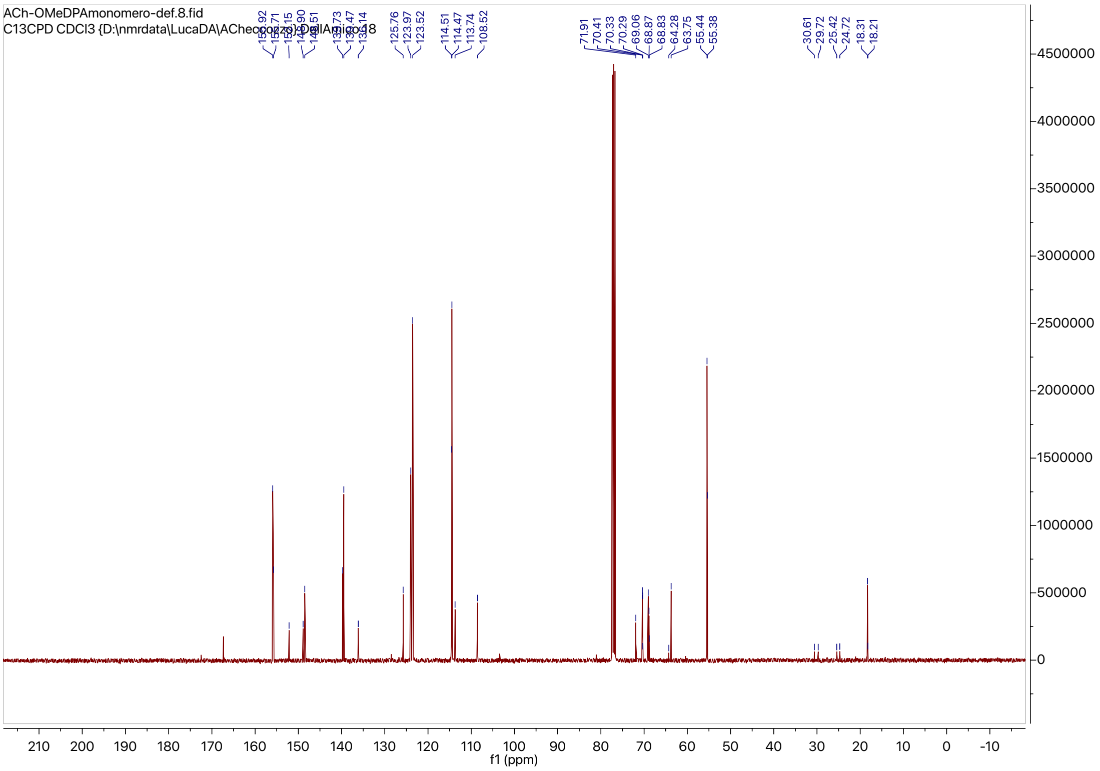

Figure 90. ^{13}C-NMR of 3(OMeDPA)IPN-MA (CDCl$_3$).

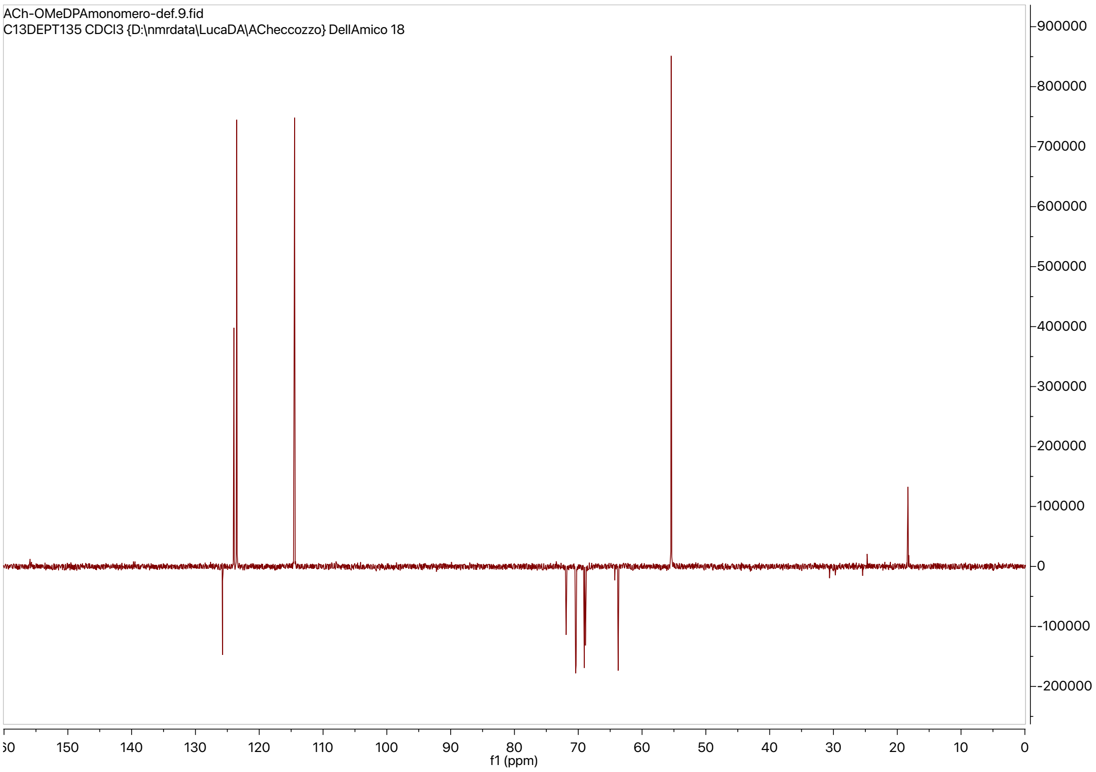

Figure 91. ^{13}C-NMR DEPT-135 of 3(OMeDPA)IPN-MA ($CDCl_3$).

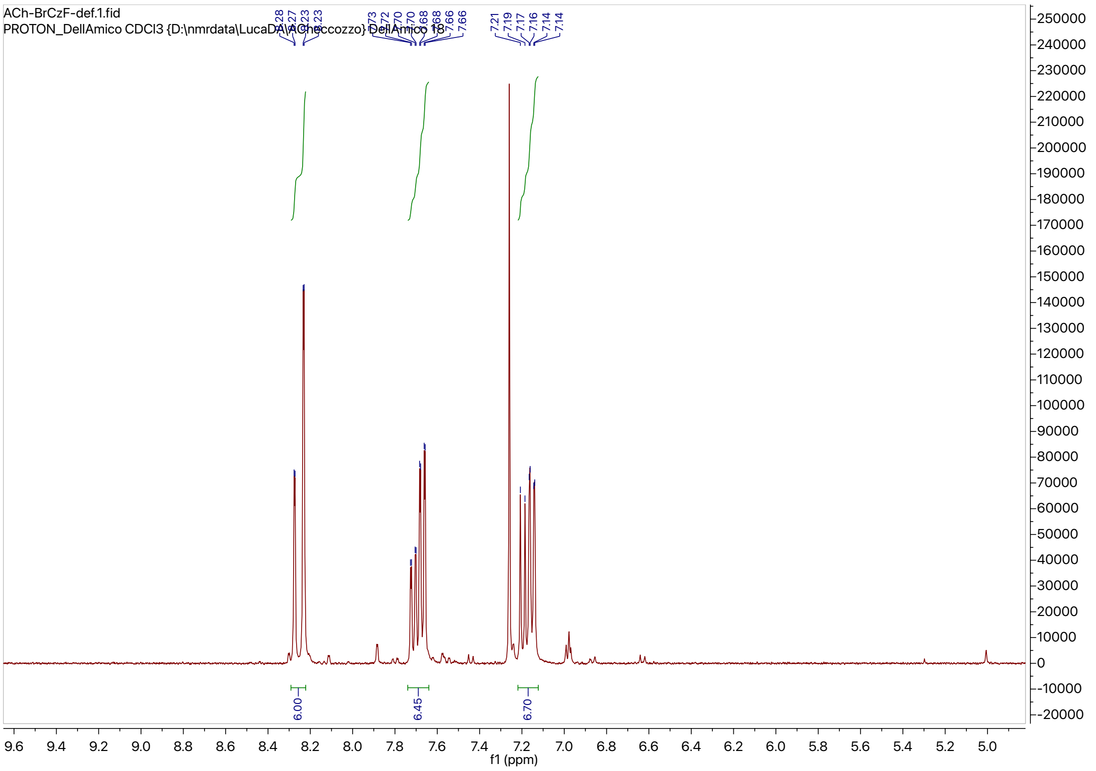

Figure 92. ^{1}H-NMR of 3(BrCz)FIPN ($CDCl_3$).

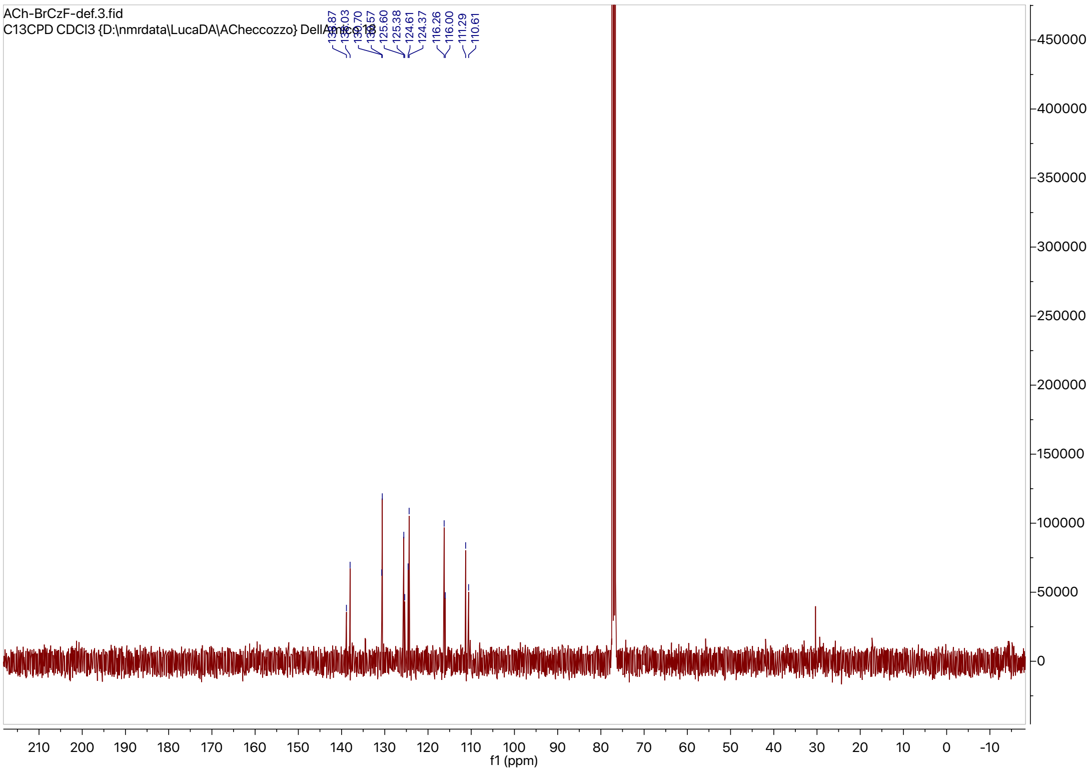

Figure 93. ^{13}C-NMR of 3(BrCz)FIPN (CDCl$_3$).

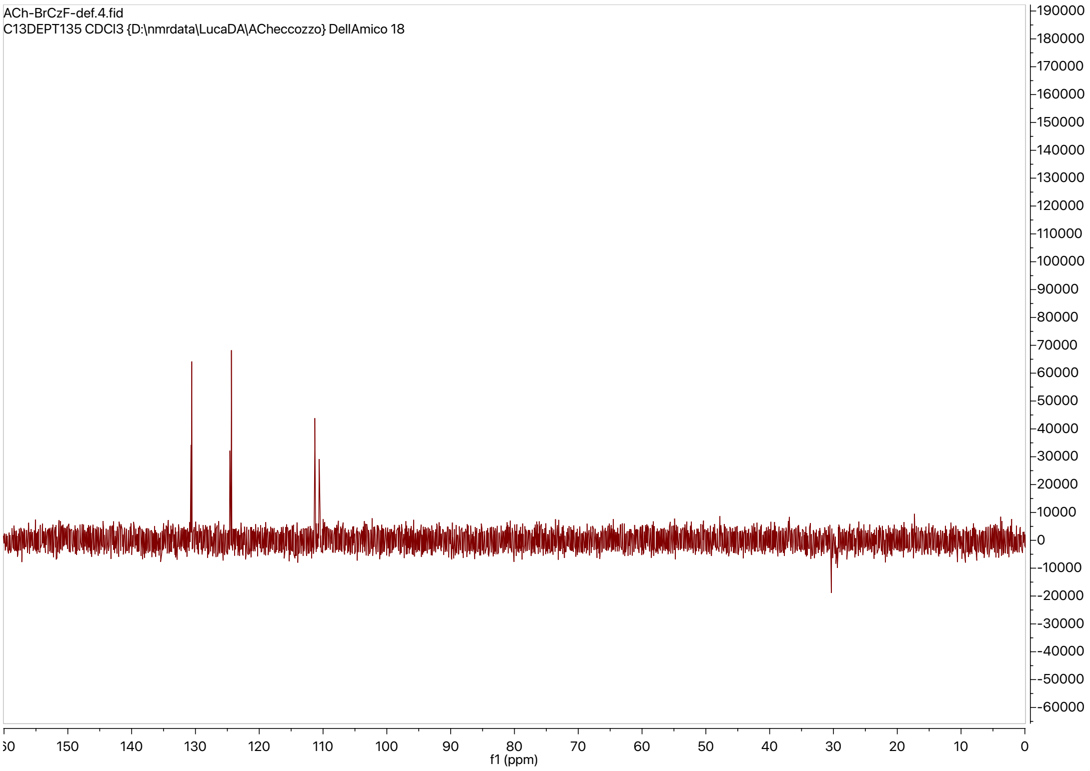

Figure 94. ^{13}C-NMR DEPT-135 of 3(BrCz)FIPN (CDCl$_3$).

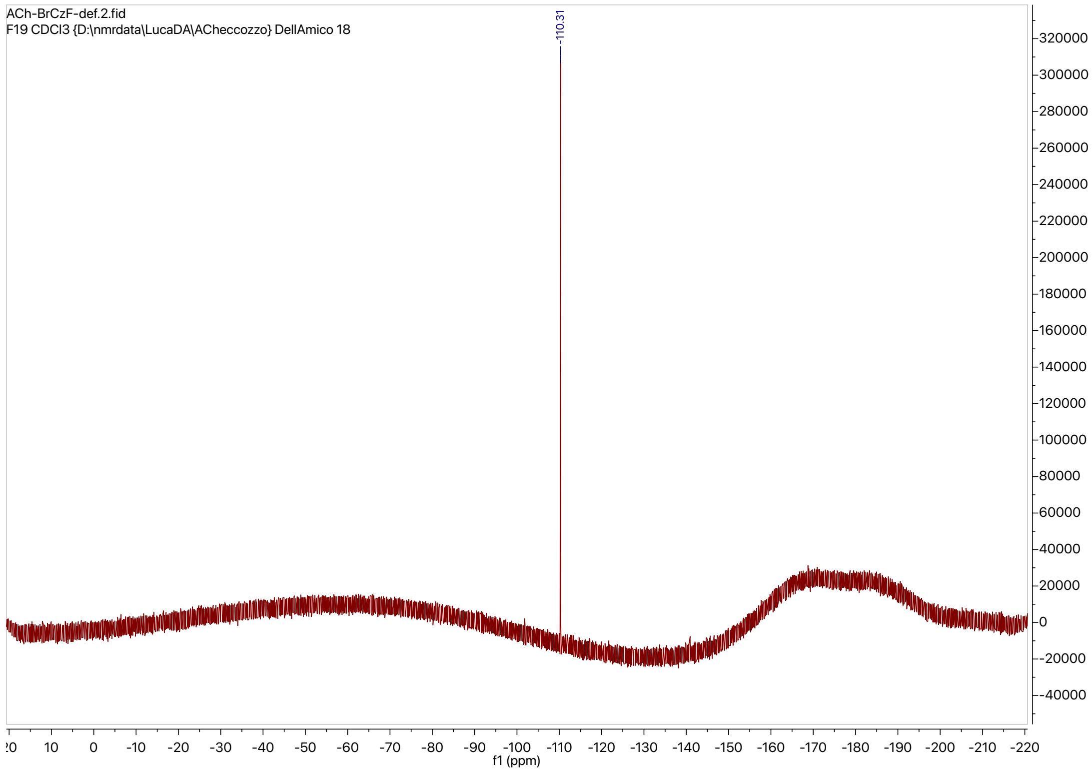

Figure 95. ^{19}F-NMR of 3(BrCz)FIPN (CDCl$_3$).

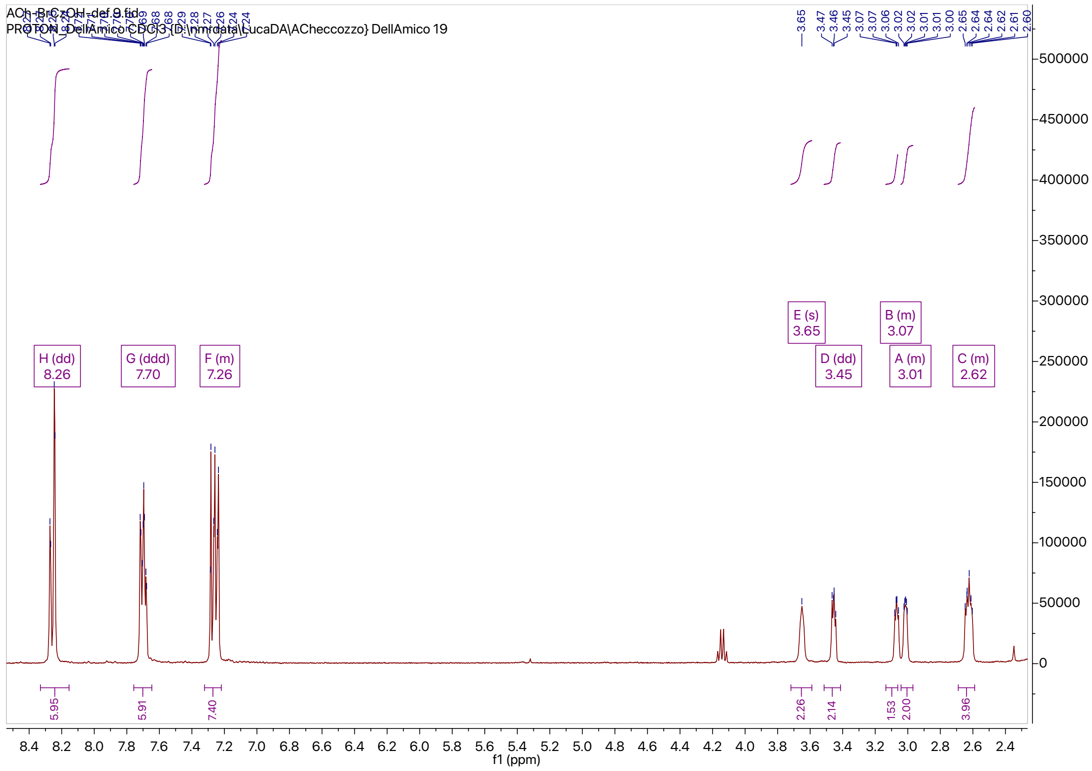

Figure 96. ^{1}H-NMR of 3(BrCz)TEGIPN (CDCl$_3$).

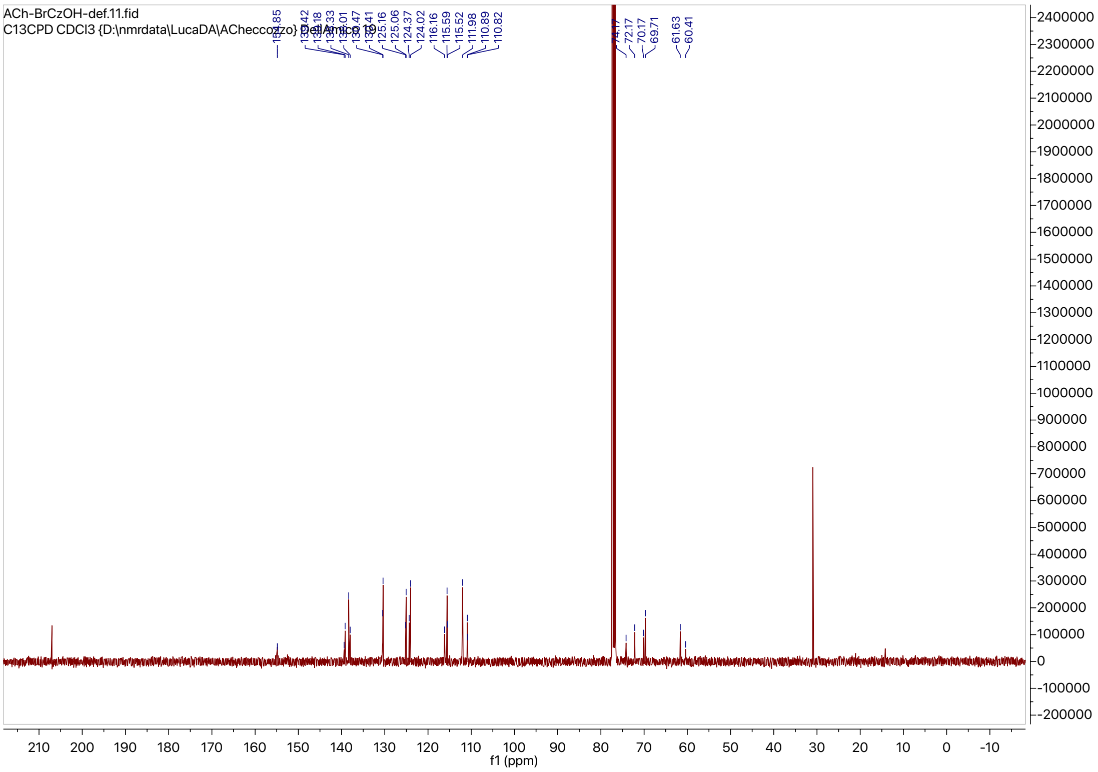

Figure 97. ^{13}C-NMR of 3(BrCz)TEGIPN (CDCl$_3$).

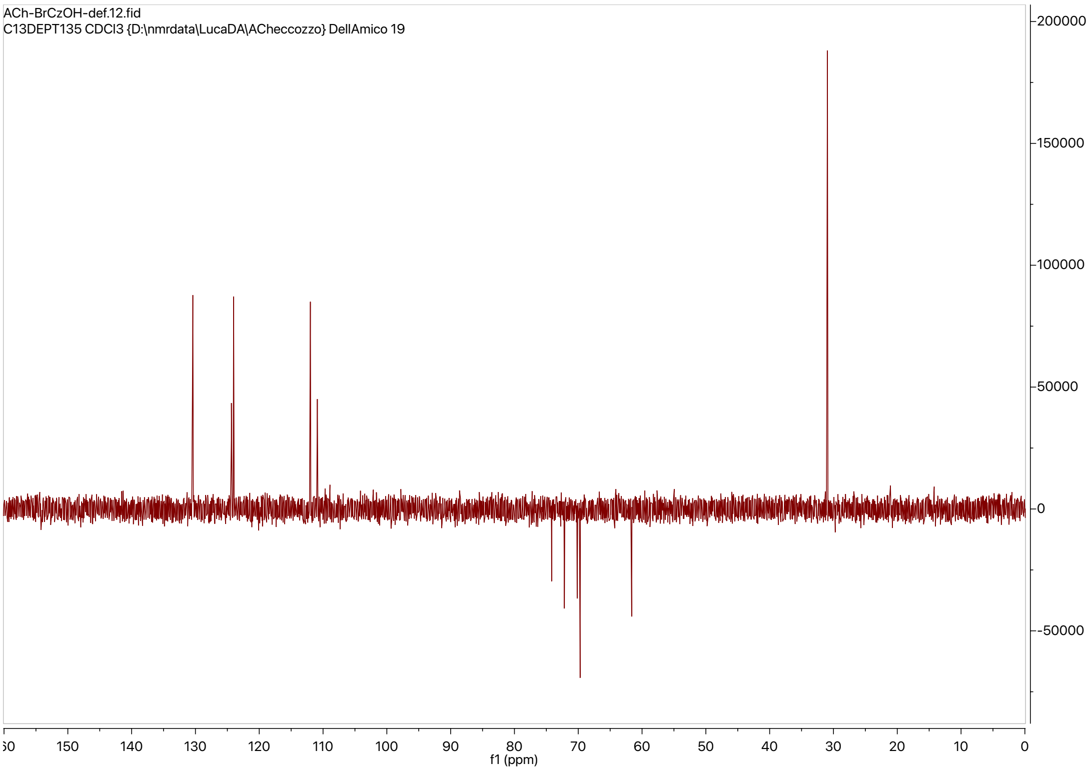

Figure 98. ^{13}C-NMR DEPT-135 of 3(BrCz)TEGIPN (CDCl$_3$).

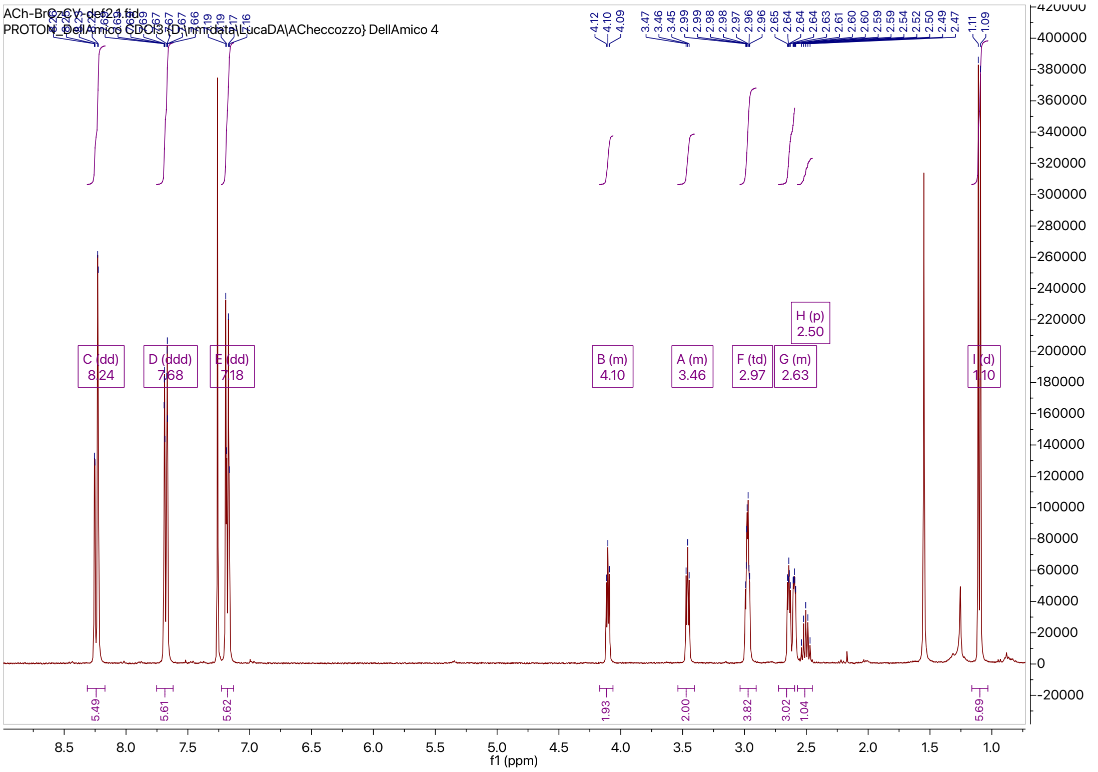

Figure 99. ^{1}H-NMR of 3(BrCz)IPN-^{i}but (CDCl$_3$).

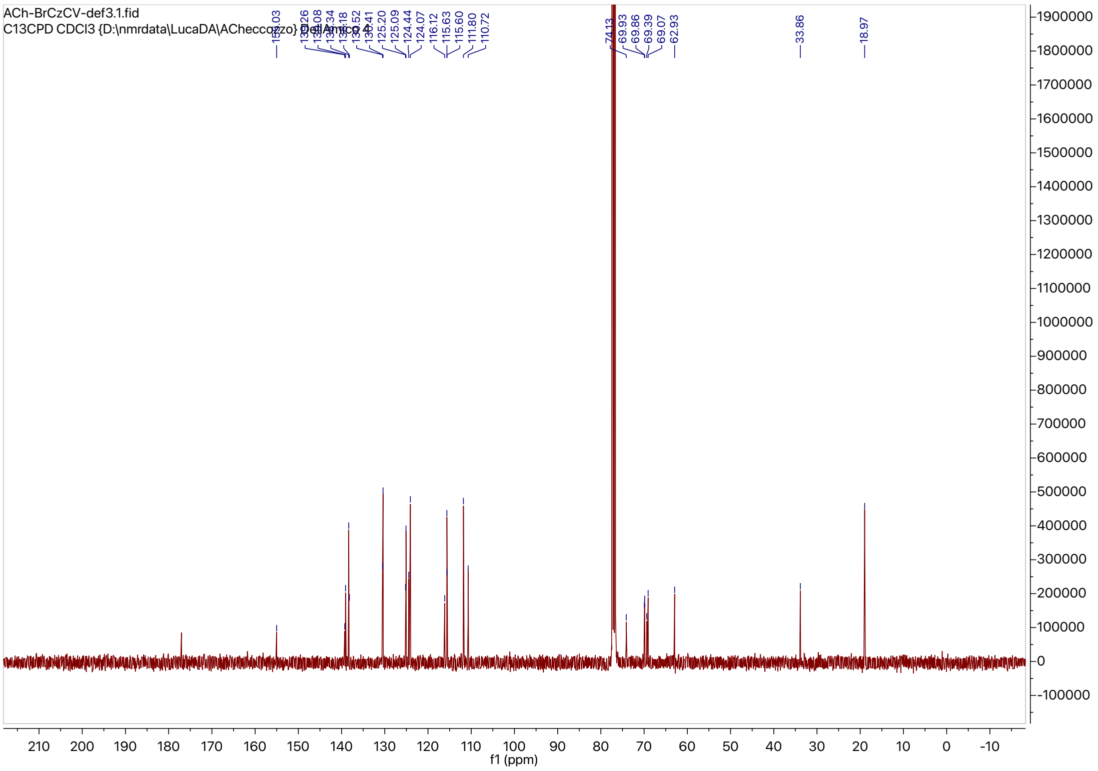

Figure 100. ^{13}C-NMR of 3(BrCz)IPN-^{i}but (CDCl$_3$).

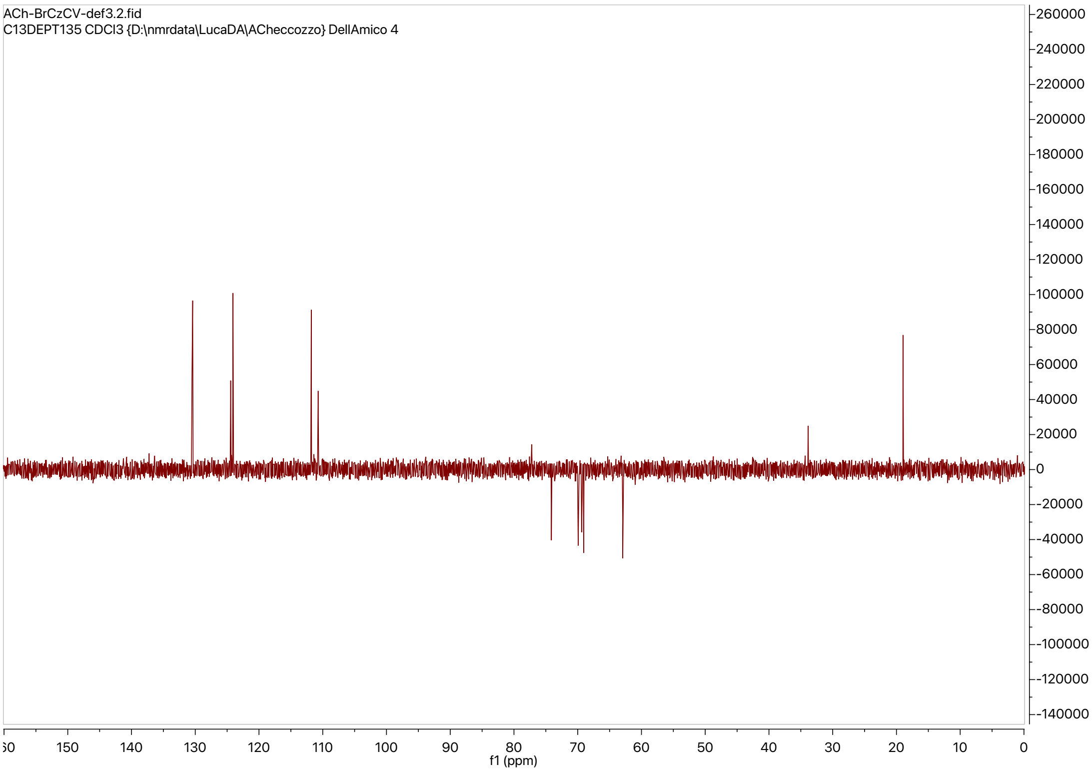

Figure 101. ^{13}C-NMR DEPT-135 of 3(BrCz)IPN-^{i}but (CDCl$_3$).

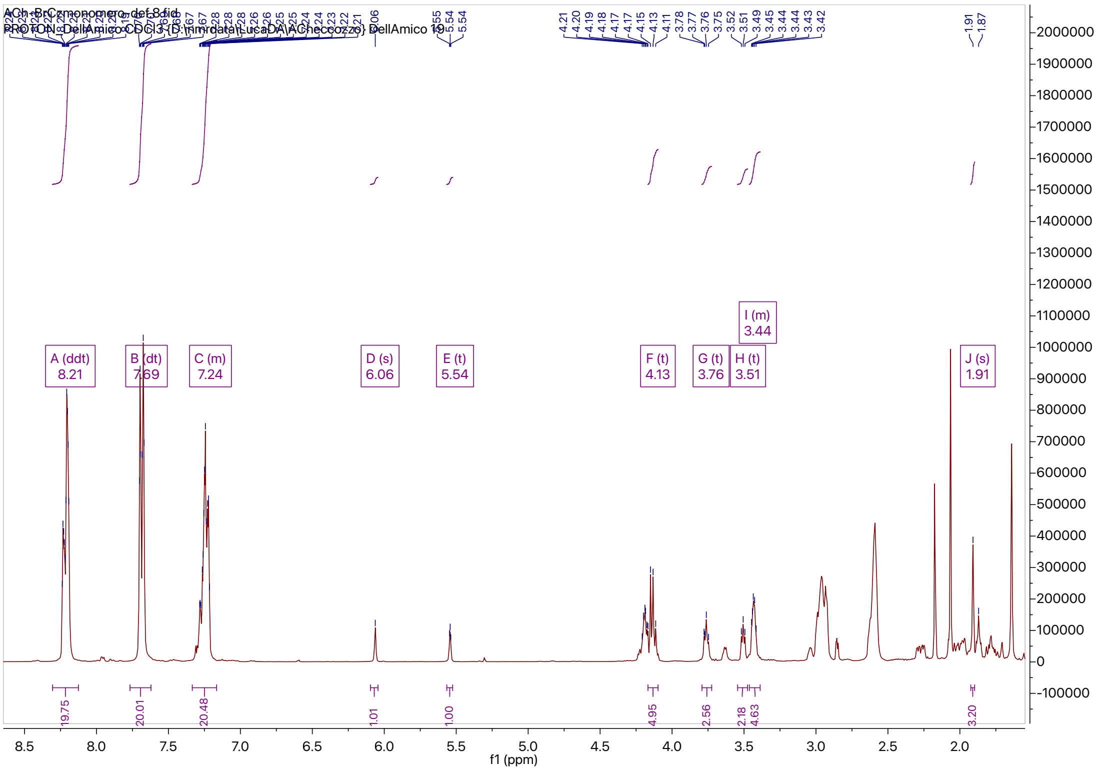

Figure 102. ^{1}H-NMR of 3(BrCz)IPN-MA (CDCl$_3$).

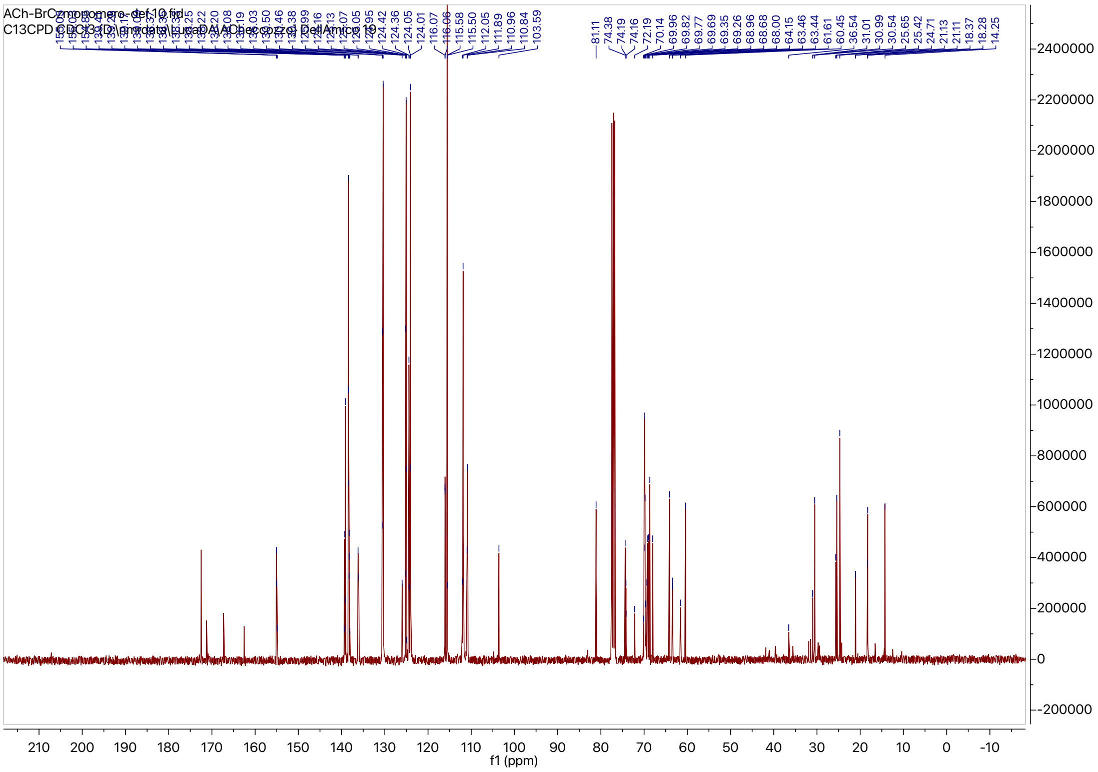

Figure 103. ^{13}C-NMR of 3(BrCz)IPN-MA ($CDCl_3$).

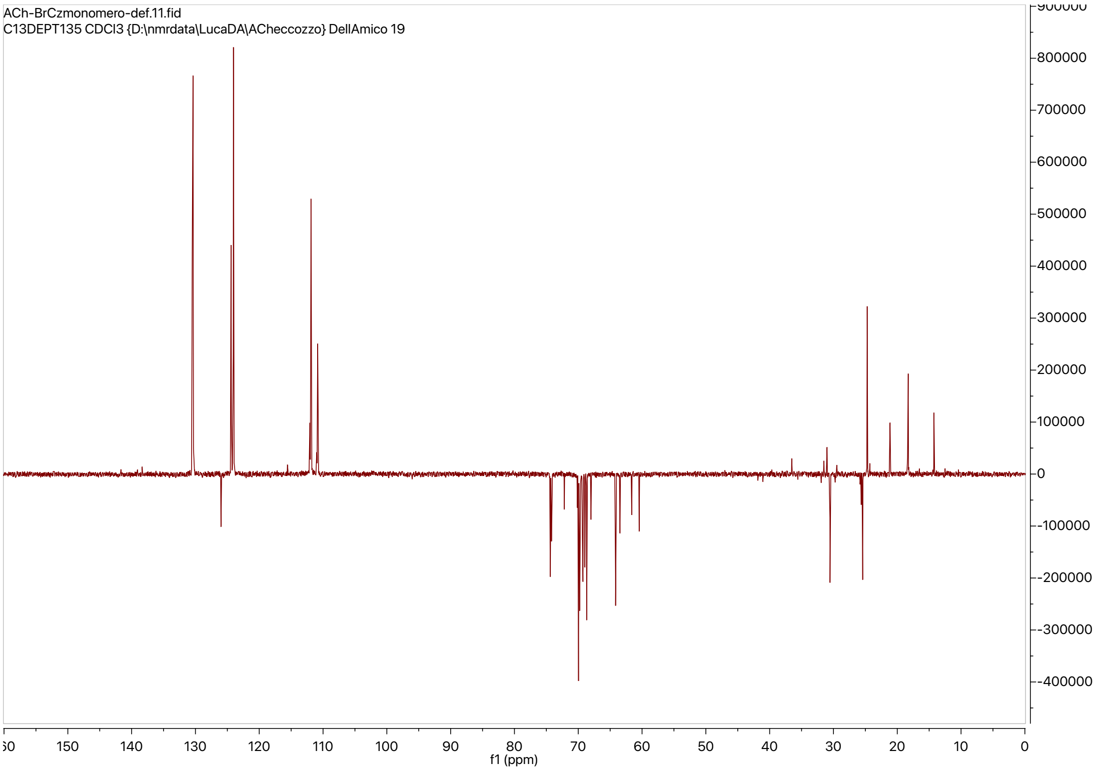

Figure 104. ^{13}C-NMR DEPT-135 of 3(BrCz)IPN-MA ($CDCl_3$).

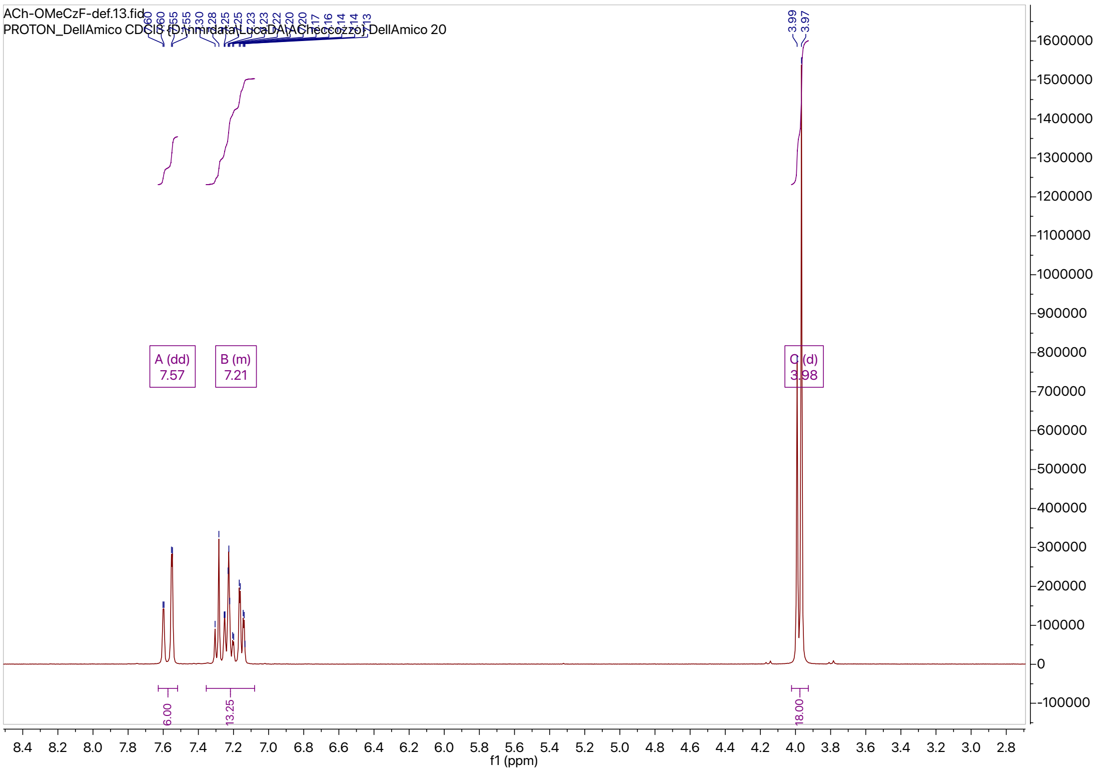

Figure 105. ^{1}H-NMR of 3(OMeCz)FIPN (CDCl$_3$).

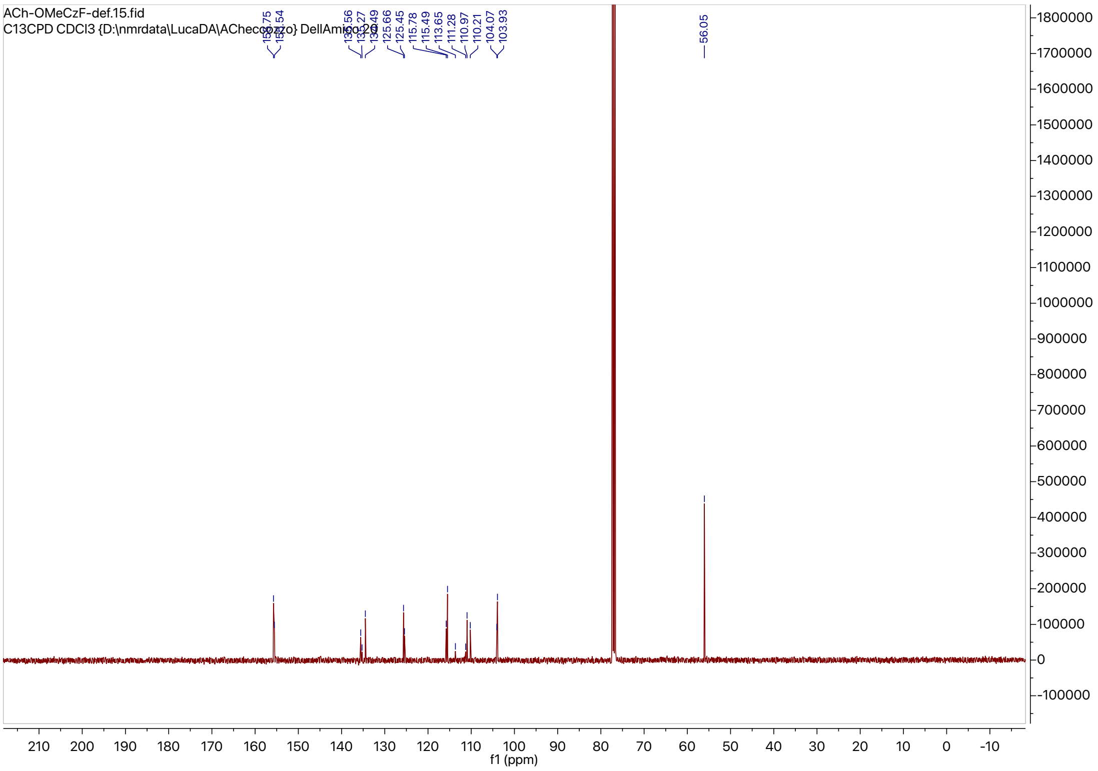

Figure 106. ^{13}C-NMR of 3(OMeCz)FIPN (CDCl$_3$).

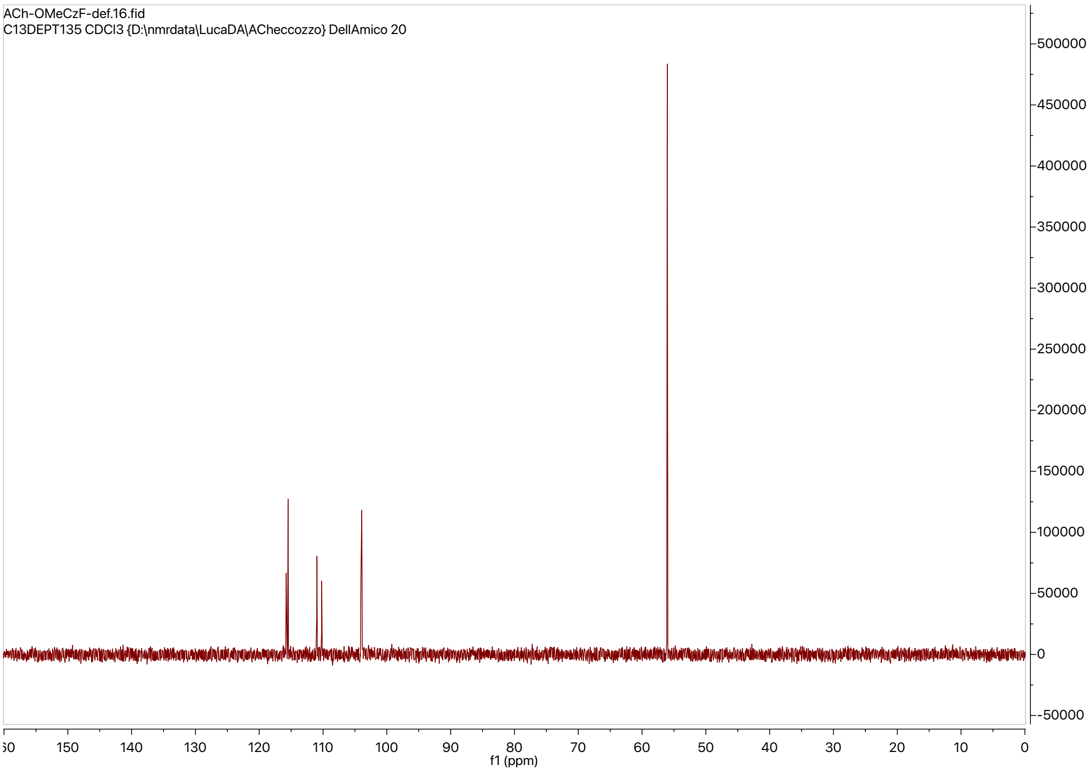

Figure 107. ^{13}C-NMR DEPT-135 of 3(OMeCz)FIPN (CDCl$_3$).

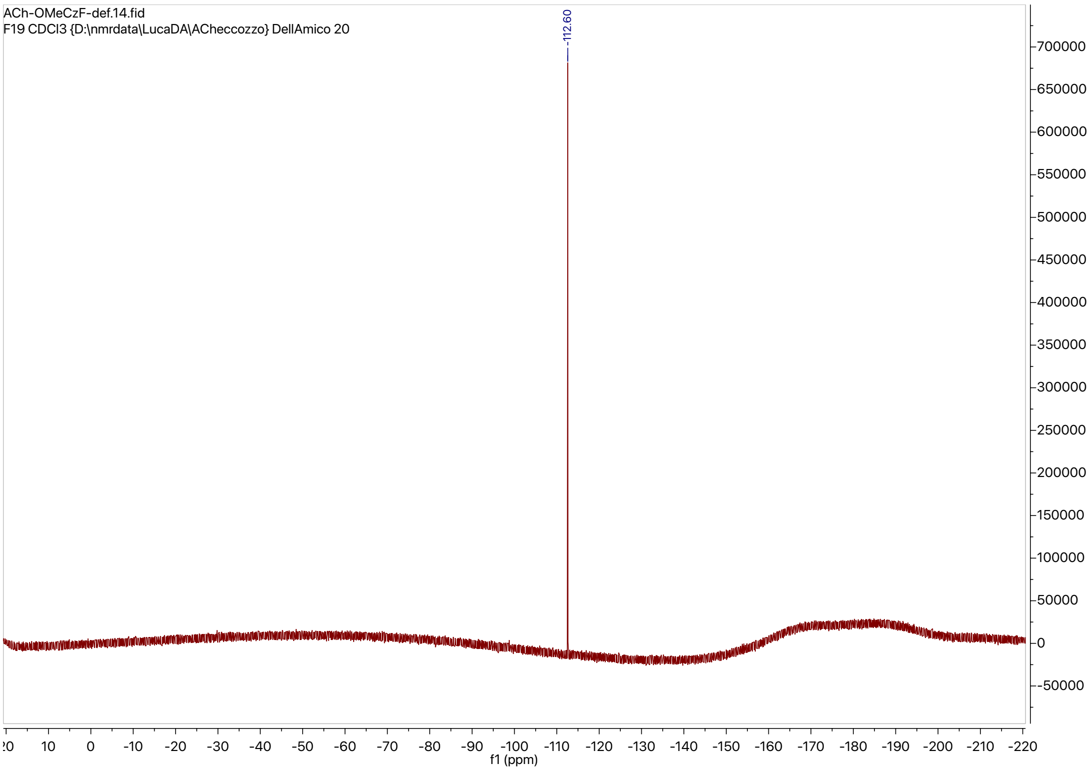

Figure 108. ^{19}F-NMR of 3(OMeCz)FIPN (CDCl$_3$).

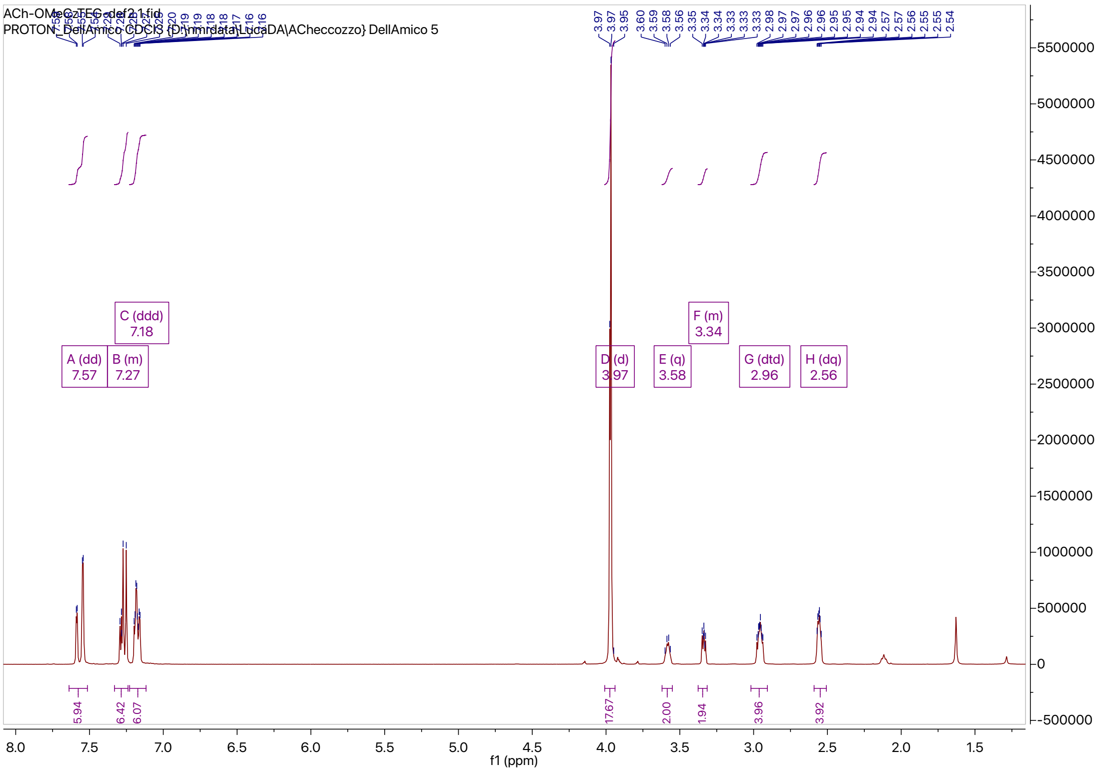

Figure 109. ^{1}H-NMR of 3(OMeCz)TEGIPN (CDCl$_3$).

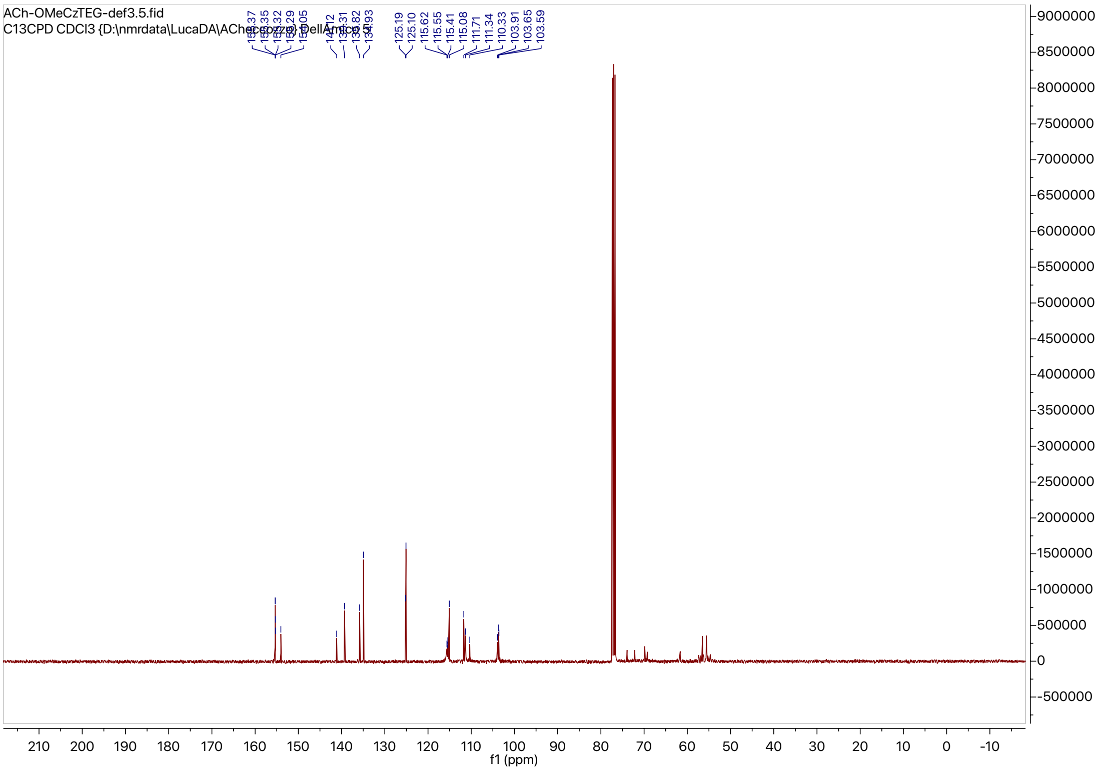

Figure 110. ^{13}C-NMR of 3(OMeCz)TEGIPN (CDCl$_3$).

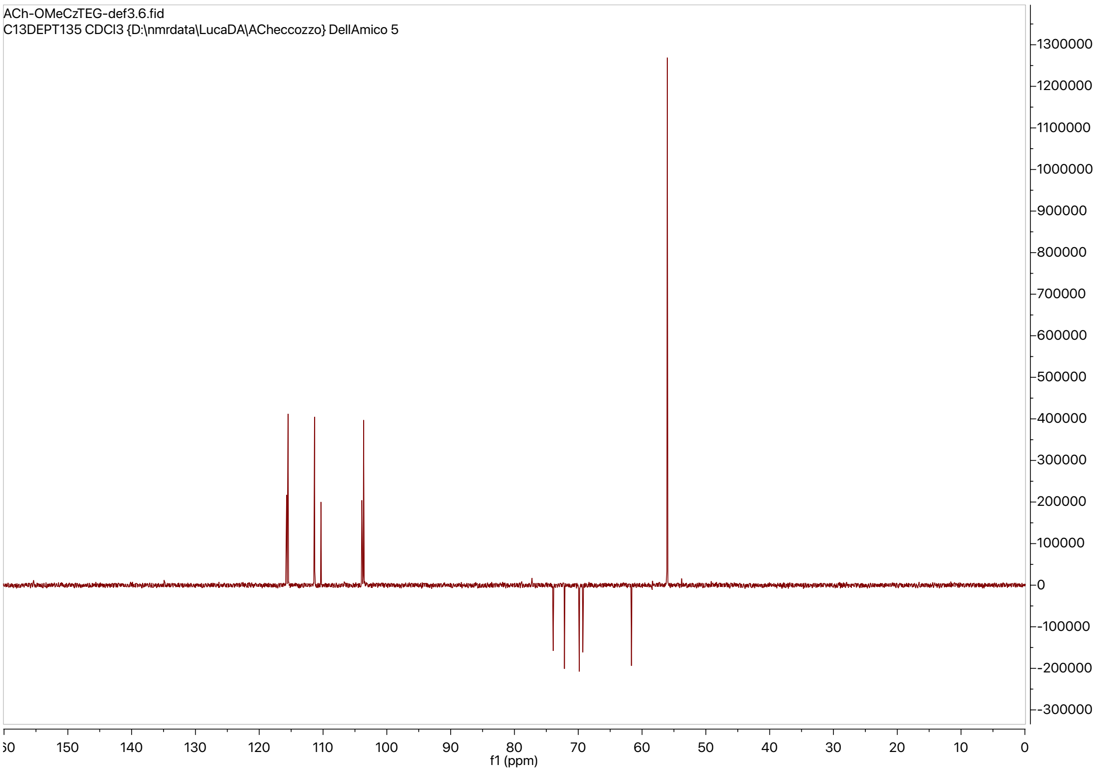

Figure 111. ^{13}C-NMR DEPT-135 of 3(OMeCz)TEGIPN (CDCl$_3$).

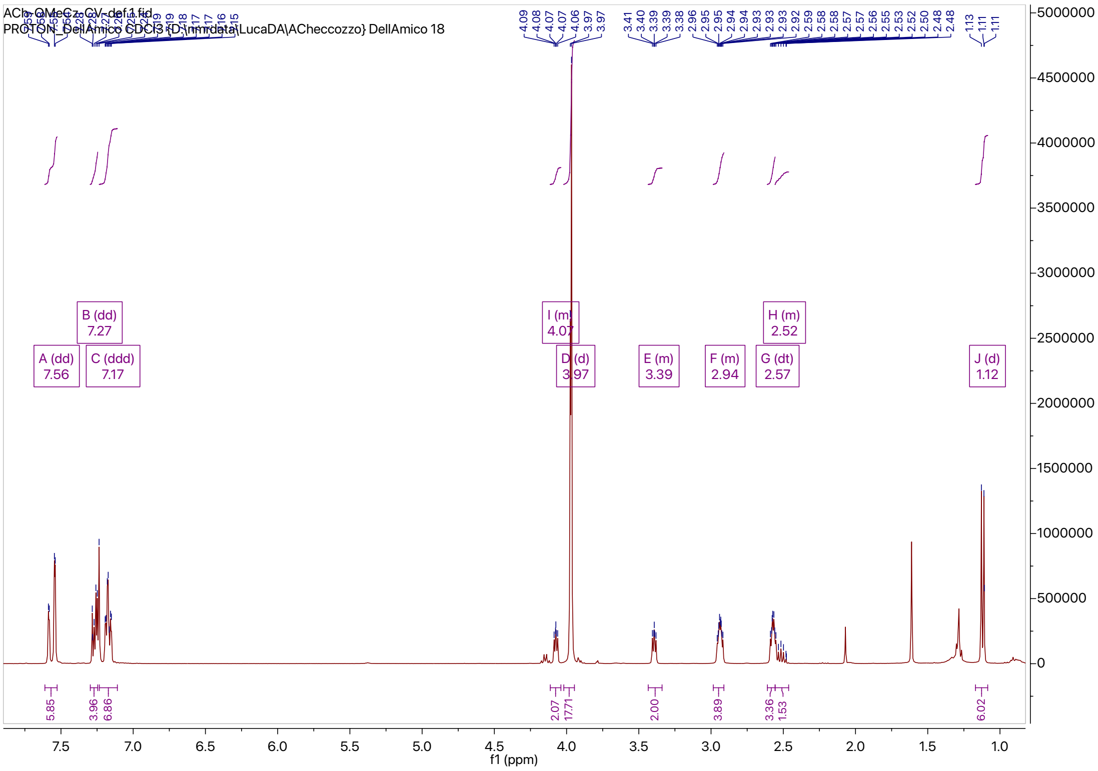

Figure 112. ^{1}H-NMR of 3(OMeCz)IPN-^{i}but (CDCl$_3$).

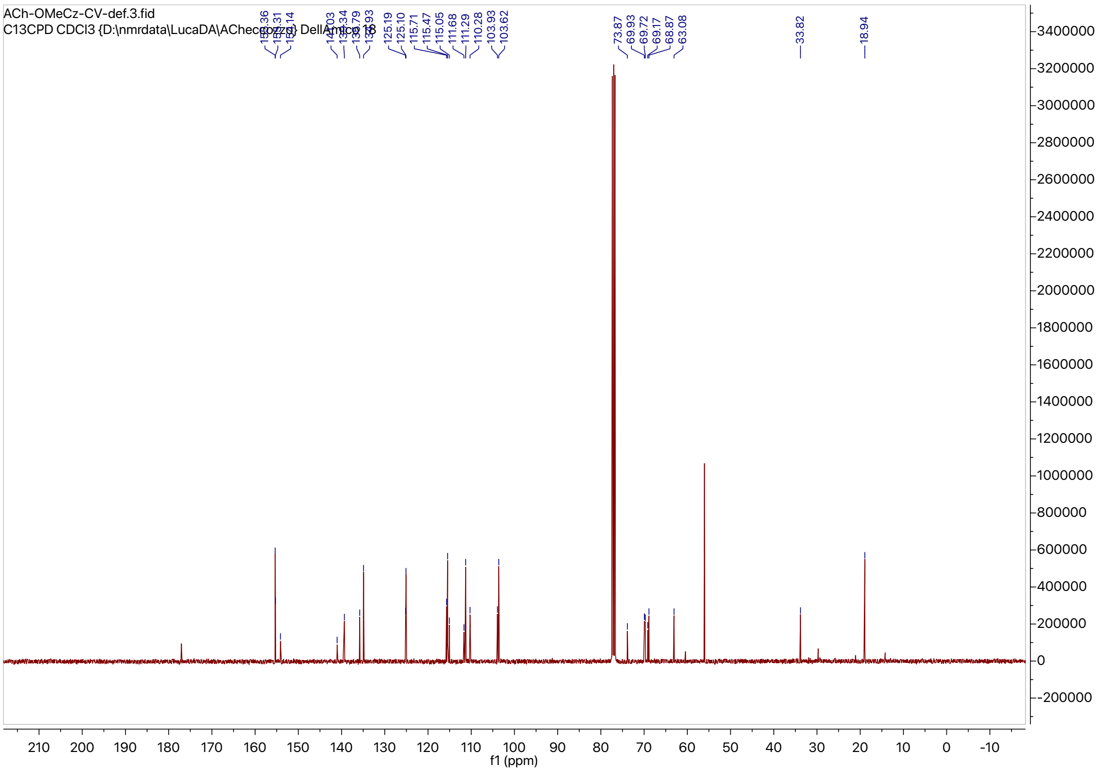

Figure 113. ^{13}C-NMR of 3(OMeCz)IPN-^{i}but (CDCl$_3$).

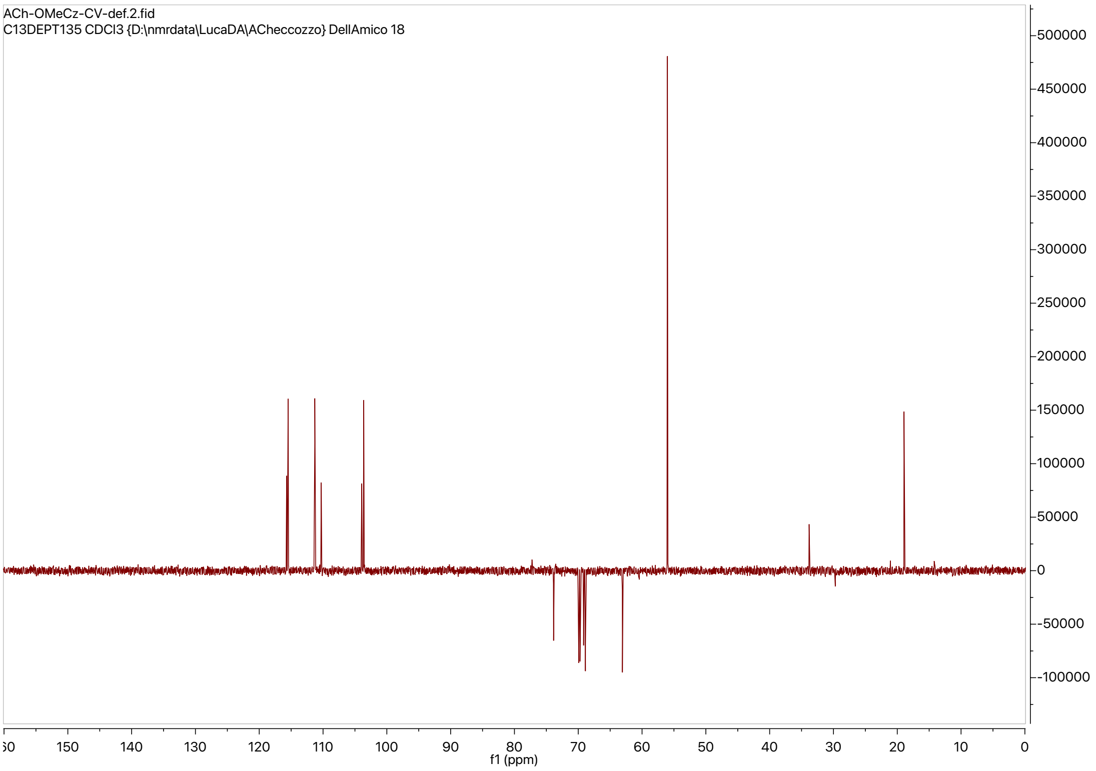

Figure 114. ^{13}C-NMR DEPT-135 of 3(OMeCz)IPN-^{i}but (CDCl$_3$).

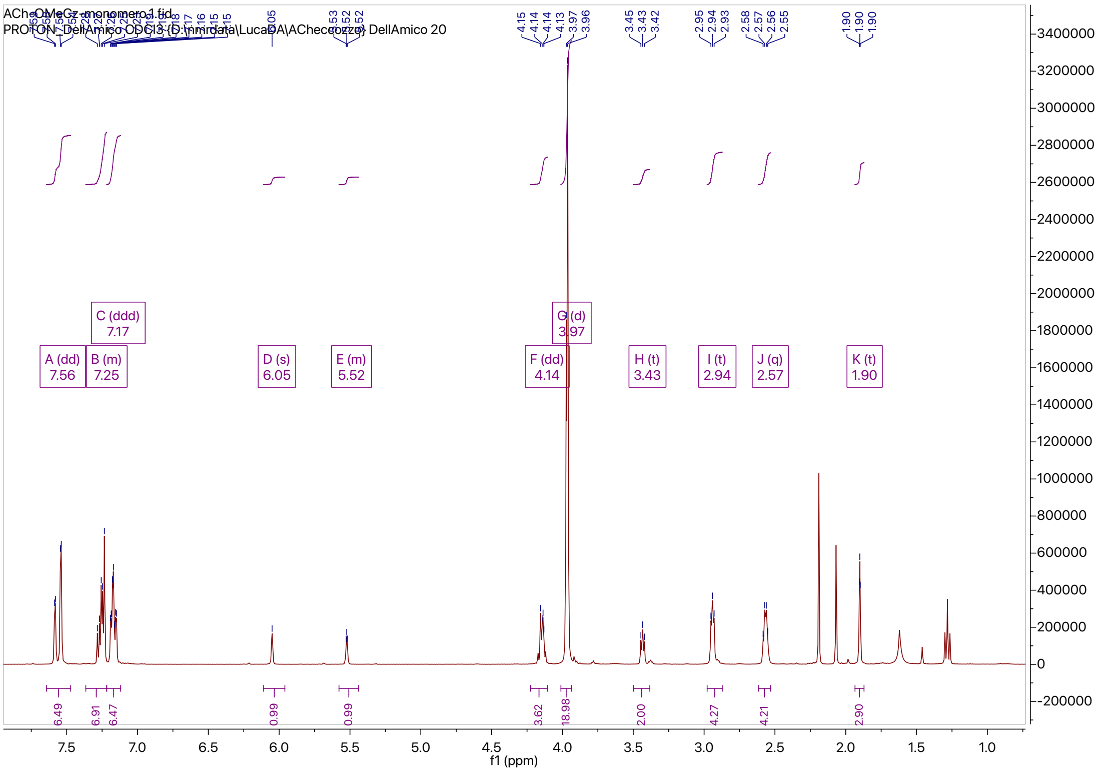

Figure 115. ^{1}H-NMR of 3(OMeCz)IPN-MA (CDCl$_3$).

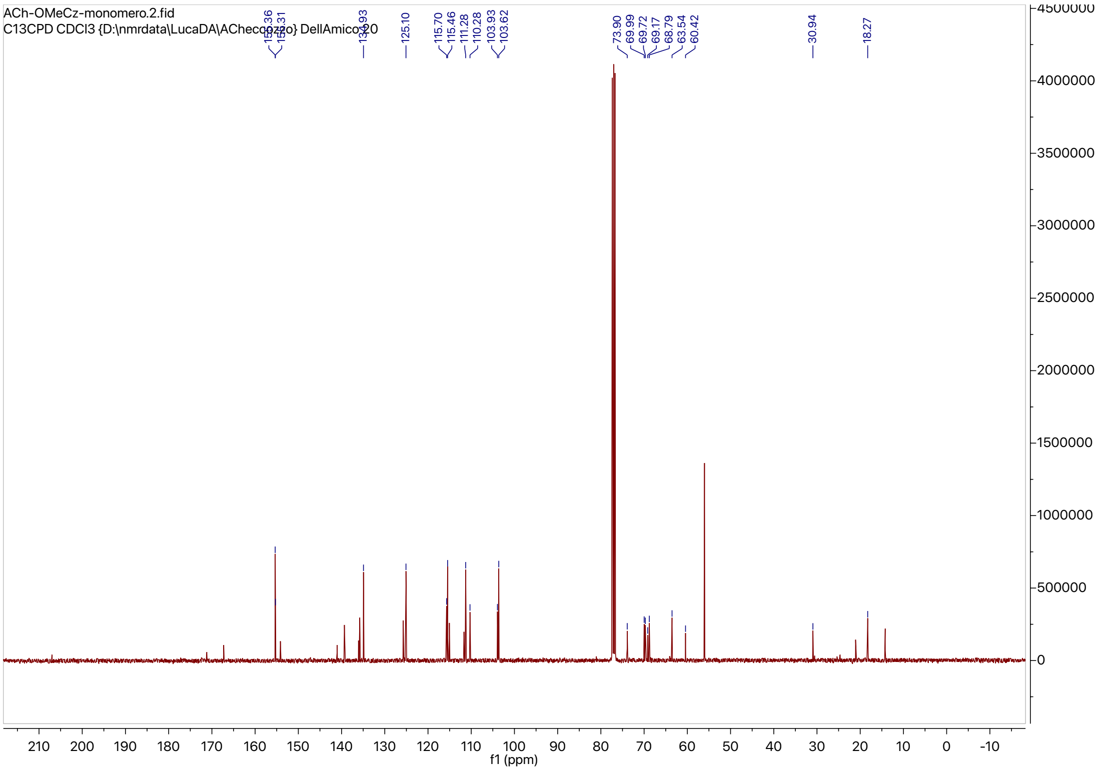

Figure 116. ^{13}C-NMR of 3(OMeCz)IPN-MA (CDCl$_3$).

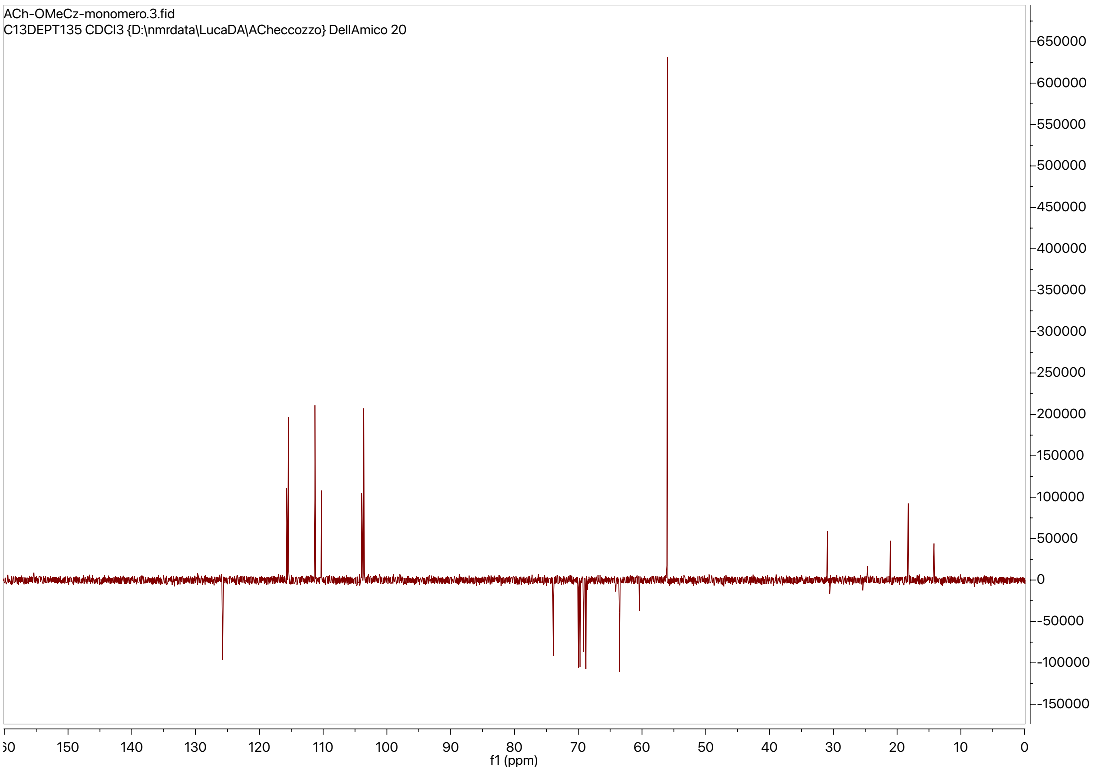

Figure 117. ^{13}C-NMR DEPT-135 of 3(OMeCz)IPN-MA (CDCl$_3$).

References

1. Buzzetti, L., Crisenza, G. E. M. & Melchiorre, P. Mechanistische Studien in der Photokatalyse. *Angewandte Chemie* **131**, 3768–3786 (2019).

2. Buglioni, L., Raymenants, F., Slattery, A., Zondag, S. D. A. & Noël, T. Technological Innovations in Photochemistry for Organic Synthesis: Flow Chemistry, High-Throughput Experimentation, Scale-up, and Photoelectrochemistry. *Chemical Reviews* vol. 122 2752–2906 Preprint at https://doi.org/10.1021/acs.chemrev.1c00332 (2022).

3. König, B. Photocatalysis in Organic Synthesis – Past, Present, and Future. *European Journal of Organic Chemistry* vol. 2017 1979–1981 Preprint at https://doi.org/10.1002/ejoc.201700420 (2017).

4. Beeler, A. B. Introduction: Photochemistry in Organic Synthesis. *Chemical Reviews* vol. 116 9629–9630 Preprint at https://doi.org/10.1021/acs.chemrev.6b00378 (2016).

5. Giacomo Ciamician. Sur les actions de la lumière. *Bull. Soc. Chim. Fr.* **3–4**, I–XXVII (1908).

6. Albini, A. & Dichiarante, V. The ‘belle époque’ of photochemistry. *Photochemical and Photobiological Sciences* **8**, 248–254 (2009).

7. Li, S. *et al.* Visible light-enabled selective depolymerization of oxidized lignin by an organic photocatalyst. *Chemical Communications* **56**, 11243–11246 (2020).

8. Loh, Y. Y. *et al.* Photoredox-catalyzed deuteration and tritiation of pharmaceutical compounds. *Science (1979)* **358**, 1182–1187 (2017).

9. Halperin, S. D. *et al.* Development of a Direct Photocatalytic C-H Fluorination for the Preparative Synthesis of Odanacatib. *Org Lett* **17**, 5200–5203 (2015).

10. Bancroft, W. D. The Electrochemistry of Light, X. *J Phys Chem* **17**, 596–602 (2002).

11. H. H. Jaffe & A. L. Miller. The Fates of Electronic Excitation Energy. *Journal of Chemical Edducation* **43**, 469–473 (1966).

12. P.A.M. Dirac. The Quantum Theory of the Electron. in *The Quantum Theory of the Electron* vol. 43 610–624 (1928).

13. H. D. Roth. History of photochemistry. *History of photochemistry* vol. 32 1–20 (1988).

14. Roth, H. D. The Beginnings of Organic Photochemistry. *Angewandte Chemie International Edition* **28**, 1193–1207 (1989).

15. Hoffmann, N. Photochemical Reactions as Key Steps in Organic Synthesis. *Chem Rev* **108**, 1052–1103 (2008).

16. Albini, A. & Germani, L. Photochemical Methods. in *Handbook of Synthetic Photochemistry* 1–24 (2009).

17. Fréneau, M. & Hoffmann, N. The Paternò-Büchi reaction—Mechanisms and application to organic synthesis. *Journal of Photochemistry and Photobiology C: Photochemistry Reviews* vol. 33 83–108 Preprint at https://doi.org/10.1016/j.jphotochemrev.2017.10.002 (2017).

18. Zheng, J., Dong, X. & Yoon, T. P. Divergent Photocatalytic Reactions of α-Ketoesters under Triplet Sensitization and Photoredox Conditions. *Org Lett* **22**, 6520–6525 (2020).

19. Bortolato, T. *et al.* The Rational Design of Reducing Organophotoredox Catalysts Unlocks Proton-Coupled Electron-Transfer and Atom Transfer Radical Polymerization Mechanisms. *J Am Chem Soc* **145**, 1835–1846 (2023).

20. Zhang, J. *et al.* Surface-modified carbon nanotubes catalyze oxidative dehydrogenation of n-butane. *Science (1979)* **322**, 73–77 (2008).

21. Prier, C. K., Rankic, D. A. & MacMillan, D. W. C. Visible light photoredox catalysis with transition metal complexes: Applications in organic synthesis. *Chemical Reviews* vol. 113 5322–5363 Preprint at https://doi.org/10.1021/cr300503r (2013).

22. Ischay, M. A., Anzovino, M. E., Du, J. & Yoon, T. P. Efficient visible light photocatalysis of [2+2] enone cycloadditions. *J Am Chem Soc* **130**, 12886–12887 (2008).

23. Tucker, J. W. & Stephenson, C. R. J. Shining light on photoredox catalysis: Theory and synthetic applications. *Journal of Organic Chemistry* **77**, 1617–1622 (2012).

24. Teegardin, K., Day, J. I., Chan, J. & Weaver, J. Advances in Photocatalysis: A Microreview of Visible Light Mediated Ruthenium and Iridium Catalyzed Organic Transformations. *Org Process Res Dev* **20**, 1156–1163 (2016).

25. Huang, H. *et al.* Visible-Light-Promoted Nickel- and Organic-Dye-Cocatalyzed Formylation Reaction of Aryl Halides and Triflates and Vinyl Bromides with Diethoxyacetic Acid as a Formyl Equivalent. *Angewandte Chemie* **129**, 1522–1527 (2017).

26. Bryden, M. A. & Zysman-Colman, E. Organic thermally activated delayed fluorescence (TADF) compounds used in photocatalysis. *Chem Soc Rev* **50**, 7587–7680 (2021).

27. A M D irac, B. P. & John, S. *The Quantum Theory o f the Emission and Absorption of Radiation*. https://royalsocietypublishing.org/.

28. Buzzetti, L., Crisenza, G. E. M. & Melchiorre, P. Mechanistische Studien in der Photokatalyse. *Angewandte Chemie* **131**, 3768–3786 (2019).

29. Capaldo, L. & Ravelli, D. Hydrogen Atom Transfer (HAT): A Versatile Strategy for Substrate Activation in Photocatalyzed Organic Synthesis. *European Journal of Organic Chemistry* vol. 2017 2056–2071 Preprint at https://doi.org/10.1002/ejoc.201601485 (2017).

30. Juliá, F., Constantin, T. & Leonori, D. Applications of Halogen-Atom Transfer (XAT) for the Generation of Carbon Radicals in Synthetic Photochemistry and Photocatalysis. *Chem Rev* **122**, 2292–2352 (2022).

31. Strieth-Kalthoff, F. & Glorius, F. Triplet Energy Transfer Photocatalysis: Unlocking the Next Level. *Chem* **6**, 1888–1903 (2020).

32. Förster, T. Zwischenmolekulare Energiewanderung und Fluoreszenz. *Ann Phys* **437**, 55–75 (1948).

33. Strieth-Kalthoff, F., James, M. J., Teders, M., Pitzer, L. & Glorius, F. Energy transfer catalysis mediated by visible light: principles, applications, directions. *Chem Soc Rev* **47**, 7190–7202 (2018).

34. Algar, W. R., Hildebrandt, N., Vogel, S. S. & Medintz, I. L. FRET as a biomolecular research tool — understanding its potential while avoiding pitfalls. *Nat Methods* **16**, 815–829 (2019).

35. Rivera, J. J., Trinh, C. & Kim, J. E. Photoinduced Electron Transfer from the Tryptophan Triplet State in Zn-Azurin. *ACS Physical Chemistry Au* **3**, 63–73 (2023).

36. Zhang, Y., Lee, T. S., Petersen, J. L. & Milsmann, C. A Zirconium Photosensitizer with a Long-Lived Excited State: Mechanistic Insight into Photoinduced Single-Electron Transfer. *J Am Chem Soc* **140**, 5934–5947 (2018).

37. Bortolato, T. *et al.* The Rational Design of Reducing Organophotoredox Catalysts Unlocks Proton-Coupled Electron-Transfer and Atom Transfer Radical Polymerization Mechanisms. *J Am Chem Soc* **145**, 1835–1846 (2023).

38. Bortolato, T., Cuadros, S., Simionato, G. & Dell'Amico, L. The advent and development of organophotoredox catalysis. *Chemical Communications* **58**, 1263–1283 (2022).

39. Vega-Peñaloza, A., Mateos, J., Companyó, X., Escudero-Casao, M. & Dell'Amico, L. A Rational Approach to Organo-Photocatalysis: Novel Designs and Structure-Property Relationships. *Angewandte Chemie - International Edition* vol. 60 1082–1097 Preprint at https://doi.org/10.1002/anie.202006416 (2021).

40. Bortolato, T. *et al.* The Rational Design of Reducing Organophotoredox Catalysts Unlocks Proton-Coupled Electron-Transfer and Atom Transfer Radical Polymerization Mechanisms. *J Am Chem Soc* **145**, 1835–1846 (2023).

41. Zhang, Y. *et al.* Delayed fluorescence from a zirconium(iv) photosensitizer with ligand-to-metal charge-transfer excited states. *Nat Chem* **12**, 345–352 (2020).

42. Bouzrati-Zerelli, M. *et al.* A novel class of photoinitiators with a thermally activated delayed fluorescence (TADF) property. *New Journal of Chemistry* **42**, 8261–8270 (2018).

43. Bryden, M. A. & Zysman-Colman, E. Organic thermally activated delayed fluorescence (TADF) compounds used in photocatalysis. *Chemical Society Reviews* vol. 50 7587–7680 Preprint at https://doi.org/10.1039/d1cs00198a (2021).

44. Cardeynaels, T. *et al.* Dominant dimer emission provides colour stability for red thermally activated delayed fluorescence emitter. *J Mater Chem C Mater* **10**, 5840–5848 (2022).

45. Luo, J. & Zhang, J. Donor-Acceptor Fluorophores for Visible-Light-Promoted Organic Synthesis: Photoredox/Ni Dual Catalytic C(sp3)-C(sp2) Cross-Coupling. *ACS Catal* **6**, 873–877 (2016).

46. Mateos, J. *et al.* Naphthochromenones: Organic Bimodal Photocatalysts Engaging in Both Oxidative and Reductive Quenching Processes. *Angewandte Chemie* **132**, 1318–1328 (2020).

47. Speckmeier, E., Fischer, T. G. & Zeitler, K. A Toolbox Approach to Construct Broadly Applicable Metal-Free Catalysts for Photoredox Chemistry: Deliberate Tuning of Redox Potentials and Importance of Halogens in Donor-Acceptor Cyanoarenes. *J Am Chem Soc* **140**, 15353–15365 (2018).

48. Speckmeier, E., Fischer, T. G. & Zeitler, K. *A Toolbox Approach to Construct Broadly Applicable Metal-Free Catalysts for Photoredox Chemistry-*

Deliberate Tuning of Redox Potentials and Importance of Halogens in Donor-Acceptor Cyanoarenes.

49. Whitfield, R. *et al.* Tailoring polymer dispersity and shape of molecular weight distributions: Methods and applications. *Chemical Science* vol. 10 8724–8734 Preprint at https://doi.org/10.1039/c9sc03546j (2019).

50. Edmondson, S., Osborne, V. L. & Huck, W. T. S. Polymer brushes via surface-initiated polymerizations. *Chem Soc Rev* **33**, 14–22 (2004).

51. Zoppe, J. O. *et al.* Surface-Initiated Controlled Radical Polymerization: State-of-the-Art, Opportunities, and Challenges in Surface and Interface Engineering with Polymer Brushes. *Chem Rev* **117**, 1105–1318 (2017).

52. Corrigan, N. *et al.* Reversible-deactivation radical polymerization (Controlled/living radical polymerization): From discovery to materials design and applications. *Progress in Polymer Science* vol. 111 Preprint at https://doi.org/10.1016/j.progpolymsci.2020.101311 (2020).

53. Wang, J.-S. & Matyjaszewski, K. Controlled/"living" radical polymerization. atom transfer radical polymerization in the presence of transition-metal complexes. *J Am Chem Soc* **117**, 5614–5615 (1995).

54. Kato, M., Kamigaito, M., Sawamoto, M. & Higashimura, T. Polymerization of Methyl Methacrylate with the Carbon Tetrachloride/Dichlorotris-(triphenylphosphine)ruthenium(II)/Methylaluminum Bis(2,6-di-tert-butylphenoxide) Initiating System: Possibility of Living Radical Polymerization. *Macromolecules* **28**, 1721–1723 (1995).

55. Krys, P. & Matyjaszewski, K. Kinetics of Atom Transfer Radical Polymerization. *European Polymer Journal* vol. 89 482–523 Preprint at https://doi.org/10.1016/j.eurpolymj.2017.02.034 (2017).

56. Pan, X., Fantin, M., Yuan, F. & Matyjaszewski, K. Externally controlled atom transfer radical polymerization. *Chem Soc Rev* **47**, 5457–5490 (2018).

57. Shi, B. *et al.* Development of ICAR ATRP–Based Polymerization-Induced Self-Assembly and Its Application in the Preparation of Organic–Inorganic Nanoparticles. *Macromol Rapid Commun* **40**, (2019).

58. Krys, P., Wang, Y., Matyjaszewski, K. & Harrisson, S. Radical Generation and Termination in SARA ATRP of Methyl Acrylate: Effect of Solvent, Ligand, and Chain Length. *Macromolecules* **49**, 2977–2984 (2016).

59. Konkolewicz, D., Schröder, K., Buback, J., Bernhard, S. & Matyjaszewski, K. Visible Light and Sunlight Photoinduced ATRP with ppm of Cu Catalyst. *ACS Macro Lett* **1**, 1219–1223 (2012).

60. Chmielarz, P. *et al.* Electrochemically mediated atom transfer radical polymerization (eATRP). *Prog Polym Sci* **69**, 47–78 (2017).

61. Jakubowski, W., Min, K. & Matyjaszewski, K. Activators regenerated by electron transfer for atom transfer radical polymerization of styrene. *Macromolecules* **39**, 39–45 (2006).

62. Kwak, Y. & Matyjaszewski, K. ARGET ATRP of methyl methacrylate in the presence of nitrogen-based ligands as reducing agents. *Polym Int* **58**, 242–247 (2009).

63. Min, K., Gao, H. & Matyjaszewski, K. Use of ascorbic acid as reducing agent for synthesis of well-defined polymers by ARGET ATRP. *Macromolecules* **40**, 1789–1791 (2007).

64. Tsarevsky, N. V. & Jakubowski, W. Atom transfer radical polymerization of functional monomers employing Cu-based catalysts at low concentration: Polymerization of glycidyl methacrylate. *J Polym Sci A Polym Chem* **49**, 918–925 (2011).

65. Horn, M. & Matyjaszewski, K. Solvent effects on the activation rate constant in atom transfer radical polymerization. *Macromolecules* **46**, 3350–3357 (2013).

66. Osako, T., Ohtaka, A. & Uozumi, Y. Development of Polymer-Supported Transition-Metal Catalysts and Their Green Synthetic Applications. in *Catalyst Immobilization* 325–368 (Wiley, 2020). doi:10.1002/9783527817290.ch10.

67. Hyun, K. *et al.* Tailoring a Dynamic Metal–Polymer Interaction to Improve Catalyst Selectivity and Longevity in Hydrogenation. *Angewandte Chemie International Edition* **60**, 12482–12489 (2021).

68. Heuer, J. & Ferguson, C. T. J. Photocatalytic polymer nanomaterials for the production of high value compounds. *Nanoscale* vol. 14 1646–1652 Preprint at https://doi.org/10.1039/d1nr06985c (2022).

69. Liu, R. *et al.* Recyclable polymer-supported iridium-based photocatalysts for photoredox organic transformations. *J Catal* **407**, 206–212 (2022).

70. Li, X. *et al.* Organic sponge photocatalysis. *Green Chemistry* **19**, 2925–2930 (2017).

71. Li, W. *et al.* HIPE Polymerization Materials Functionalized with Iodic-BODIPY on the Surface as Porous Heterogeneous Visible-Light Photocatalysts. *Chem Asian J* **12**, 392–396 (2017).

72. Lessard, J. J. *et al.* Self-catalyzing photoredox polymerization for recyclable polymer catalysts. *Polym Chem* **12**, 2205–2209 (2021).

73. Boussiron, C., Le Bechec, M., Sabalot, J., Lacombe, S. & Save, M. Photoactive rose bengal-based latex via RAFT emulsion polymerization-induced self-assembly. *Polym Chem* **12**, 134–147 (2021).

74. Korpusik, A. B., Tan, Y., Garrison, J. B., Tan, W. & Sumerlin, B. S. Aptamer-Conjugated Micelles for Targeted Photodynamic Therapy Via Photoinitiated Polymerization-Induced Self-Assembly. *Macromolecules* **54**, 7354–7363 (2021).

75. Wu, W. & Liu, B. Modulating the optical properties and functions of organic molecules through polymerization. *Mater Horiz* **9**, 99–111 (2022).

76. Yoo, W.-J. & Kobayashi, S. Efficient visible light-mediated cross-dehydrogenative coupling reactions of tertiary amines catalyzed by a polymer-immobilized iridium-based photocatalyst. *Green Chem.* **16**, 2438–2442 (2014).

77. Kuckhoff, T. *et al.* Comonomer effects in vinyl based photocatalytic polymers. *RSC Applied Polymers* **2**, 155–162 (2024).

78. Freeburne, S., Sacco, J. L., Gomez, E. W. & Pester, C. W. Effects of Surface-Immobilization on Photobleaching of Xanthene Dye Photocatalysts. *Macromol Chem Phys* **224**, (2023).

79. Bell, K., Freeburne, S., Fromel, M., Oh, H. J. & Pester, C. W. Heterogeneous photoredox catalysis using fluorescein polymer brush functionalized glass beads. *Journal of Polymer Science* **59**, 2844–2853 (2021).

80. Ferguson, C. T. J. & Zhang, K. A. I. Classical Polymers as Highly Tunable and Designable Heterogeneous Photocatalysts. *ACS Catalysis* vol. 11 9547–9560 Preprint at https://doi.org/10.1021/acscatal.1c02056 (2021).

81. Hunter, B. *et al.* Photoactive polymer coatings for antibacterial applications. *Eur Polym J* **213**, (2024).

82. Bassan, E. *et al.* Visible-light driven photocatalytic CO2 reduction promoted by organic photosensitizers and a Mn(i) catalyst. *Sustain Energy Fuels* **7**, 3454–3463 (2023).

83. Cao, X. *et al.* Systematically tuning of optoelectronic properties from electron donating to accepting substituents on bicarbazole/cyanobenzene hybrids: Host to dopant materials for phosphorescent and delayed fluorescence OLEDs. *Org Electron* **52**, 22–31 (2018).

84. Phillips, D., Drake, R. C., O'Connor, D. V. & Christensen, R. L. Time Correlated Single-Photon Counting (Tcspc) Using Laser Excitation. *Instrum Sci Technol* **14**, 267–292 (1985).

85. Lawton, M., Bolden, R. C. & Shaw, M. J. A 10 ns multichannel photon counter. *J Phys E* **9**, 686–690 (1976).

86. Villa, M. *et al.* Organic super-reducing photocatalysts generate solvated electrons via two consecutive photon induced processes. *Chem Sci* **15**, 14739–14745 (2024).

87. Ishimatsu, R. *et al.* Solvent Effect on Thermally Activated Delayed Fluorescence by 1,2,3,5-Tetrakis(carbazol-9-yl)-4,6-dicyanobenzene. *J Phys Chem A* **117**, 5607–5612 (2013).

88. Nakagawa, T., Ku, S.-Y., Wong, K.-T. & Adachi, C. Electroluminescence based on thermally activated delayed fluorescence generated by a spirobifluorene donor–acceptor structure. *Chemical Communications* **48**, 9580 (2012).

89. Youn Lee, S., Yasuda, T., Nomura, H. & Adachi, C. High-efficiency organic light-emitting diodes utilizing thermally activated delayed fluorescence from triazine-based donor–acceptor hybrid molecules. *Appl Phys Lett* **101**, 093306 (2012).

90. Yin, X. *et al.* Recent Advances in Thermally Activated Delayed Fluorescent Polymer—Molecular Designing Strategies. *Front Chem* **8**, (2020).

91. Hua, T. *et al.* Heavy-atom effect promotes multi-resonance thermally activated delayed fluorescence. *Chemical Engineering Journal* **426**, (2021).

92. Lyra, E. P., Petzhold, C. L. & Lona, L. M. F. Tin(II) 2-ethylhexanoate and ascorbic acid as reducing agents in solution ARGET ATRP: A kinetic study approach by mathematical modeling and simulation. *Chemical Engineering Journal* **364**, 186–200 (2019).

93. Vega-Peñaloza, A., Mateos, J., Companyó, X., Escudero-Casao, M. & Dell'Amico, L. A Rational Approach to Organo-Photocatalysis: Novel Designs and Structure-Property Relationships. *Angewandte Chemie International Edition* **60**, 1082–1097 (2021).

94. Mateos, J. *et al.* Naphthochromenones: Organic Bimodal Photocatalysts Engaging in Both Oxidative and Reductive Quenching Processes. *Angewandte Chemie* **132**, 1318–1328 (2020).

95. Suresh Yedase, G., Venugopal, S., P., A. & Reddy Yatham, V. Catalyst-free Hantzsch Ester-mediated Organic Transformations Driven by Visible light. *Asian J Org Chem* **11**, e202200478 (2022).